# IMPACT OF INCREASED TEMPERATURE AND ATMOSPHERIC CARBON DIOXIDE ON MERCURY AND SULFUR SPECIATION IN PEATLAND SOILS

Master's Thesis

SUBMITTED TO THE FACULTY OF THE

GRADUATE PROGRAM IN LAND AND ATMOSPHERIC SCIENCE,

UNIVERSITY OF MINNESOTA

Anna Lucia Pax Krupp

IN PARTIAL FULFILLMENT OF THE REQUIREMENTS

FOR THE DEGREE OF

MASTER OF SCIENCE

Advisors: Dr. Brandy Toner and Dr. Ed Nater

August 2018

# ACKNOWLEDGEMENTS

I would like to thank my advisors, Dr. Brandy Toner and Dr. Ed Nater, for all of their instruction, advice, and help these past two and a half years. I would also like to thank Dr. Nic Jelinski for being part of my defense committee as well as for the much-appreciated direction and advice regarding my multiple linear regressions and statistics. I want to thank Dr. Laura Pigozzi for being part of my defense committee and for her work with me on my minor in Scientific and Technical Communication. Finally, I want to thank my family and friends for supporting me through this process. This thesis is dedicated to my fiancée, Brian Anderson, for always believing in me.

# ABSTRACT

Environmental mercury (Hg) pollution exists as a global public health issue without any localized borders. Volatile Hg emissions travel freely throughout the atmosphere, allowing anthropogenic point-source industrial emissions to have truly global impact. Recent research demonstrates that climate change may further impact the extent of environmental mercury pollution through increased production of monomethylmercury, more commonly known as methylmercury (MeHg), by various microorganisms within the soil, including sulfate-reducing bacteria, iron-reducing bacteria and methanogens. Continued research on the subject is warranted to fully understand the impacts of climate change on the environmental biogeochemical cycling of Hg and MeHg on various natural systems. Increasing global temperatures and levels of atmospheric $CO_2$ could significantly increase the net conversion of Hg to MeHg by sulfate-reducing and iron-reducing bacteria in systems particularly vulnerable to climate change such as ombrotrophic peatbogs, leading to an increased size in the net MeHg pool overall.

The Supplementary Files attached to this thesis document include the following files: raw data (SPRUCE_2012_2014_2015_2016_Peat_Final_Data.xlsx), untransformed multiple linear regression values (Regression_Non_Transformed.xlsx), log transformed multiple linear regression values (Regression_Log_Transformed.xlsx), maximum value calculations (Max_Calculations.xlsx), and fitted XANES data for 2012 (SPRUCE-2012-fit7-tidy.xlsx), 2015 (SPRUCE-2015-fit4-tidy.xlsx), and 2016 (SPRUCE-2016-fit4-tidy.xlsx).

TABLE OF CONTENTS

ACKNOWLEDGEMENTS...……...i

ABSTRACT……ii

TABLE OF CONTENTS……...……iii

LIST OF TABLES……..iv

LIST OF FIGURES……...……..v

CHAPTER 1……..……..1

CHAPTER 2……..……15

CHAPTER 3……..……21

CHAPTER 4……..……77

CHAPTER 5……..……82

BIBLIOGRAPHY……..83

APPENDIX……91

LIST OF TABLES

**Table 1** Summary of SPRUCE Project Temperature & $CO_2$ Treatment by Year……..……21

**Table 2** Mean Total Mercury (THg) Values for Years 2012-2016……..……..34

**Table 3** Minimum and Maximum Total Mercury (THg) Values for 2015……35

**Table 4** Minimum and Maximum Total Mercury (THg) Values for 2016……36

**Table 5** Mean Methylmercury (MeHg) Values for Years 2012-2016……....36

**Table 6** Minimum and Maximum Methylmercury (MeHg) Values for 2015……37

**Table 7** Minimum and Maximum Methylmercury (MeHg) Values for 2016……38

**Table 8** $Log_{10}$ Transformed Total Mercury (THg) Estimated Values, Standard Error, t Values and p Values……..53

**Table 9** $Log_{10}$ Transformed Total Mercury (THg) $R^2$, Akaike Information Criterion (AIC), and Bayesian Information Criterion (BIC) Values……53

**Table 10** $Log_{10}$ Transformed Total Mercury (THg) Variance Inflation Factor (VIF) Values…….....53

**Table 11** $Log_{10}$ Transformed Methylmercury (MeHg) Estimated Values, Standard Error, t Values, and p Values……..64

**Table 12** $Log_{10}$ Transformed Methylmercury (MeHg) $R^2$, Akaike Information Criterion (AIC), and Bayesian Information Criterion (BIC) Values…….65

**Table 13** $Log_{10}$ Transformed Methylmercury (MeHg) Variance Inflation Factor (VIF) Values…….65

LIST OF FIGURES

**Figure 1** Aerial Photograph SPRUCE Experimental Chambers[54]…….13

**Figure 2** Satellite Image of SPRUCE Experimental Chambers[54]……..13

**Figure 3** Total Mercury (THg) Concentration Depth Profiles for Years 2012-2016…….24

**Figure 4** Modeled Total Mercury (THg) Concentration Depth Profiles for Years 2012-2016…….26

**Figure 5** Methylmercury (MeHg) Concentration Depth Profiles for Years 2012-2016……29

**Figure 6** Modeled Methylmercury (MeHg) Concentration Depth Profiles for Years 2012-2016…….31

**Figure 7** Sulfur Reduced ($S_{red}$) Concentration Depth Profiles for Years 2012-2016…….40

**Figure 8** Percent Carbon (C) Depth Profiles for Years 2012-2016……42

**Figure 9** Percent Nitrogen (N) Depth Profiles for Years 2012-2016…….44

**Figure 10** Percent Sulfur (S) Depth Profiles for Years 2012-2016……46

**Figure 11** Maximum Total Mercury ($THg_{max}$) Depth vs. Temperature Treatment……49

**Figure 12** Maximum Methylmercury ($MeHg_{max}$) Depth vs. Temperature Treatment……...49

**Figure 13** Correlation Matrix for Multiple Linear Regression……..51

**Figure 14** Untransformed Total Mercury (THg) Histogram Plot……..55

**Figure 15** $Log_{10}$ Transformed Total Mercury (THg) Histogram Plot……56

**Figure 16** $Log_{10}$ Transformed Total Mercury (THg) Residuals vs. Fitted Values Plot…….57

**Figure 17** $Log_{10}$ Transformed Total Mercury (THg) Q-Q Plot……..58

**Figure 18** $Log_{10}$ Transformed Total Mercury (THg) Scale-Location Plot…….59

**Figure 19** $Log_{10}$ Transformed Total Mercury (THg) Residuals vs. Leverage Plot……60

**Figure 20** $Log_{10}$ Transformed Total Mercury (THg) Added Variable Plot for Depth Below Surface……61

**Figure 21** $Log_{10}$ Transformed Total Mercury (THg) Added Variable Plot for Percent Sulfur (% S)…….62

**Figure 22** Untransformed Methylmercury (MeHg) Histogram Plot……..67

**Figure 23** $Log_{10}$ Transformed Methylmercury (MeHg) Histogram Plot……68

**Figure 24** $Log_{10}$ Transformed Methylmercury (MeHg) Residuals vs. Fitted Values Plot…….69

**Figure 25** $Log_{10}$ Transformed Methylmercury (MeHg) Q-Q Plot…….70

**Figure 26** $Log_{10}$ Transformed Methylmercury (MeHg) Scale-Location Plot……71

**Figure 27** $Log_{10}$ Transformed Methylmercury (MeHg) Residuals vs. Leverage Plot……...72

**Figure 28** $Log_{10}$ Transformed Methylmercury (MeHg) Added Variable Plot for $log_{10}$ Transformed Total Mercury (THg)……73

**Figure 29** $Log_{10}$ Transformed Methylmercury (MeHg) Added Variable Plot for $log_{10}$ Transformed Reduced Sulfur ($S_{red}$)……74

**Figure 30** $Log_{10}$ Transformed Methylmercury (MeHg) Added Variable Plot for Depth Below Peat Surface……75

**Figure 31** $Log_{10}$ Transformed Methylmercury (MeHg) Added Variable Plot for Percent Nitrogen (% N)……...76

**Figure 32** Multiple Linear Regression for Total Mercury (THg) in 2016……..91

**Figure 33** Multiple Linear Regression for Methylmercury (MeHg) in 2016……91

**Figure 34** $Log_{10}$ Transformed Total Mercury (THg) Residuals vs. Leverage Plot……92

# CHAPTER 1

# Introduction

## 1.1 Environmental Mercury (Hg) Pollution

Mercury (Hg) is a toxic heavy metal found naturally occurring in the environment. Methylmercury (MeHg) is a highly toxic and bioavailable form of Hg, classified by the United States Environmental Protection Agency (EPA) as a powerful neurotoxin capable of bypassing the blood-brain barrier of fish and bioaccumulating up the food web[4] into humans, where it is known to cause neurological and reproductive damage to fetuses in vitro[5]. Over the last several decades, substantial efforts have been made in the United States and abroad to reduce human and specifically fetal exposure to MeHg, including various campaigns on the part of the Federal Drug Administration (FDA) and the EPA to eliminate fish high in Hg from the diet of pregnant women[6]. Despite substantial increases in public awareness over the last several decades, the issue of Hg consumption remains a serious public health problem in the United States. In 2011, the Minnesota Department of Health found that 8 percent of newborns within the Lake Superior Basin had MeHg levels above the U.S. EPA dose limit[7]. Thus, to this day, environmental Hg pollution presents a significant public health issue that needs to be addressed.

Environmental Hg pollution has clear anthroprogenic origins. Evidence from the Peruvian Andes, Spain and Southern France indicate that mining for Hg deposits in ore-rich areas began as far back as several thousand years ago, thus long before the industrial revolution, it is likely that early mining for Hg and other ores in close proximity caused

increased amounts of Hg to enter the environment[8]. Heavy metals have historically been used by humans all over the world for a variety of purposes, with large amounts of heavy metal waste entering the environment as a direct consequence of industrial use. In fact, since the domestication of fire itself, human activity and environmental heavy metal pollution have been inextricably connected, with historical evidence suggesting that our cave dwelling ancestors released small amounts of trace metals burning firewood[9].

Evidence of early atmospheric metal pollution in Europe suggests that human mining and metallurgy activities began as far back as the Chalcolithic/Early Bronze Age[10], thus, by prehistoric times, increased amounts of heavy metals had already begun to enter the environment as a result of human activity. During the Roman Empire, small scale mining efforts for lead (Pb), copper (Cu), zinc (Zn) and Hg "resulted in substantial emissions of trace metals to the atmosphere,"[9] producing a significant impact on global air quality. With the onset of the industrial revolution during the 19$^{th}$ century, heavy metal usage increased substantially. Analysis of central Greenland snow and ice cores indicates that concentrations of Pb, Zn, cadmium (Cd) and Cu continued to increase because of large-scale atmospheric pollution of the northern hemisphere up until the late 1970's before substantially decreasing over the next several decades[11].

Industrial pollution is considered a major anthropogenic source of environmental heavy metal contamination[1], with Pb, Cd, and Hg being cited as the heavy metals posing the greatest threats to human health as well as the health of other species and the planet[2]. Industries such as agricultural, pharmaceutical and textile production processes all act as significant sources of heavy metals to the environment[1]. Smelting and metal production have also been associated with the accumulation of various contaminants in the soil,

including Pb, Zn, nickel (Ni), Cu, iron (Fe) and arsenic (As), while manganese (Mn) and Cd contamination has often been observed in soils impacted by textile manufacturing processes[3].

Fossil fuel combustion is also a primary anthropogenic source of Hg pollution to the environment[12], responsible for approximately 60 percent of all global Hg emissions in the year 2000[13]. Coal burning alone is responsible for approximately 470 tons of Hg emitted annually, accounting for nearly a quarter of the nearly 2000 tons of Hg emitted to the atmosphere each year[14]. Artisanal and small-scale gold production have also been cited as being significant sources of Hg pollution to the environment, resulting in the annual emission of over 700 tons of Hg to the atmosphere to later end up in local water and soil systems[14].

Mercuric sulfide (HgS), or cinnabar, is a sparingly soluble, non-toxic form of Hg commonly found naturally occurring in the environment[15]. Between 1950 and 2003, active mining for HgS and minor pyrite ($FeS_2$) occurred in conjunction with metallurgical production in Almadén, Spain[16]. Prior to the sites closure, gaseous elemental mercury (GEM) levels as high as 20,000 ng $m^{-3}$ were found in the air around the main facility and Hg concentrations in the soil were found to exceed 800 ng $m^{-3}$ [16]. Such high levels of Hg contamination clearly demonstrate the measurable negative environmental impact of human industrial activity on the release of mercury into the environment.

### 1.2 Background on Peatlands

Peatlands are a type of wetland comprised mainly of organic soils. Peatlands form

under conditions of near-permanent saturation, which produce anaerobic conditions conducive to the preservation of organic materials deposited to the saturated soil surface. Peatland ecosystems are commonly found in boreal regions where low temperatures and shorter growing seasons enhance the preservation of organic materials. Peatlands have been shown to be primary sources for the methylation of Hg[17]. Additionally, peatlands are sensitive ecosystems that will likely be strongly impacted by climate change.

Ombrotrophic peatlands are unique in their hydrology due to having raised centers, making them hydrologically isolated from the surrounding uplands. Consequently, ombrotrophic peatlands receive all their nutrients from atmospheric deposition and can be characterized as being nutrient poor and low pH. Ombrotrophic peatlands therefore provide unique opportunities for the study of biogeochemical processes, including the cycling of Hg. Previous research has demonstrated that increasing sulfate deposition in peatlands can be correlated with a decrease in Hg storage and an increase in mercury methylation[18], while chronic sulfate deposition has been shown to increase the ability of peatlands to methylate Hg and store MeHg [18]. Furthermore, mercury methylation within a boreal peatland has been shown to decline with the cessation of experimental increases in sulfate deposition[19].

### 1.3 Biogeochemistry of Mercury (Hg) and Sulfur (S)

Initially occurring on the local scale, the impacts of Hg contamination have global consequences. Gaseous elemental mercury (GEM) is easily transported[15] and can be transported long distances in the atmosphere[20] before being deposited in terrestrial

ecosystems by precipitation and/or dry deposition, making atmospheric deposition a primary source of Hg contamination, even to pristine environments[21]. It is important to note that the long half-life of GEM in the atmosphere results from its relatively low solubility in water. Consequently, only a small fraction of GEM is deposited from the atmosphere as precipitation at any given time. Additionally, Hg that enters a natural system via atmospheric deposition has been shown to be more bioavailable and vulnerable to methylation than Hg found preexisting in the soil[22]. Gaseous $Hg^{2+}$ is more soluble than GEM and dominates during precipitation[21]. Upon entering an aqueous environment, inorganic $Hg^{2+}$ becomes bioavailable when solubilized [15] and can be further transformed by sulfate-reducing bacteria (SRB) to MeHg[23], a potent neurotoxin presenting significant danger to the health of aquatic ecosystems via biomagnification upwards through the food web[23].

$$Hg^{0}_{(g)} \rightarrow Hg^{2+}_{(g)} \rightarrow Hg^{2+}_{(aq)} \rightarrow MeHg_{(aq)} \qquad \textbf{(Equation 1)}$$

### 1.4 Role of Microbes in Mercury (Hg) Methylation

The methylation of Hg to MeHg is a processed that is mediated by microbes in the natural environment[24, 25]. Three major groups of bacteria are primarily responsible for the methylation of Hg: sulfate-reducing bacteria (SRB), iron-reducing bacteria (IRB), and methanogens[26]. Both SRB and IRB have previously been implicated in the production of MeHg in freshwater river sediments[24,25] and increasing levels of MeHg have been observed with the addition of inorganic Hg to freshwater sediments containing SRB[24].

SRB are, thus, considered principle Hg methylators, responsible for the transformation of soluble $Hg^{2+}$ to MeHg in the environment[27]. Under anoxic conditions, SRB can reduce $SO_4^{2-}$ to hydrogen sulfide ($H_2S$), resulting in binding between sulfide ion and any free metal present and the subsequent precipitation of metal sulfides, for example, iron sulfide (FeS). Furthermore, the formation of HgS has been observed occurring "only where sulfide [S(-II)] is produced from porewater sulfate by microbial activity," a process which itself can only occur under suboxic to anoxic conditions [28,29].

$$SO_4^{2-}{}_{(aq)} \rightarrow H_2S_{(g)} \qquad \textbf{(Equation 2)}$$

Increasing average temperatures associated with climate change may have significant impacts on the activity of the soil microbial community. Simulated warming has previously been shown to shift the species distribution within soil microbial communities[31], thus, increasing temperatures may also affect the distribution of SRB, IRB, and methanogens within peatland soil, potentially leading to subsequent changes in the cycling of Hg and sulfur (S).

### 1.5 Environmental Cycling of Mercury (Hg) and Sulfur (S)

The biogeochemical cycling of S presents a significant control on the methylation of Hg in the environment. Thus, a comprehensive understanding of the cycling of Hg and S between the atmosphere and the soil is crucial in order to mitigate potential environmental contamination resulting from future changes in global climate. Research has shown that Hg is strongly adsorbed to natural organic matter (NOM) because of its high affinity for S-containing functional groups[32]. X-ray absorption spectroscopy (XAS)

evidence obtained on humic soils demonstrated that reduced S functional groups are preferred over oxygen ligands for Hg (II) complexation[33], while extended X-ray absorption fine structure (EXAFS) spectroscopy further indicated the relationship between Hg(II)–S bond distance and Hg(II) coordination[34] and established linear two-coordination complexation between Hg(II) and reduced S in the soil[35] . Researchers previously characterized soils in close proximity to an industrial complex contaminated with elemental mercury and found that the Hg present was in the form of Hg-sulfide[36]. Sulfur is also influential on the production of MeHg[18]. Sulfide inhibition of microbial mercury methylation may decrease with the addition of dissolved organic matter[37].

### 1.6 Impact of Climate Change on the Biogeochemical Cycling of Mercury (Hg) and Sulfur (S)

For the past three decades, average temperatures at the Earth's surface have been the warmest on record since 1850[38]. According to current EPA models, the Earth's surface is expected to warm by up to +5°C by the end of this century, in conjunction with increased atmospheric $CO_2$ concentrations[39]. Future changes in precipitation are debatable, however, small increases in total annual precipitation are expected, coupled with more intense storms and potentially longer dry periods between the storms[39]. Overall, we expect to see a dryer climate in summer, at least, likely due to increased evapotranspiration and longer growing seasons[39].

Temperature is an important control on the bioaccumulation of mercury upwards through the food web. Increases in average global temperature will have significant

impact on the methylation of Hg within the soil. The extent of Hg methylation and bioaccumulation is dependent on environmental conditions rather than the amount of atmospheric deposition[23]. Evidence suggests that the warming climate could increase the scavenging rate of "available" Hg from the water column by algal-derived organic matter and result in increased contaminant bioavailability to fish[40]. Research clearly demonstrates that the extent of bioaccumulation in fish is significantly impacted by changes in temperature and increases in MeHg concentrations in fish have been observed in correlation with both experimental and natural warming[41].

Research on MeHg production in Artic soil concluded that climate induced warming of the Artic soil from -2 to 8°C could potentially enhance net MeHg production by up to an order of magnitude[22]. Changes in climate have been shown to drive the release of carbon (C) and Hg from peatlands previously overlain by permafrost and increased accumulation of sediment Hg has been observed to occur during warmer periods of increased atmospheric Hg input[44]. Results of data collected from high Artic coastal marine sediments demonstrated that increases in temperature caused increased rates of methylmercury production[45]. Furhermore, sulfate reduction was found to be temperature dependent and most importantly, with increases in temperature, compensatory demethylation was not observed[45].

Increased levels of atmospheric $CO_2$ may also impact the cycling of Hg between the atmosphere and the soil. Elevated atmospheric $CO_2$ has been shown to cause increases in Artic soil C storage[46] and atmospheric $CO_2$-induced changes in percent soil organic matter could potentially cause an increase in the capacity of soil to store mercury[47]. Alternatively, rising atmospheric $CO_2$ levels can be correlated with increased

soil acidification[48]. However, precipitation and fertilization levels have been shown to be more important controls than acidity on the methylation of Hg[49], with increased acidity impacting the soil leaching of other metals such as Cd to a much larger extent than Hg[50].

Over half of the total anthropogenic $CO_2$ emissions have occurred in the last 40 years, with $CO_2$ emissions accounting for 78% of the total greenhouse gas emissions between 1970 and 2010[38]. Increases in atmospheric $CO_2$ will likely impact the biogeochemical cycling of Hg between the atmosphere and the soil. Researchers have established that elevated levels of atmospheric $CO_2$ have the potential to impact both bacterial activity and diversity[42]. One study found that elevated $CO_2$ resulted in increased microbial activity for both cellulose-degrading and lignin-degrading enzymes in the soil[43].

Increases in average temperatures and atmospheric $CO_2$ concentrations will likely affect the biogeochemical cycling of Hg and S in the natural environment. Recent research demonstrates that increases in average global temperatures and atmospheric $CO_2$ have the potential to release increased quantities of THg and MeHg into natural ecosystems[22,45,47]. Further research will be needed to fully quantify the impact of climate change on these systems and potentially mitigate environmental issues resulting from increased production of MeHg.

### 1.7 SPRUCE Site Description

The Spruce and Peatland Response Under Changing Environments (SPRUCE) project is a 10-year multi-disciplinary environmental study supported by the United

States Department of Agriculture Forestry Service (USDA-FS) and comprising a major portion of the Terrestrial Ecosystem Science Scientific Focus Area within the Oak Ridge National Laboratory (ORNL) Climate Change program and coordinated by Dr. Paul Hanson (ORNL) and Randy Kolka (USDA-FS). My research, therefore, spans only a portion of an ongoing 10-year study in the MEF, aimed at establishing the potential impact of increased temperature and atmospheric $CO_2$ concentrations on a wide variety of environmental processes.

The main objective of the SPRUCE project is to simulate two components of climate change, namely, increased temperatures and increased atmospheric $CO_2$ concentrations, and to determine the impact, if any, of those changes on various environmental processes naturally occurring within an ombrotrophic peatland. The biogeochemical cycling of Hg will likely be impacted by climate change[22,47]. Previous studies have found that increases in the average global temperature may lead to increased production of MeHg[22], while elevated levels of atmospheric $CO_2$ could result in an increased capacity to store Hg in the soil[47].

The SPRUCE research site is located in an ombrotrophic peat bog, therefore, all nutrient input to the experimental enclosures is limited to atmospheric deposition. Atmospheric deposition of Hg and S are both closely related to industrial emissions of Hg and S during the industrial revolution. In addition, the methylation of Hg to MeHg occurs in the anoxic zone around the water table, the same zone in which the reduction of sulfate to sulfide is known to occur, and both processes are known to be mediated by sulfate-reducing bacteria. Furthermore, according to human chorionic gonadotropin (hCG) gene

sequencing, all three types of methylating microbes mentioned here (SRB, IRB, and methanogens) are present at the SPRUCE site[30].

The SPRUCE experimental plots consist of 10 large open-top enclosures which are each 12 meters in diameter and 8 meters in height. Aerial photographs of the SPRUCE site are shown in **Figure 1** and **Figure 2**. Experimental enclosures are assigned temperature treatments (0, 2.25, 4.5, 6.75, and 9° above ambient temperature) in pairs, with one of each pair receiving ambient $CO_2$ treatment (400 ppm), and the other of each pair receiving elevated $CO_2$ treatment (900 ppm). Experimental enclosures are located on the S1 bog within the Marcell Experimental Forest (MEF), 40 km north of Grand Rapids, Minnesota, U.S.A. (47˚30.476' N; 93 ˚ 27.1620'W and 412 m a.m.s.l)[51]. The MEF was established in 1962 by the United States Department of Agriculture (USDA) Forest Service for conducting long-term environmental research[52]. The MEF is comprised of ombrotrophic peatlands, fens and lakes which formed in Wisconsinan glacial moraine deposits[52], with exposed sandy outwash comprising one third of the MEF soils[52] and sandy outwash covered by clay loam, limestone and shale fragments, and loess occupying the remaining two thirds[52].

Research watersheds at the MEF are designated as S1, S2, S3, S4, S5, and S6. The S1 watershed drains first to Cutaway Lake and then to the Prairie River and the Mississippi River before finally reaching the Gulf of Mexico. Within the S1 bog, in general, the depth of the peat ranges from 2 to 4 m deep with a maximum depth of 10 meters below the surface in one particular location and the water-table fluctuates within 30 cm of the surface[52]. The surface of the S1 bog is made up of alternating raised hummocks and wet hollows[52]. The average relief between the maximum of the hummock

and the minimum of the hollow ranges from 20 to 30 cm[51]. When the water table nears the surface of the peat, water flows laterally to the lagg, or margin of the peatland, and to an outlet stream[52].

Mean annual air temperature at the MEF is 3.4°C[52] and average air temperatures have increased by 0.4°C per decade since 1961[52], with an average annual precipitation at the MEF of 780 mm within the same time period[52], and with a third of the total precipitation being due to snowfall[52]. Since 1979, the rate of wet ammonium deposition at the MEF has remained steady, while nitrate deposition has decreased during the same time period[52]. Decreases in wet deposition of hydrogen, chloride, and base cations (Ca, Mg, K, Na) have been observed since 1979[52]. Observed wet deposition of mercury at the MEF decreased in the 1980s before increasing during the 1990s and continuing to increase since[52].

Each experimental chamber partially encloses a group of black spruce trees (*Picea mariana)* atop peatland moss (*Sphagnum spp.)*. Initial soil core sampling began in 2012 and final construction of experimental enclosures was completed in 2015. Deep-soil (below-ground) and air (above-ground) heating elements were installed in 2014 and 2015, respectively. Peat sampling in 2014 was conducted prior to the initiation of soil heating. Chambers designated as "ambient temperature" and "ambient $CO_2$" were used for controls. $CO_2$ concentrations in one of each temperature pair were increased to 900 ppm in the middle of 2015, therefore all sampling prior to and including 2014 can be considered "time zero" data. Data collected in 2016 represent the first year within the SPRUCE study for which all intended experimental components were in place. More

details on the process of simulating climate change in the context of the SPRUCE project can be found in the 2017 publication by Hanson et al.[53].

**Figure 1** Aerial Photograph SPRUCE Experimental Chambers[54]

**Figure 2** Satellite Image of SPRUCE Experimental Chambers[54]

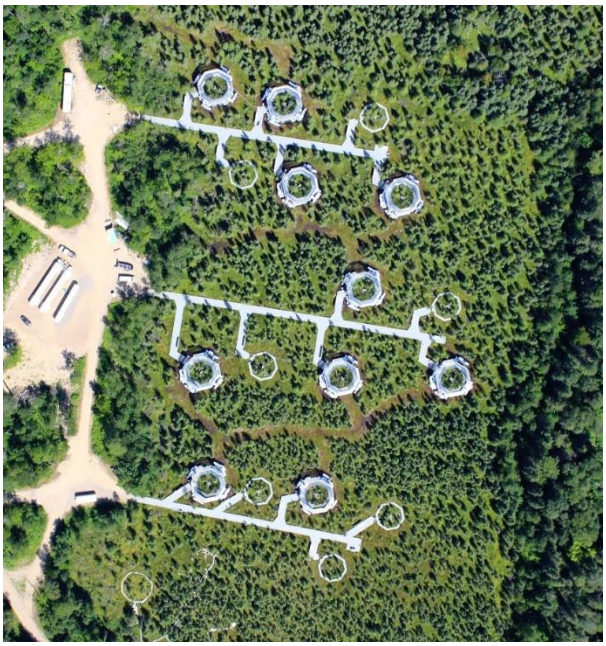

## 1.8 Study Objectives

The objectives of the present study were to determine the impact of increasing temperatures and atmospheric $CO_2$ on the biogeochemical cycling of Hg and S in an ombrotrophic peatland via analysis of Hg and S speciation in peat cores obtained annually from the SPRUCE site. There were two major objectives to this study. First, this study proposed to determine the relationship between THg, MeHg, and $S_{red}$ using a combination of CVAFS, S 1s XANES spectroscopic analysis, and elemental analysis of C, nitrogen (N), and S of peat cores through depth and over time. Second, this study also intended to determine whether simulated warming and $CO_2$ elevation will impact the depth below the surface at which the maximum values for THg ($THg_{max}$) and MeHg ($MeHg_{max}$) occur in peatland soils. This purpose of this was to evaluate whether heat and/or $CO_2$ treatment impacts the magnitude of $THg_{max}$ and $MeHg_{max}$ as well as the depth at which they occur. Statistical models were also generated to describe the behavior of THg and MeHg based on various physiologically related variables (depth, $S_{red}$, %C, %N, %S).

# CHAPTER 2

# Methodology

## 2.1 SPRUCE Field Campaign

Peat cores were collected from SPRUCE experimental plots in August 2012, June 2014, September 2014, June 2015, and August 2016. Peat core samples were collected from hummocks and hollows using a hole saw and a Russian peat borer. In 2012, peat cores were taken from both hummocks and hollows down to a maximum depth of 250 cm below the peat surface. In 2014, 2015, and 2016, peat cores were taken from hollows only down to a maximum depth of 200 cm below the peat surface. Peat cores were segmented into the following depth increments: 0-10, 10-20, 20-30, 30-40, 40-50, 50-75, 75-100, 100-125, 125-150, 150-175, 175-200, 200-225, and 225-250 cm (where applicable). Peat core samples were separated into two subsamples intended for either S 1s XANES analysis or Hg analysis. Subsamples intended for Hg analysis were placed in capped vials and frozen on dry ice immediately following sampling. Subsamples intended for S 1s XANES analysis were collected in ultraclean IChem boro-silicate vials capped with Teflon-lined septa and purged with argon immediately following sampling. Following the argon purge, samples intended for S 1s XANES analysis were heat-sealed in Mylar bags containing oxygen scrubbers and frozen on dry ice.

## 2.2 Total Mercury (THg) and Methylmercury (MeHg) Analysis in Peat

In this study, Hg speciation in a boreal peatland was determined through depth using cold vapor atomic fluorescence spectrometry (CVAFS) to measure the

concentrations of total Hg (THg), and MeHg, present in peat samples obtained from the SPRUCE site. Peat samples analyzed for THg were freeze-dried and then oven digested in concentrated nitric acid overnight at 70°C. THg concentration was then determined by double amalgamation and cold vapor atomic fluorescence spectroscopy (CVAFS) according to EPA Method 1631[55]. Peat samples collected in 2012 were analyzed for THg on a Brooks-Rand III CVAFS analyzer, whereas peat samples collected in 2014, 2015 and 2016 were analyzed for THg on a Tekran 2600 CVAFS analyzer. Blanks and standard reference materials were run approximately every 15 samples. Duplicates were run for 10% of samples and 10% of samples were spiked with known amounts of THg.

Peat samples analyzed for MeHg were freeze-dried and then oven digested in a solution of 25% potassium hydroxide and methanol for 4 hours at 90°C. Following digestion, samples were distilled at 135°C in 60 mL perfluoroalkoxy (PFA) Teflon impinger vessels. Distillates were ethylated with sodium tetraethylborate and analyzed for MeHg by capillary gas chromatography and CVAFS detection on a Tekran 2700 CVAFS analyzer according to EPA Method 1630[56]. Blanks and standard reference materials were run approximately every 15 samples. Duplicates were run for 10% of samples and 10% of samples were spiked with known amounts of MeHg.

### 2.3 Sulfur (S) 1s X-ray absorption near edge structure (XANES) Spectroscopy

In this study, S speciation in a boreal peatland was determined through depth using S 1s X-ray absorption near-edge structure (XANES) spectroscopy to determine the relative proportions of S containing groups in soil core samples. All XANES data were

run at the Canadian Light Source on the 06B1-1 Soft X-ray Microcharacterization Beamline (SXRMB) in Saskatoon, Canada. See appendix (AA-XX) for full spreadsheets containing raw XANES data. No photon damage to the sample was observed and 2 scans were taken for each sample and averaged to give the final spectrum. Reference S XANES spectra were acquired for gypsum in total electron yield (TEY) mode and the energy calibration of the monochromator was accomplished using the set absorption maximum for gypsum at 2482.74 eV. All S XANES spectra were acquired in fluorescence mode. The reference spectral database consisted of previously published spectra[51,57,58].

All S XANES spectra underwent pre-edge subtraction and post-edge normalization using a set edge jump value of 1. Normalized spectra were subsequently fitted with linear combinations of the compiled reference spectra over the range of 2450-2550 eV using linear combination fitting software "EXAFS Linear least-squares fit, combinations"[59]. The quality of each fit was determined by calculating the normalized sum-of-squares (NSS) parameter for each sample requiring at least a 10% decrease in the calculated value of NSS to justify the inclusion of an additional component. The sum of the component fractions for each were not limited to 1.

Linear combination fitting of experimental spectra with reference spectra was performed using a custom program called mrfitty[60]. The mrfitty program was created using SciPy[61,62] and can be found at https://github.com/jklynch/mr-fitty. The original fits can be viewed in the Supplementary Files. After linear combination fitting with reference standards, the reference components were binned into groups to reflect S valence state and local coordination environment. The proportion of $S_{red}$ was calculated by summing

contributions of all thiol, organic mono-sulfide, thiophene, and organic di-sulfide species. Reduced S species were combined to give $S_{red}$ for subsequent linear regression analysis.

### 2.4 Determination of Elemental Carbon (C), Nitrogen (N), and Sulfur (S)

Percent carbon (%C), percent nitrogen (%N), and percent sulfur (%S) were determined through depth via dry combustion analysis at 1150°C using an Elemental Pyrocube combustion analyzer in CNS mode.

### 2.5 Statistical Analysis

Statistical analyses were conducted in R version 3.4.1[63] using the following packages: ggplot2[64], colorspace[65], scales[66], tidyverse[67], GGally[68], cowplot[69], gridExtra[70], ggpubr[71], devtools[72], ggfortify[73,74], and Rmisc[75]. THg and MeHg depth profiles were fitted using non-linear modeling and the Ricker function obtained from Archontoulis et al.[76,77]. Data were log normalized following linear regression calculation of $R^2$ values as well as inspection of residuals for transformed and untransformed variables using qqplot. Multiple linear regression was accomplished using a stepwise process to select the model with the best fit. In this case, the intended purpose of conducting linear regression was to better understand the relationships between independent variables rather than for the purpose of prediction.

Linear regression modeling for THg, shown in **Figure 32 [AA-91]**, was accomplished beginning with single regressions of log THg against the following

independent variables: temperature (+0°C, +2.25°C, +4.5°C, +6.75°C, and +9°C), atmospheric $CO_2$ (either ambient or elevated), depth, bulk density, log %C, log %N, log %S, and log $S_{red}$. $R^2$ and p values were calculated to determine the model with the best fit. The independent variable with the highest $R^2$ value and significant p values was selected and retained in the model. This process was repeated with the remaining independent variables until all variables had been incorporated into the model or any remaining variables could be eliminated based on insignificant p values ($p < 0.05$).

Linear regression modeling for MeHg, shown in **Figure 33 [AA-91],** was accomplished similarly beginning with single regressions of log MeHg against the following independent variables: temperature (+0°C, +2.25°C, +4.5°C, +6.75°C, and +9°C), atmospheric $CO_2$ (either ambient or elevated), depth, bulk density, log %C, log %N, log %S, log $S_{red}$, and log THg. $R^2$ and p values were calculated to determine the model with the best fit. The independent variable with the highest $R^2$ value and significant p values was selected and retained in the model. This process was repeated with the remaining independent variables until all variables had been incorporated into the model or any remaining variables could be eliminated based on insignificant p values ($p < 0.05$).

Variance inflation factor (VIF) values were calculated to check for co-variance, with VIF values greater than 10 considered significant evidence of strong co-variance and requiring reconsideration of the inclusion of both variables in the model (**Table 13**). Akaike information criterion (AIC) and Bayesian information criterion (BIC) values were calculated and models with minimized AIC and BIC values were selected. Residuals were analyzed using qqplot and multiple different residual plots were generated,

including plots of residuals versus fitted values, the square root of the standardized residuals versus fitted values, and residuals versus leverage values. Residuals that are normally distributed should show good agreement with the horizontal axis. Added variable plots (also referred to as partial regression plots) were also generated for each independent variable in both linear regression models. Added variable plots with non-zero slopes support the conclusion that the addition of an independent variable has significant impact on the model overall and should be retained.

In the process of multiple regression analysis, one data point ("point 353") was identified as a potential outlier based on an abnormal residual plot for THg (**Figure 34**) (**AA-92**). The data point corresponded to a 2012 sample taken from a control plot with no temperature treatment or $CO_2$ elevation. The THg value for "point 353" was consistent with the range of THg seen in the remaining samples, however, upon inspection of the determined %C, %N, and %S values corresponding to that same sample, it was clear that the data point in question was not valid. For example, %C for all other samples was on the scale of 40%, however, %C for "point 353" was 8.6%. Furthermore, %N for all other samples was on the scale of 2.5%, however, %N for "point 353" was 0.5%. Finally, %S for all other samples was on the scale of 30%, however, %S for "point 353" was 89%. "Point 353" was removed from the data set and linear regression was revised. Residual plots from before and after the removal of "point 353" were compared and a significant improvement in residuals was noted (**Figure 19**). This improvement confirmed the decision to remove "point 353" from the dataset as an outlier.

# CHAPTER 3

## Results

Samples collected 2012 and 2014, prior to the initialization of heat treatment and $CO_2$ elevation, were considered as corresponding to ambient temperature and $CO_2$ -treatment. Below-ground "deep heat" temperature treatment was initiated prior to the 2015 peat sampling, therefore, samples collected in 2015 were exposed to some heat treatment, however, they were still collected prior to $CO_2$ elevation and above-ground heat treatment. Above-ground temperature treatment and elevation of $CO_2$ concentrations from 450 ppm ("ambient") to 900 ppm ("elevated") in selected enclosures (half of each temperature pair) was initiated prior to 2016 sampling, therefore, samples collected in 2016 were exposed to the full range of treatments, including above- and below-ground heat treatments and $CO_2$ elevation. Data collected in 2016, thus, represent a full data set with controls. Temperature and $CO_2$ treatment are summarized by year in **Table 1**.

**Table 1** Summary of SPRUCE Project Temperature & $CO_2$ Treatment by Year

| Year | Temperature Treatment | $CO_2$ Treatment |
|---|---|---|
| 2012 | Ambient | Ambient |
| 2014 | Ambient | Ambient |
| 2015 | Below ground only | Ambient |
| 2016 | Above & below ground | Elevated |

### 3.1 Total Mercury (THg) and Methylmercury (MeHg) Concentration Depth Profiles

Results of THg analysis were displayed as THg concentration (ng/g) versus depth (cm) and displayed in **Figure 3**. Far below the peat surface, at depths near 200 cm, THg concentrations are consistently at a low, around 30 ng/g, corresponding to pre-industrial levels. A maximum in THg concentration is observed 15 to 60 cm below the peat surface, corresponding to increased THg deposition during the 1850's with the industrial revolution[78], with maximum THg ($THg_{max}$) values averaging between 132 and 188 ng/g. Following this spike, THg levels decline back to near pre-industrial levels towards the surface, corresponding to declines in THg deposition since the 1970's with the introduction of emissions regulations[79]. Total mercury concentrations were also modeled for better data visualization using the Ricker's function obtained from Archontoulis et al.[77,76] and plotted versus depth over the intended range of temperature treatments (+0°C, +2.25°C, +4.5°C, +6.75°C, and +9°C) (**Figure 4**).

Results of MeHg analysis were displayed as MeHg concentration (ng/g) versus depth (cm) in **Figure 5**. Far below the peat surface, at depths near 200 cm, MeHg concentrations are consistently at a low, approaching 0 ng/g, corresponding to pre-industrial levels of THg and low net rates of methylation at low depths. A maximum in MeHg concentration is observed at 5 to 45 cm below the peat surface, corresponding to increased production of MeHg with increased THg deposition during the 1850's with the industrial revolution[78]. The maximum MeHg ($MeHg_{max}$) values averaging between 4.31 and 5.46 ng/g also reflect environmental conditions favoring net methylation. Following this spike, MeHg levels decline to near pre-industrial levels towards the surface, corresponding to declines in THg deposition since the 1970's with the introduction of

emissions regulations[79] and lower net methylation in the more oxic near-surface peat. Methylmercury concentrations were also modeled for better data visualization using the Ricker's function obtained from Archontoulis et al.[77, 76] and plotted versus depth over the intended range of temperature treatments (+0°C, +2.25°C, +4.5°C, +6.75°C, and +9°C) (**Figure 6**).

**Figure 3** Total Mercury (THg) Concentration Depth Profiles for Years 2012-2016

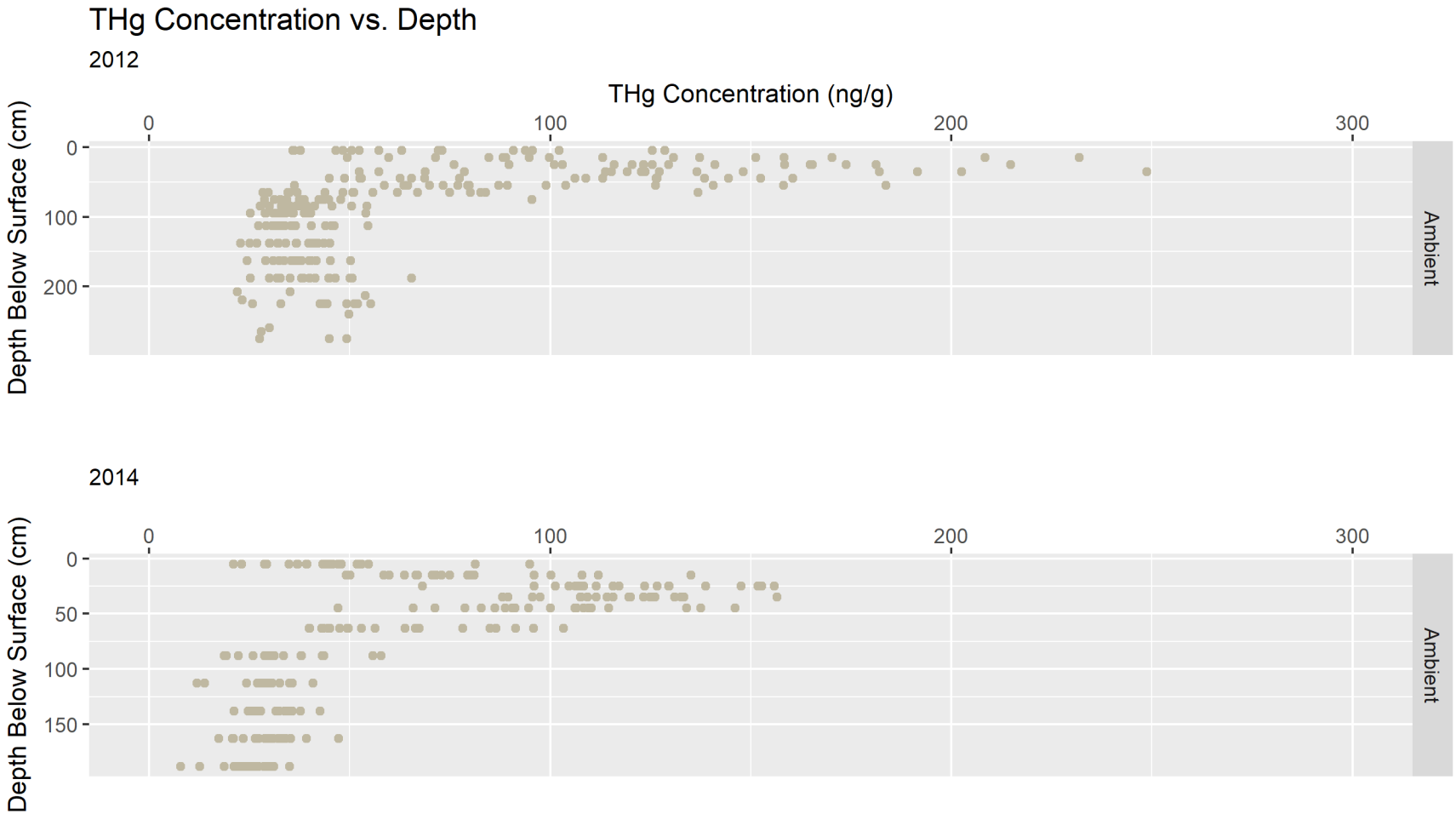

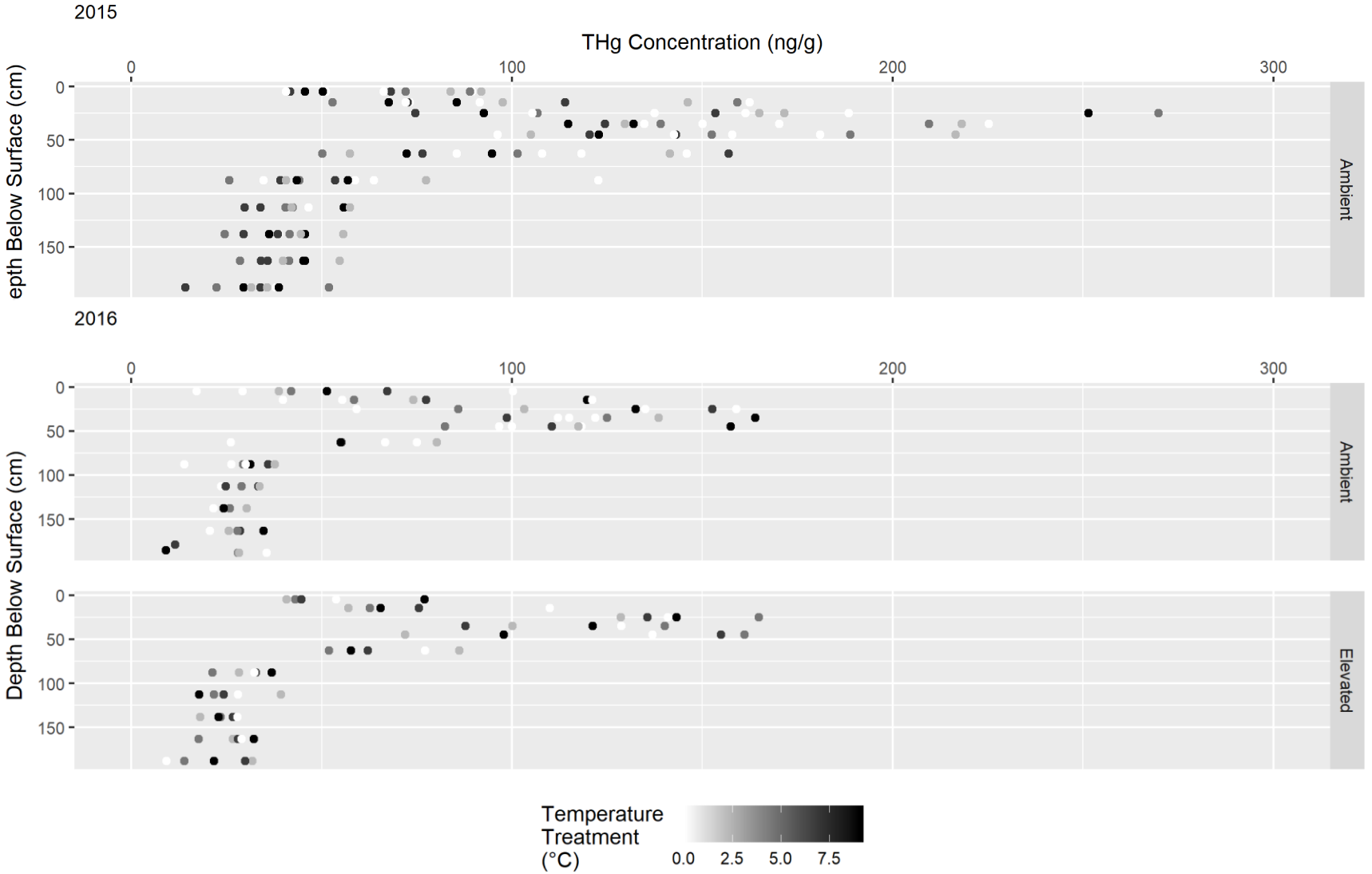
2015
THg Concentration (ng/g)
0
100
200
300
epth Below Surface (cm)
0
50
100
150
Ambient
2016
Depth Below Surface (cm)
Ambient
Elevated
Temperature Treatment (°C)
0.0
2.5
5.0
7.5

**Figure 4** Modeled Total Mercury (THg) Concentration Depth Profiles for Years 2012-2016

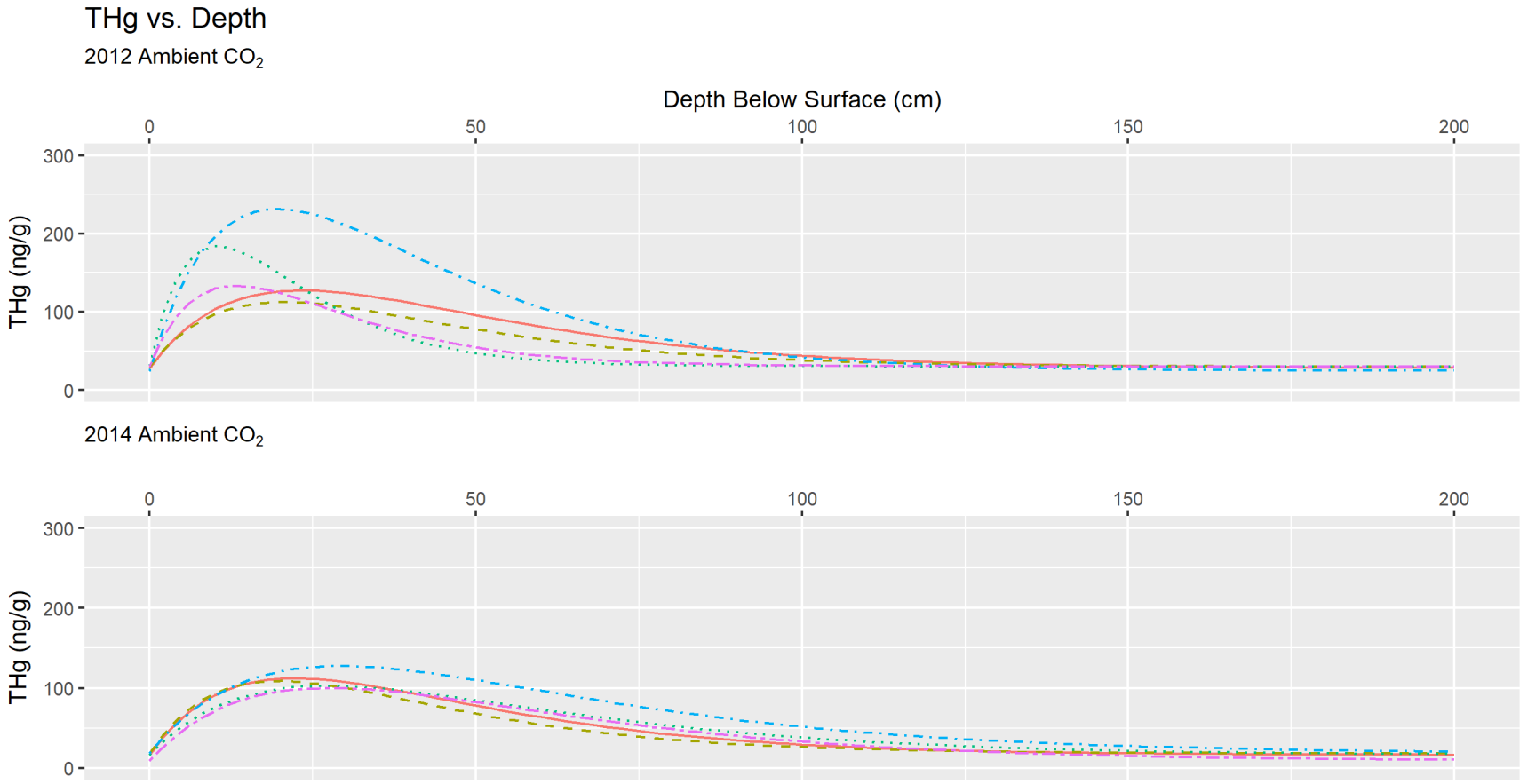

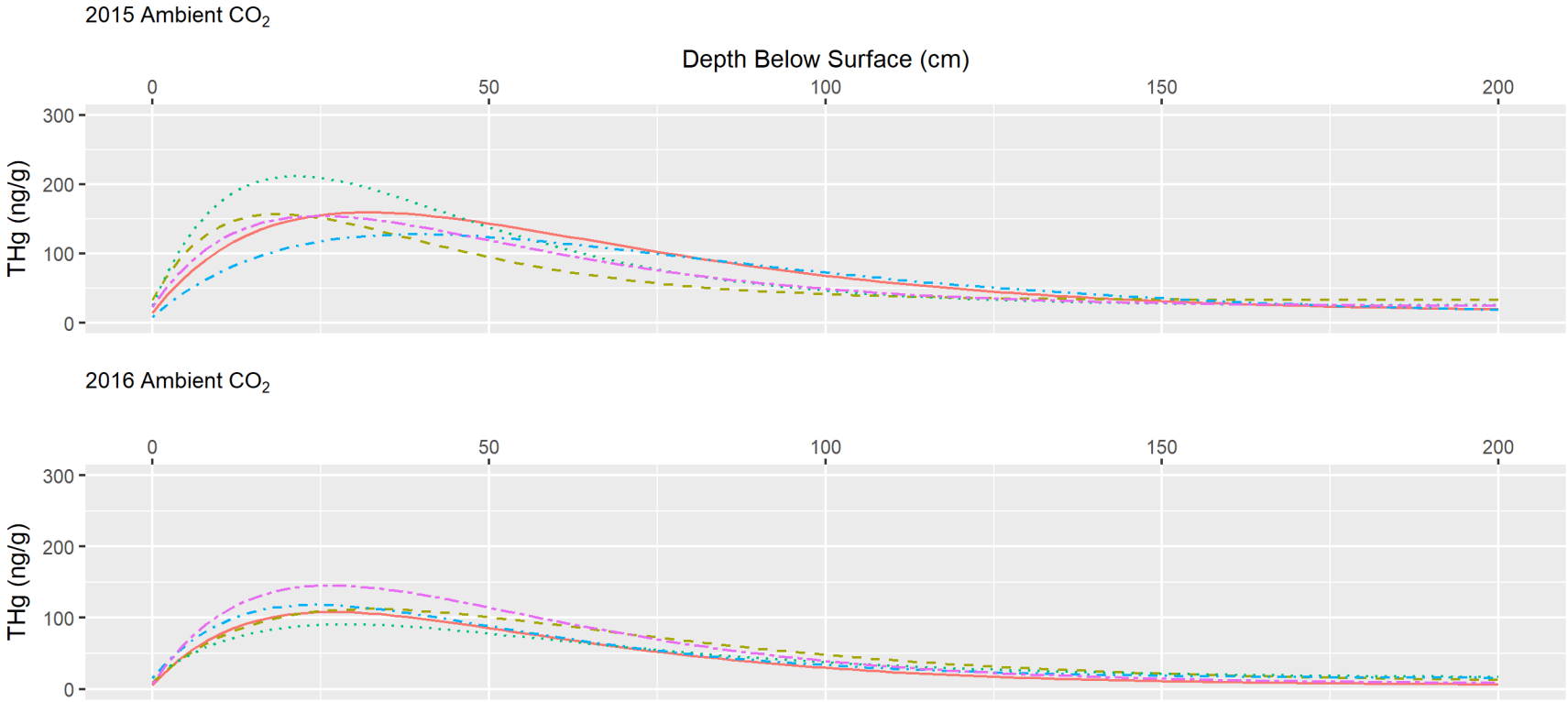
2015 Ambient $CO_2$
Depth Below Surface (cm)
0
50
100
150
200
300
200
100
0
THg (ng/g)
2016 Ambient $CO_2$
0
50
100
150
200
300
200
100
0
THg (ng/g)

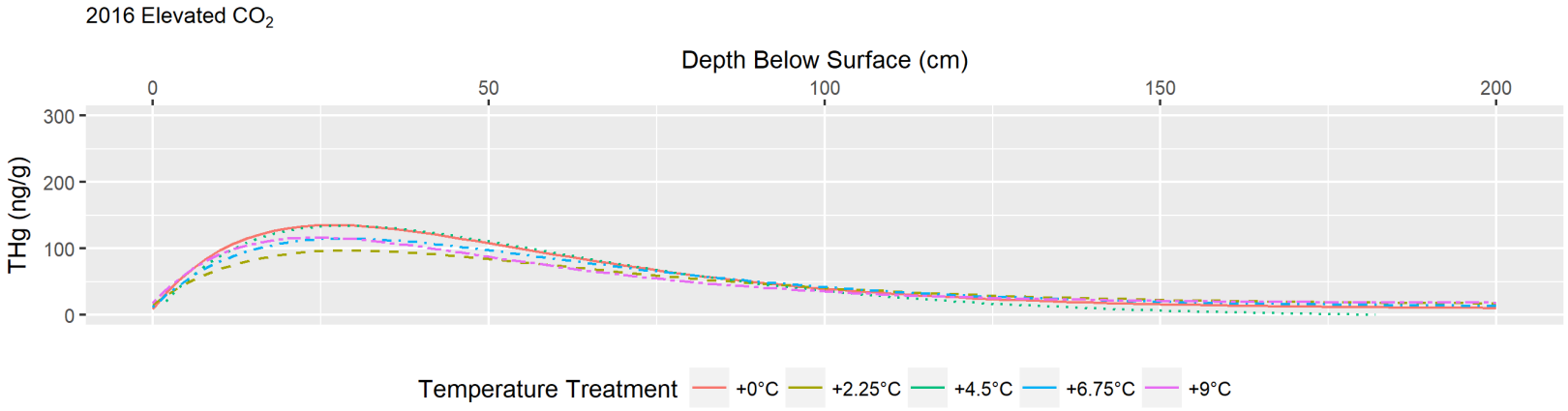
2016 Elevated $CO_2$
Depth Below Surface (cm)
0
50
100
150
200
300
200
100
0
THg (ng/g)
Temperature Treatment
+0°C
+2.25°C
+4.5°C
+6.75°C
+9°C

**Figure 5** Methylmercury (MeHg) Concentration Depth Profiles for Years 2012-2016

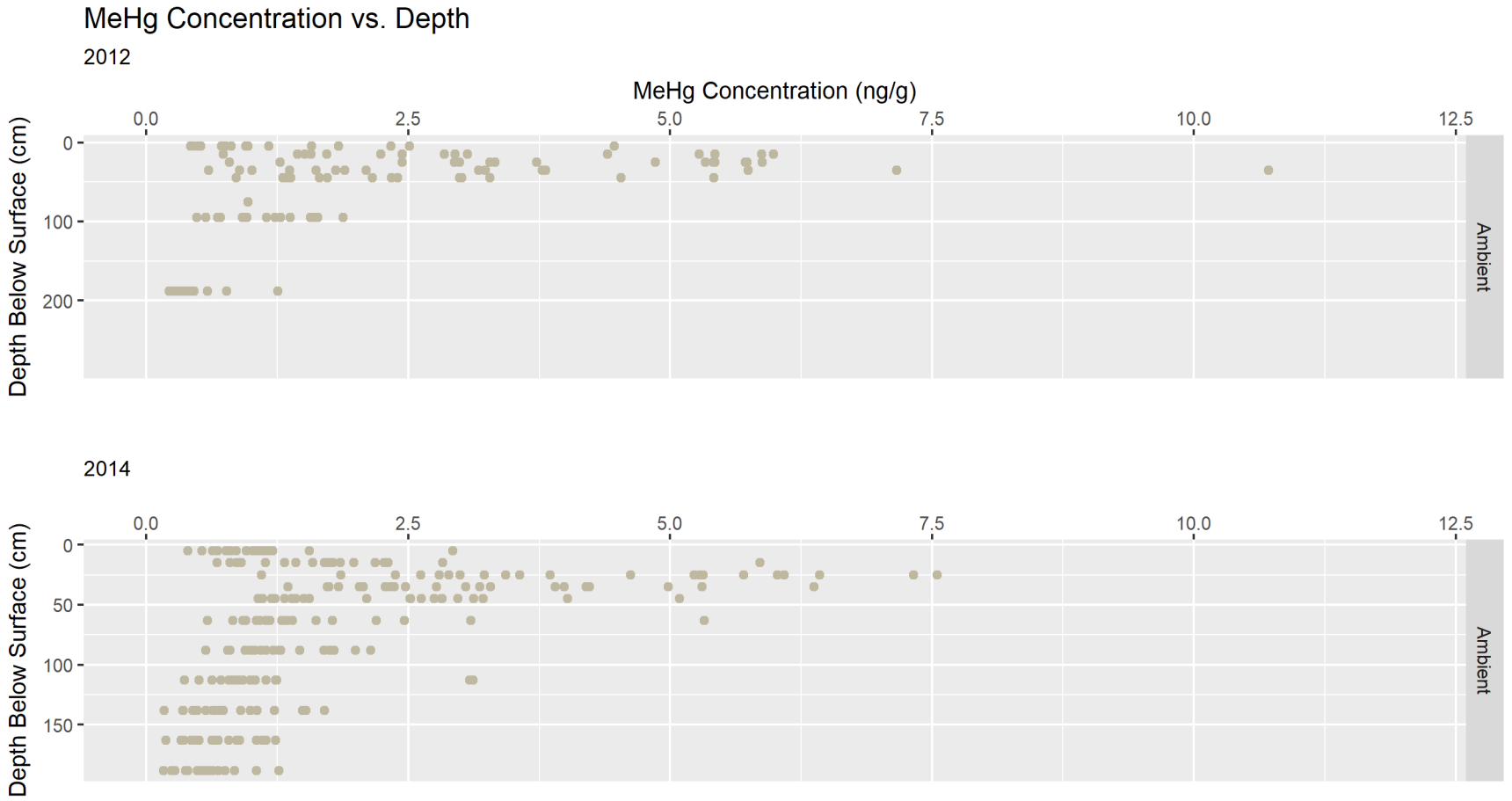

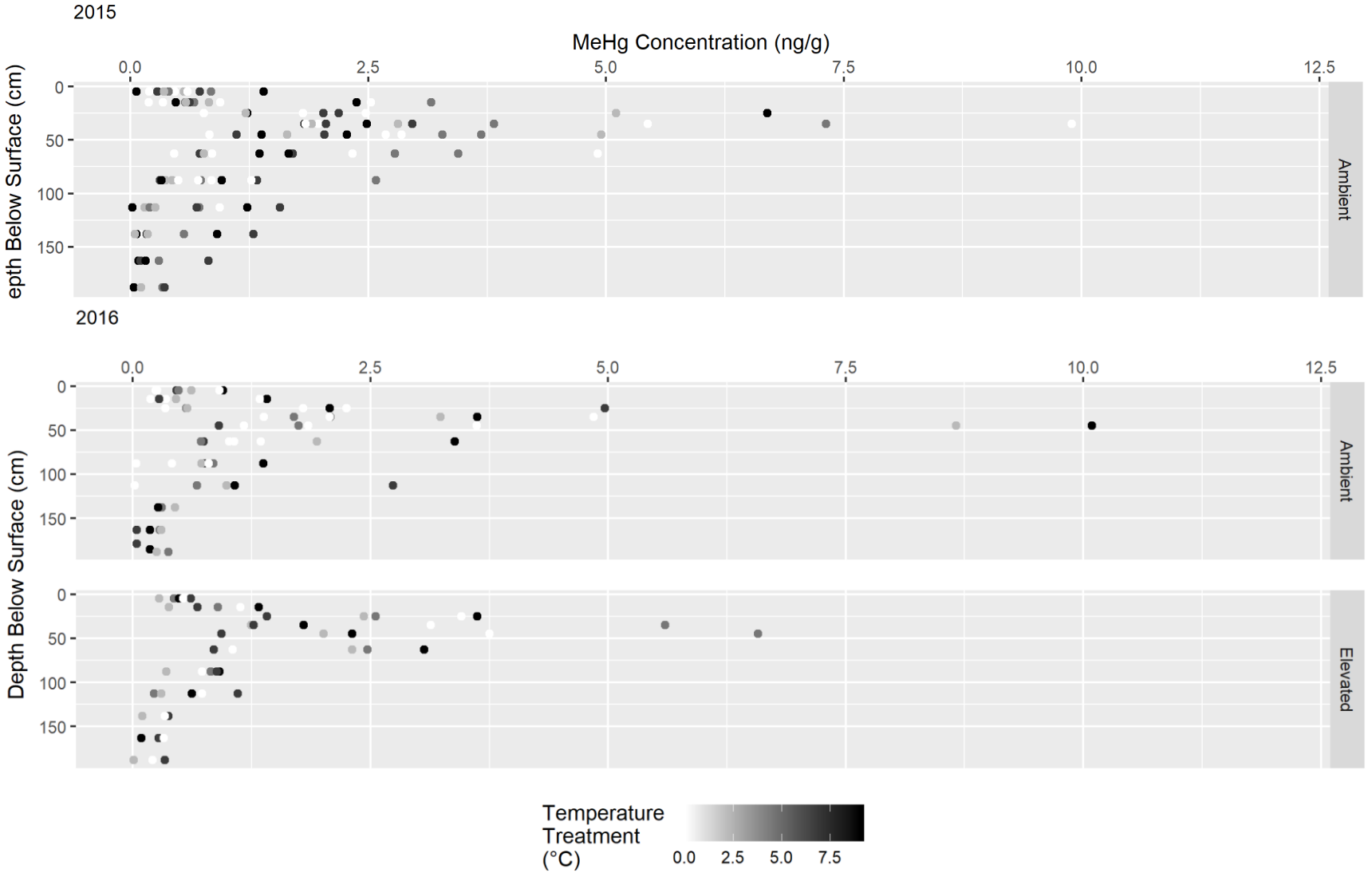
2015
MeHg Concentration (ng/g)
0.0
2.5
5.0
7.5
10.0
12.5
epth Below Surface (cm)
0
50
100
150
Ambient
2016
Depth Below Surface (cm)
Ambient
Elevated
Temperature
Treatment
(°C)
0.0
2.5
5.0
7.5

**Figure 6** Modeled Methylmercury (MeHg) Concentration Depth Profiles for Years 2012-2016

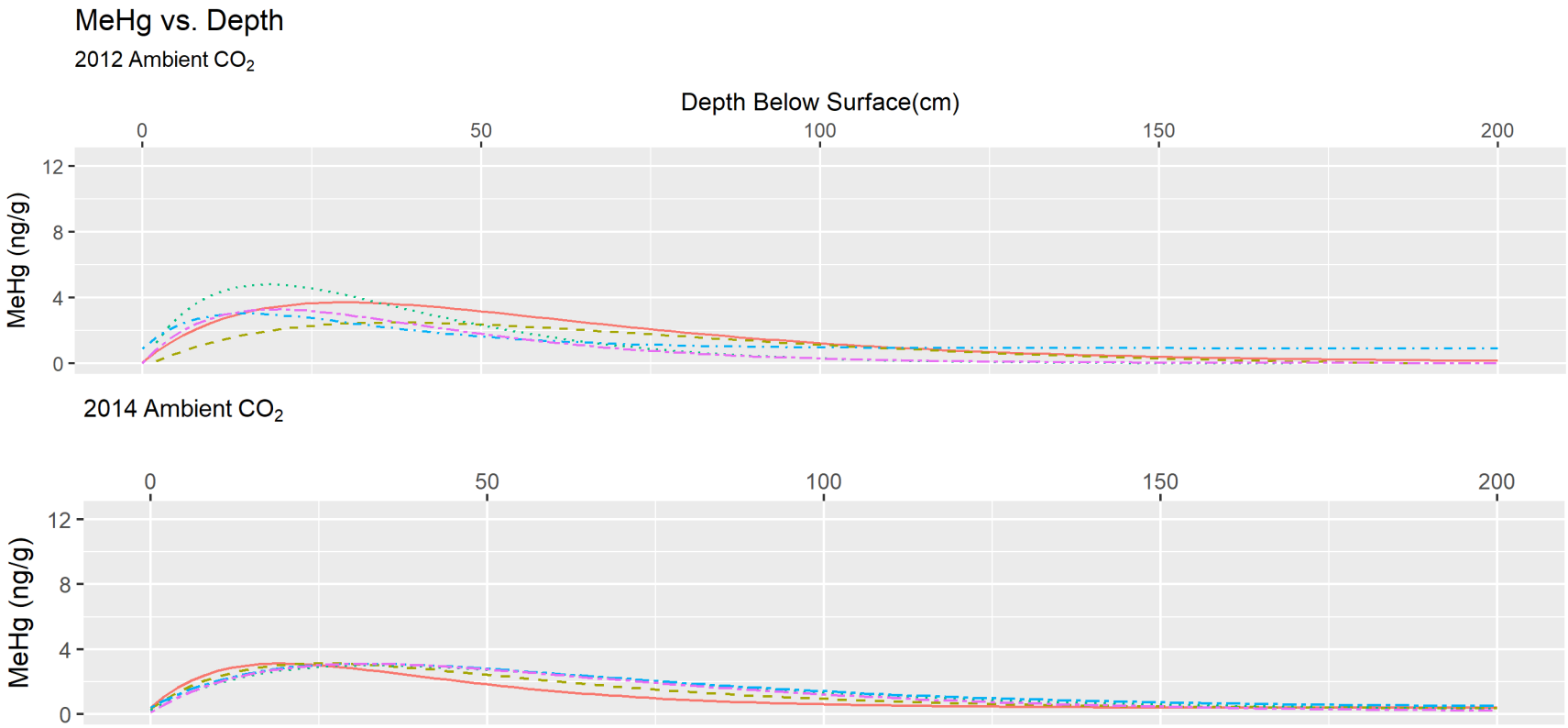

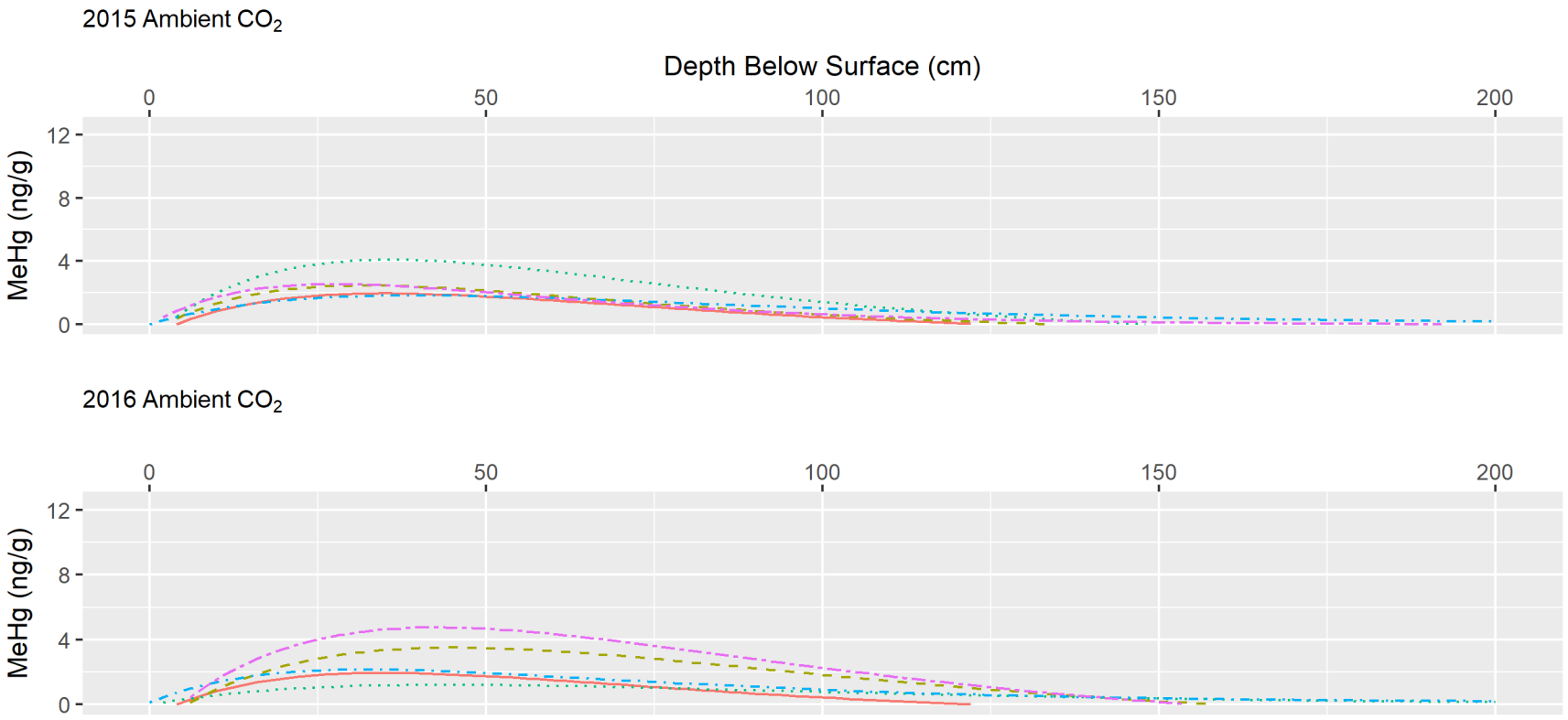
2015 Ambient $CO_2$
Depth Below Surface (cm)
0
50
100
150
200
MeHg (ng/g)
12
8
4
0
2016 Ambient $CO_2$
0
50
100
150
200
MeHg (ng/g)
12
8
4
0

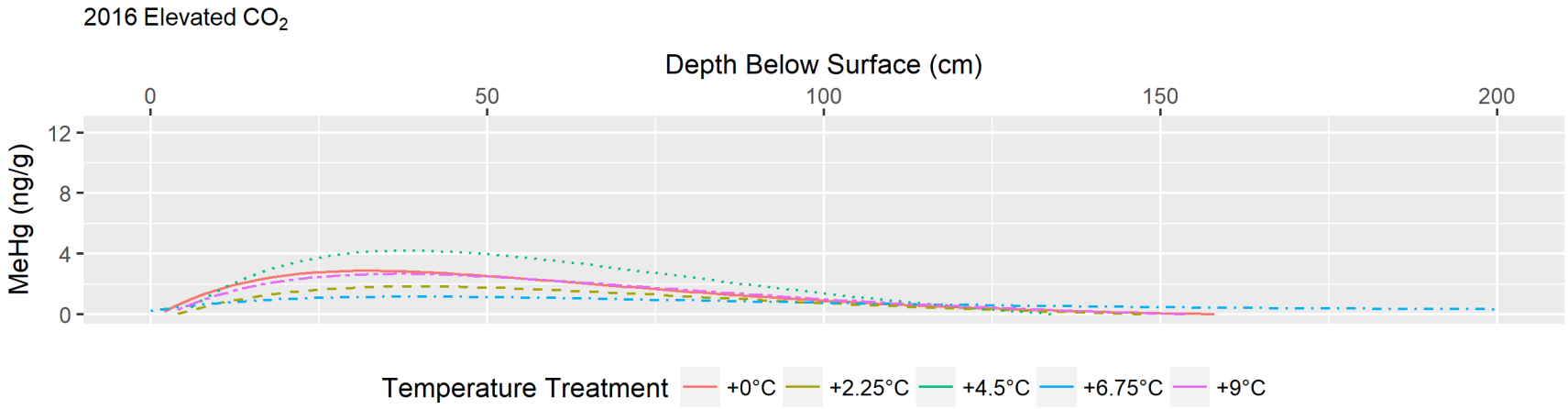
2016 Elevated $CO_2$
Depth Below Surface (cm)
0
50
100
150
200
MeHg (ng/g)
12
8
4
0
Temperature Treatment
+0°C
+2.25°C
+4.5°C
+6.75°C
+9°C

Depth profiles for both THg and MeHg demonstrate maximum THg and MeHg values occurring at some depth below the peat surface. Comparison of $THg_{max}$ and $MeHg_{max}$ values with increased temperature and/or increased atmospheric $CO_2$ was conducted to evaluate for any qualitative trends in 1) the magnitude of $THg_{max}$ or $MeHg_{max}$ or 2) the depth at which either $THg_{max}$ or $MeHg_{max}$ occurred, in order to determine the effect of simulated warming and $CO_2$ elevation on the THg pool overall as well as the production of MeHg in peat. In addition to $THg_{max}$ values, minimum THg values ($THg_{min}$), mean $THg_{max}$ values and the depth below the peat surface $THg_{max}$ occurred are reported in **Table 2-4**. Similarly, in addition to $MeHg_{max}$ values, minimum MeHg values ($MeHg_{min}$), mean $MeHg_{max}$ values and the depth below the peat surface at which $MeHg_{max}$ values occurred are reported in **Table 5-7**.

**Table 2** Mean Total Mercury (THg) Values for Years 2012-2016

| **Year** | **$THg_{min}$ (ng/g)** | **$THg_{max}$ (ng/g)** | **Mean $THg_{max}$ (ng/g) (obs.)** | **Mean $THg_{max}$ Depth (cm)** |
|---|---|---|---|---|
| 2012 | 22 | 249 | 161 (17) | 5-45 |
| 2014 | 8 | 157 | 132 (21) | 15-45 |
| 2015 | 14 | 270 | 188 (12) | 25-63 |
| 2016 | 9 | 165 | 144 (12) | 25-45 |

**Table 3** Minimum and Maximum Total Mercury (THg) Values for 2015

| Year | Temperature Treatment | $CO_2$ Treatment | $THg_{min}$ (ng/g) | $THg_{max}$ (ng/g) | $THg_{max}$ Depth (cm) |
|---|---|---|---|---|---|
| 2015 | +0°C | Ambient | 35.8 | 225.2 | 35 |
| 2015 | +0°C | Ambient | 89.6 | 170.2 | 35 |
| 2015 | +0°C | Ambient | 34.7 | 142.6 | 45 |
| 2015 | +0°C | Ambient | 63.8 | 188.5 | 25 |
| 2015 | +2.25°C | Ambient | 35.7 | 218.1 | 35 |
| 2015 | +2.25°C | Ambient | 31.5 | 171.6 | 25 |
| 2015 | +4.5°C | Ambient | 22.4 | 188.8 | 45 |
| 2015 | +4.5°C | Ambient | 40.6 | 269.8 | 25 |
| 2015 | +6.75°C | Ambient | 33.9 | 156.9 | 63 |
| 2015 | +6.75°C | Ambient | 14.1 | 153.4 | 25 |
| 2015 | +9°C | Ambient | 29.4 | 122.9 | 45 |
| 2015 | +9°C | Ambient | 38.8 | 251.5 | 25 |

**Table 4** Minimum and Maximum Total Mercury (THg) Values for 2016

| Year | Temperature Treatment | $CO_2$ Treatment | $THg_{min}$ (ng/g) | $THg_{max}$ (ng/g) | $THg_{max}$ Depth (cm) |
|---|---|---|---|---|---|
| 2016 | +0°C | Ambient | 17.1 | 135.0 | 25 |
| 2016 | +0°C | Ambient | 13.9 | 121.8 | 35 |
| 2016 | +0°C | Ambient | 30.0 | 158.9 | 25 |
| 2016 | +0°C | Elevated | 9.24 | 141.0 | 25 |
| 2016 | +2.25°C | Ambient | 25.6 | 138.5 | 35 |
| 2016 | +2.25°C | Elevated | 18.1 | 128.6 | 25 |
| 2016 | +4.5°C | Ambient | 25.8 | 125.0 | 35 |
| 2016 | +4.5°C | Elevated | 13.9 | 164.9 | 25 |
| 2016 | +6.75°C | Ambient | 11.5 | 152.7 | 25 |
| 2016 | +6.75°C | Elevated | 24.2 | 155.9 | 45 |
| 2016 | +9°C | Ambient | 9.14 | 163.9 | 35 |
| 2016 | +9°C | Elevated | 17.9 | 143.2 | 25 |

**Table 5** Mean Methylmercury (MeHg) Values for Years 2012-2016

| Year | $MeHg_{min}$ (ng/g) | $MeHg_{max}$ (ng/g) | Mean $MeHg_{max}$ (ng/g) (obs.) | Mean $MeHg_{max}$ Depth (cm) |
|---|---|---|---|---|
| 2012 | 0.220 | 10.7 | 5.46 (15) | 5-45 |
| 2014 | 0.166 | 7.55 | 4.57 (21) | 15-35 |
| 2015 | 0.020 | 9.90 | 4.44 (12) | 15-45 |
| 2016 | 0.011 | 10.1 | 4.31 (12) | 25-45 |

**Table 6** Minimum and Maximum Methylmercury (MeHg) Values for 2015

| Year | Temperature Treatment | $CO_2$ Treatment | $MeHg_{min}$ (ng/g) | $MeHg_{max}$ (ng/g) | $MeHg_{max}$ Depth (cm) |
|---|---|---|---|---|---|
| 2015 | +0°C | Ambient | 0.095 | 2.85 | 45 |
| 2015 | +0°C | Ambient | 0.192 | 5.44 | 35 |
| 2015 | +0°C | Ambient | 0.941 | 9.90 | 35 |
| 2015 | +0°C | Ambient | 0.462 | 2.53 | 15 |
| 2015 | +2.25°C | Ambient | 0.048 | 2.81 | 35 |
| 2015 | +2.25°C | Ambient | 0.113 | 5.11 | 25 |
| 2015 | +4.5°C | Ambient | 0.300 | 3.82 | 35 |
| 2015 | +4.5°C | Ambient | 0.203 | 7.32 | 35 |
| 2015 | +6.75°C | Ambient | 0.360 | 2.055 | 35 |
| 2015 | +6.75°C | Ambient | 0.105 | 2.96 | 35 |
| 2015 | +9°C | Ambient | 0.035 | 1.83 | 35 |
| 2015 | +9°C | Ambient | 0.020 | 6.69 | 25 |

**Table 7** Minimum and Maximum Methylmercury (MeHg) Values for 2016

| Year | Temperature Treatment | $CO_2$ Treatment | $MeHg_{min0}$ (ng/g) | $MeHg_{max}$ (ng/g) | $MeHg_{max}$ Depth (cm) |
|---|---|---|---|---|---|
| 2016 | +0°C | Ambient | 0.018 | 4.85 | 35 |
| 2016 | +0°C | Ambient | 0.037 | 1.38 | 35 |
| 2016 | +0°C | Ambient | 0.799 | 2.25 | 25 |
| 2016 | +0°C | Elevated | 0.205 | 3.75 | 45 |
| 2016 | +2.25°C | Ambient | 0.251 | 8.66 | 45 |
| 2016 | +2.25°C | Elevated | 0.011 | 2.43 | 25 |
| 2016 | +4.5°C | Ambient | 0.281 | 1.74 | 45 |
| 2016 | +4.5°C | Elevated | 0.223 | 6.58 | 45 |
| 2016 | +6.75°C | Ambient | 0.040 | 4.96 | 25 |
| 2016 | +6.75°C | Elevated | 0.274 | 1.41 | 25 |
| 2016 | +9°C | Ambient | 0.178 | 10.1 | 45 |
| 2016 | +9°C | Elevated | 0.089 | 3.62 | 25 |

### 3.2 Carbon (C), Nitrogen (N), Sulfur (S), and Reduced Sulfur ($S_{red}$) Depth Profiles

Results of $S_{red}$ analysis were plotted as $S_{red}$ (%) versus depth below the peat surface and displayed in **Figure 7**. At depths far below the peat surface, near 200 cm, the percentage of peat S in a chemically reduced form, presented here as $S_{red}$, is approximately 75% and then declines to around 50% towards the surface.

Percent total C concentrations for peat were plotted versus depth and are displayed in **Figure 8**. At depths far below the peat surface, near 200 cm, %C is approximately 50%, with a slight increase observed around 100 cm below the peat surface and then a decline to around 45% near the surface.

Percent total N concentrations for peat were plotted versus depth and are displayed in **Figure 9**. At depths far below the peat surface, around 200 cm, %N is approximately 2 to 3% and then declines to around 1% near the surface.

Percent total S concentrations for peat were plotted versus depth and are displayed in **Figure 10**. At depths far below the peat surface, near 200 cm, %S is approximately 0.2 to 0.3% and then declines to around 0.1% near the surface.

**Figure 7** Sulfur Reduced ($S_{red}$) Concentration Depth Profiles for Years 2012-2016

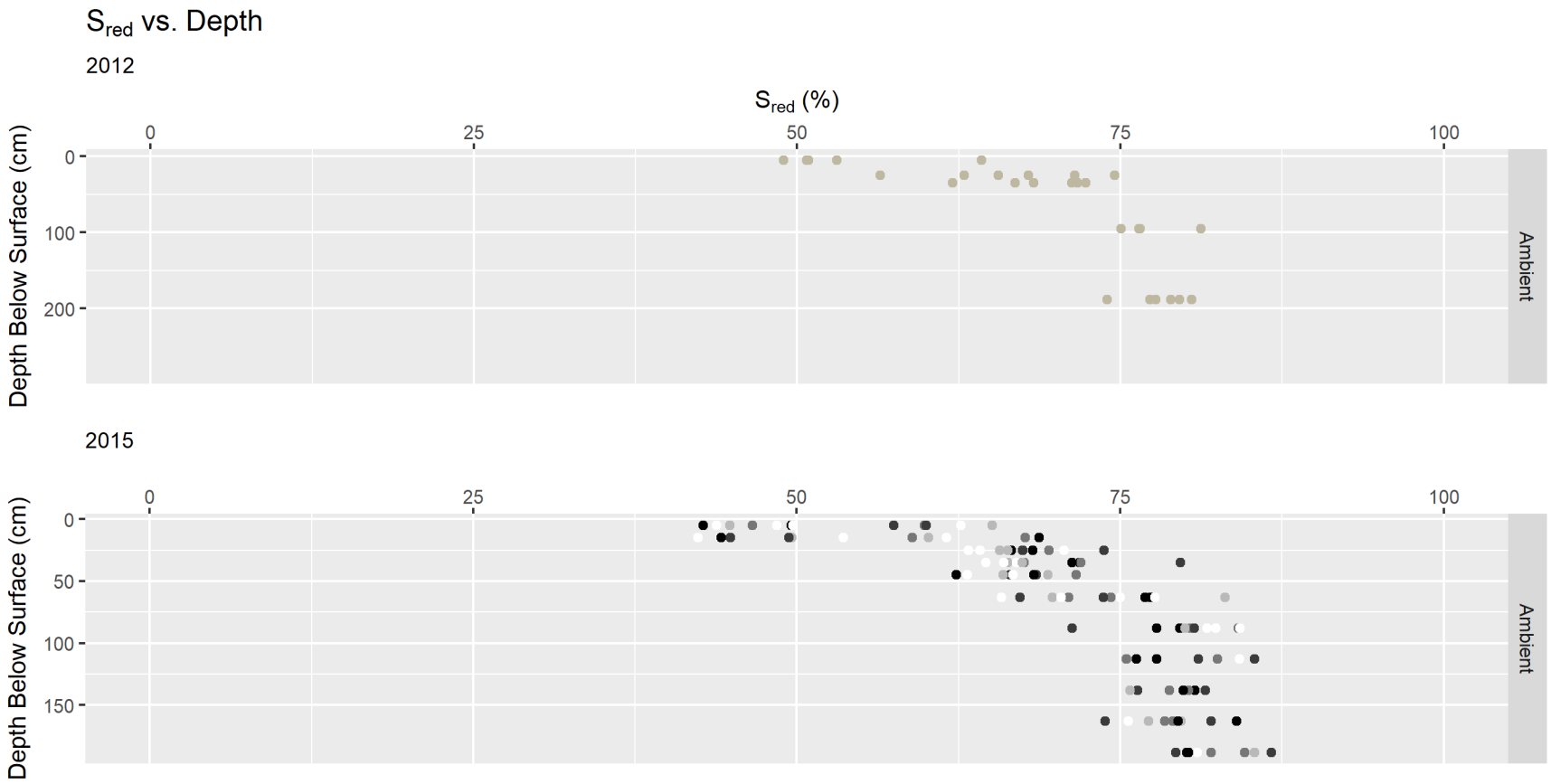

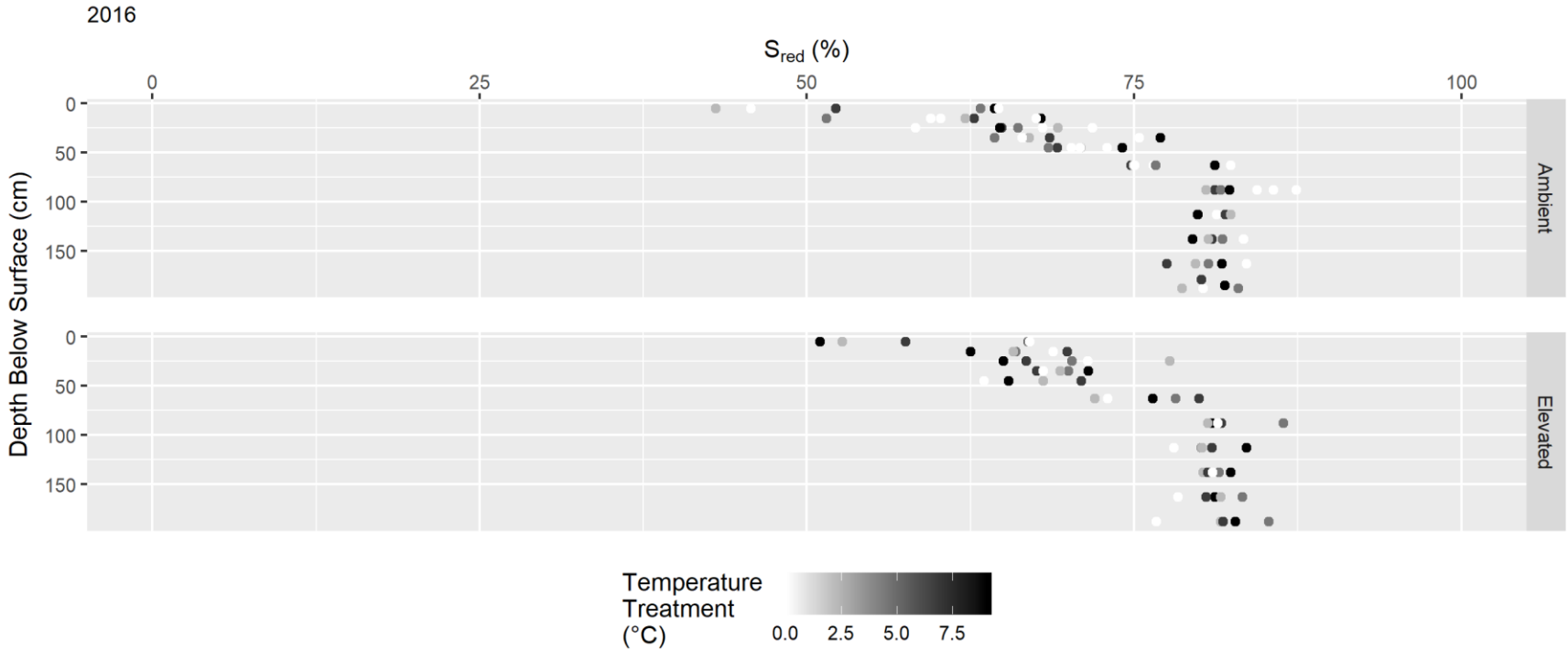
2016
$S_{red}$ (%)
0
25
50
75
100
Depth Below Surface (cm)
0
50
100
150
Ambient
Elevated
Temperature Treatment (°C)
0.0
2.5
5.0
7.5

**Figure 8** Percent Carbon (C) Depth Profiles for Years 2012-2016

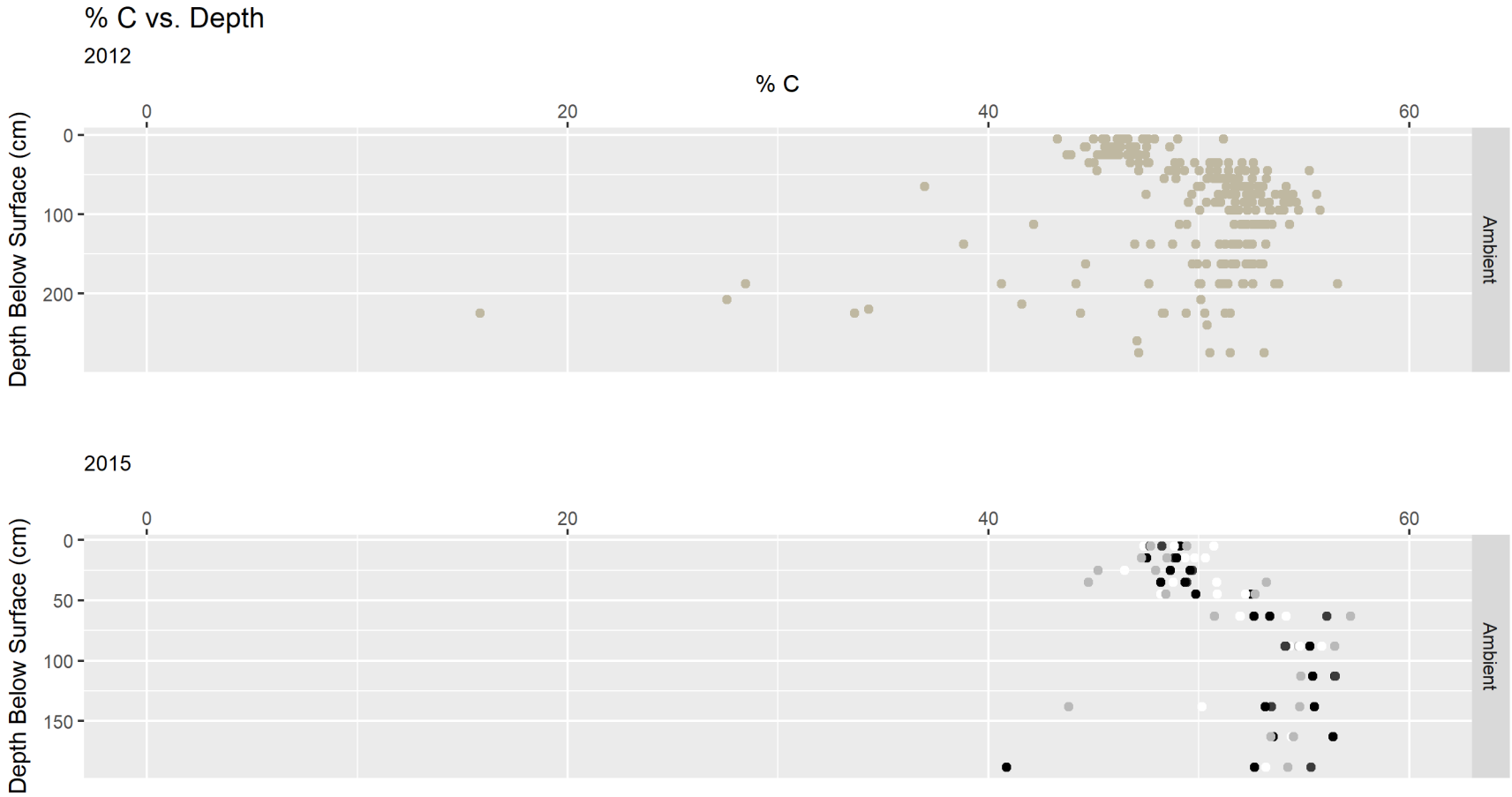

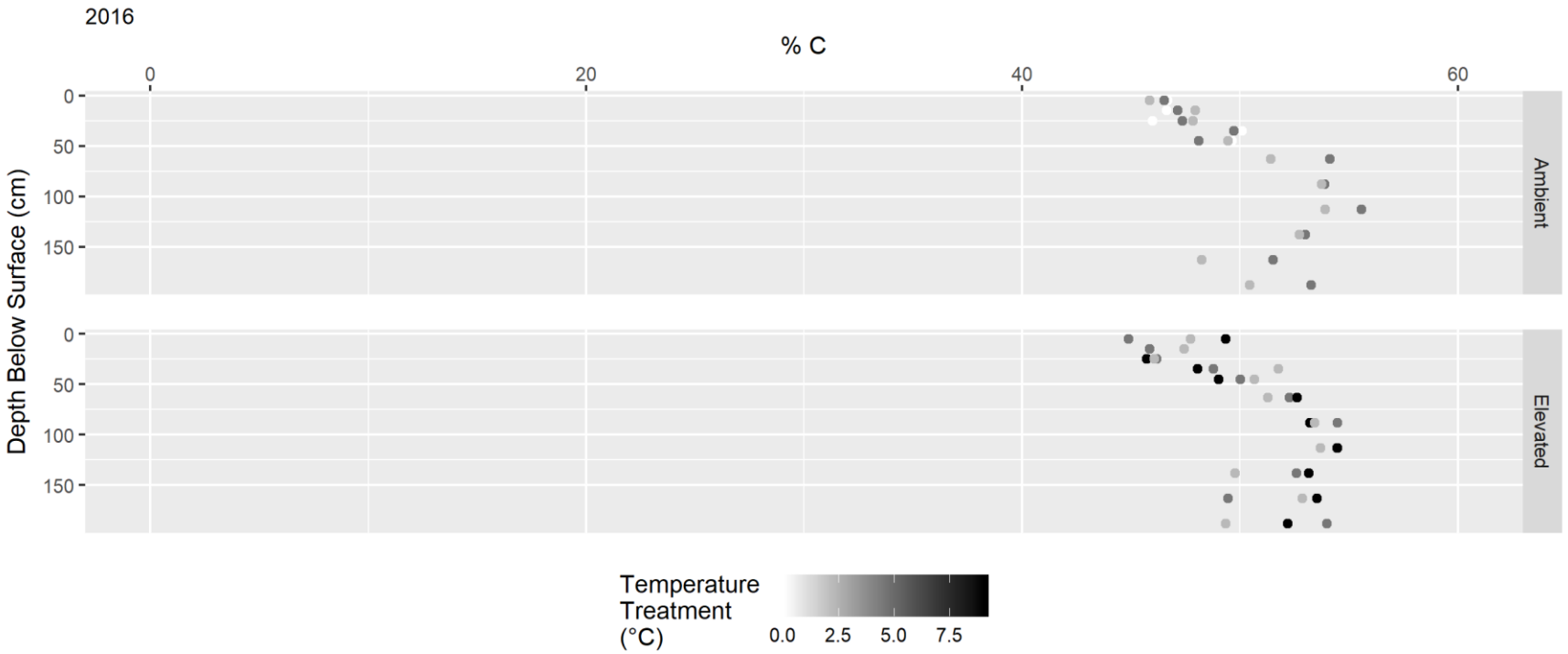
2016
% C
0
20
40
60
Depth Below Surface (cm)
0
50
100
150
Ambient
Elevated
Temperature Treatment (°C)
0.0
2.5
5.0
7.5

**Figure 9** Percent Nitrogen (N) Depth Profiles for Years 2012-2016

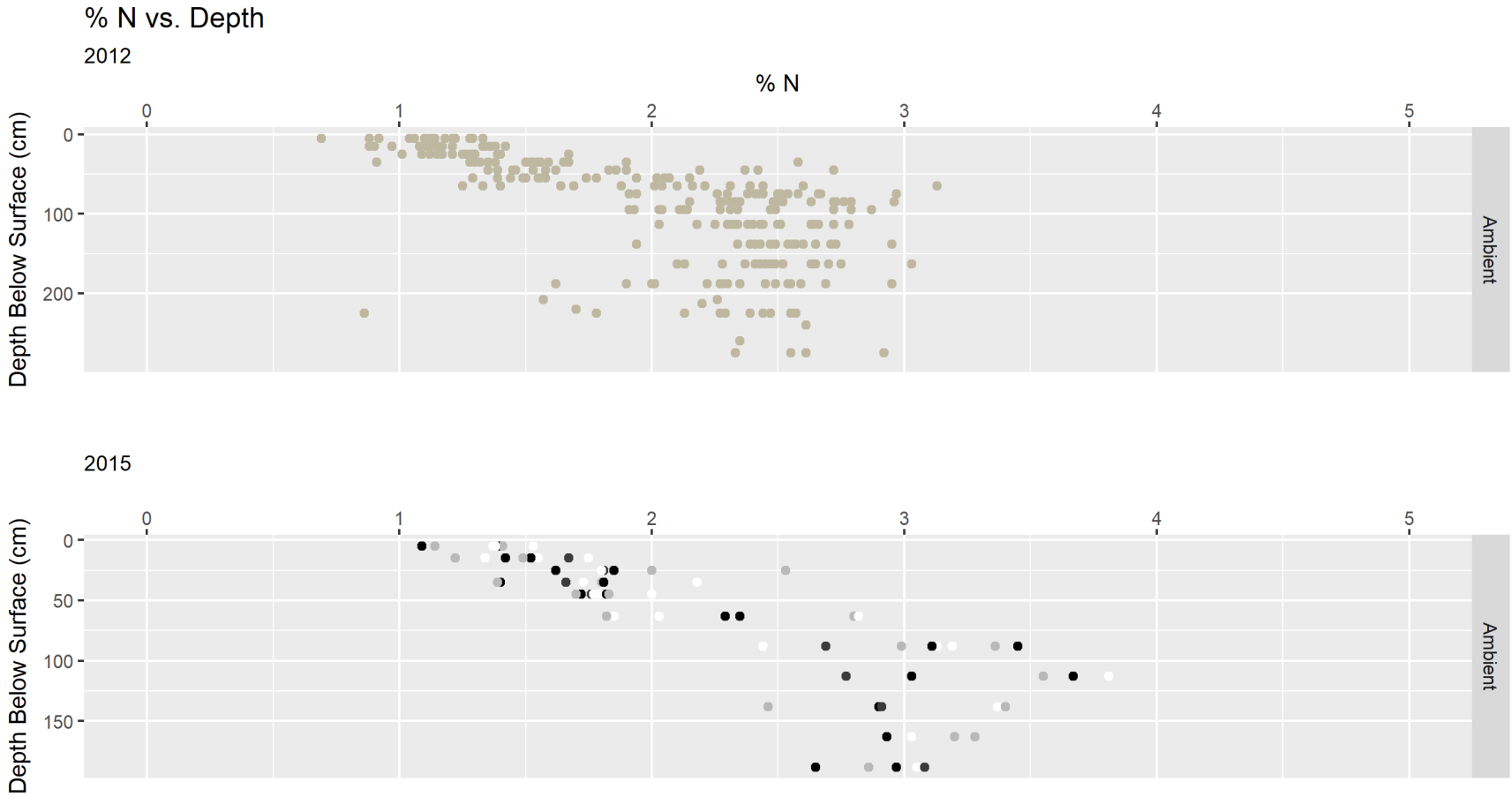

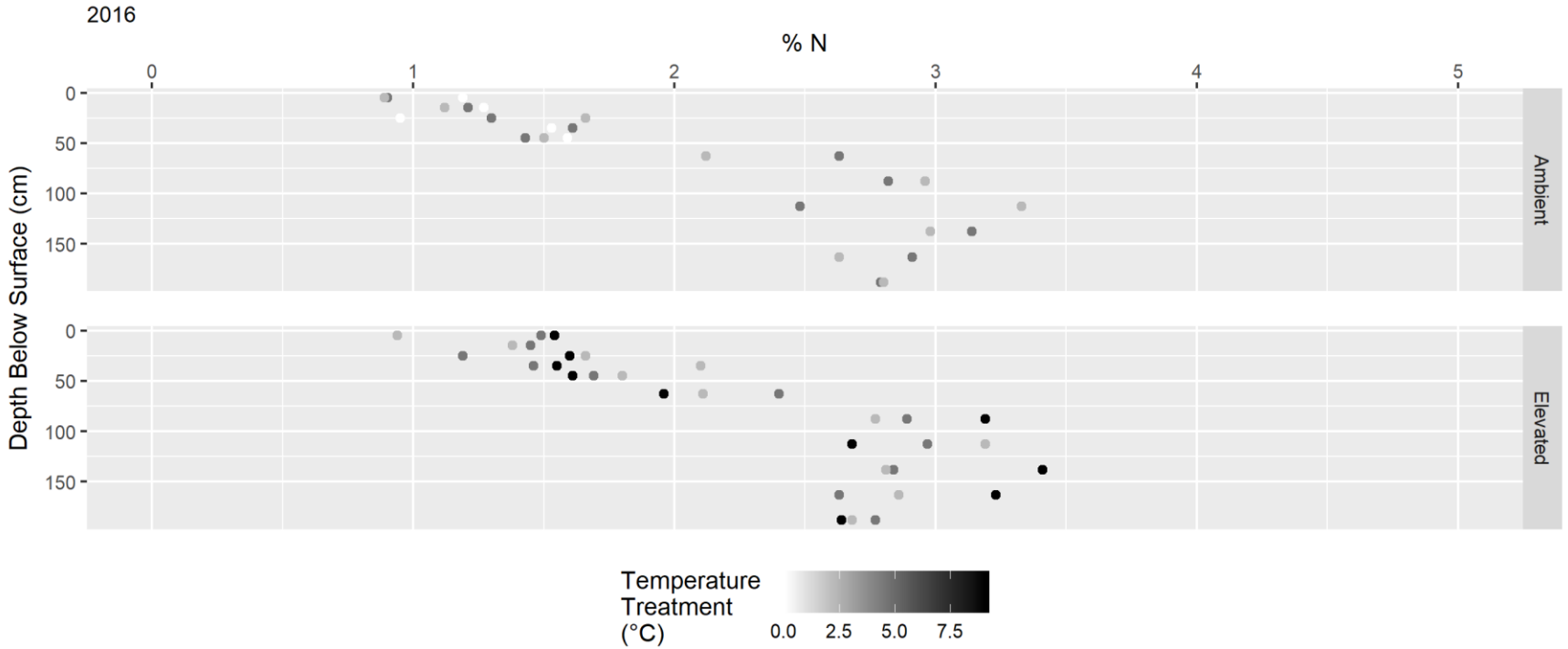
2016
% N
0
1
2
3
4
5
Depth Below Surface (cm)
0
50
100
150
Ambient
Elevated
Temperature Treatment (°C)
0.0
2.5
5.0
7.5

**Figure 10** Percent Sulfur (S) Depth Profiles for Years 2012-2016

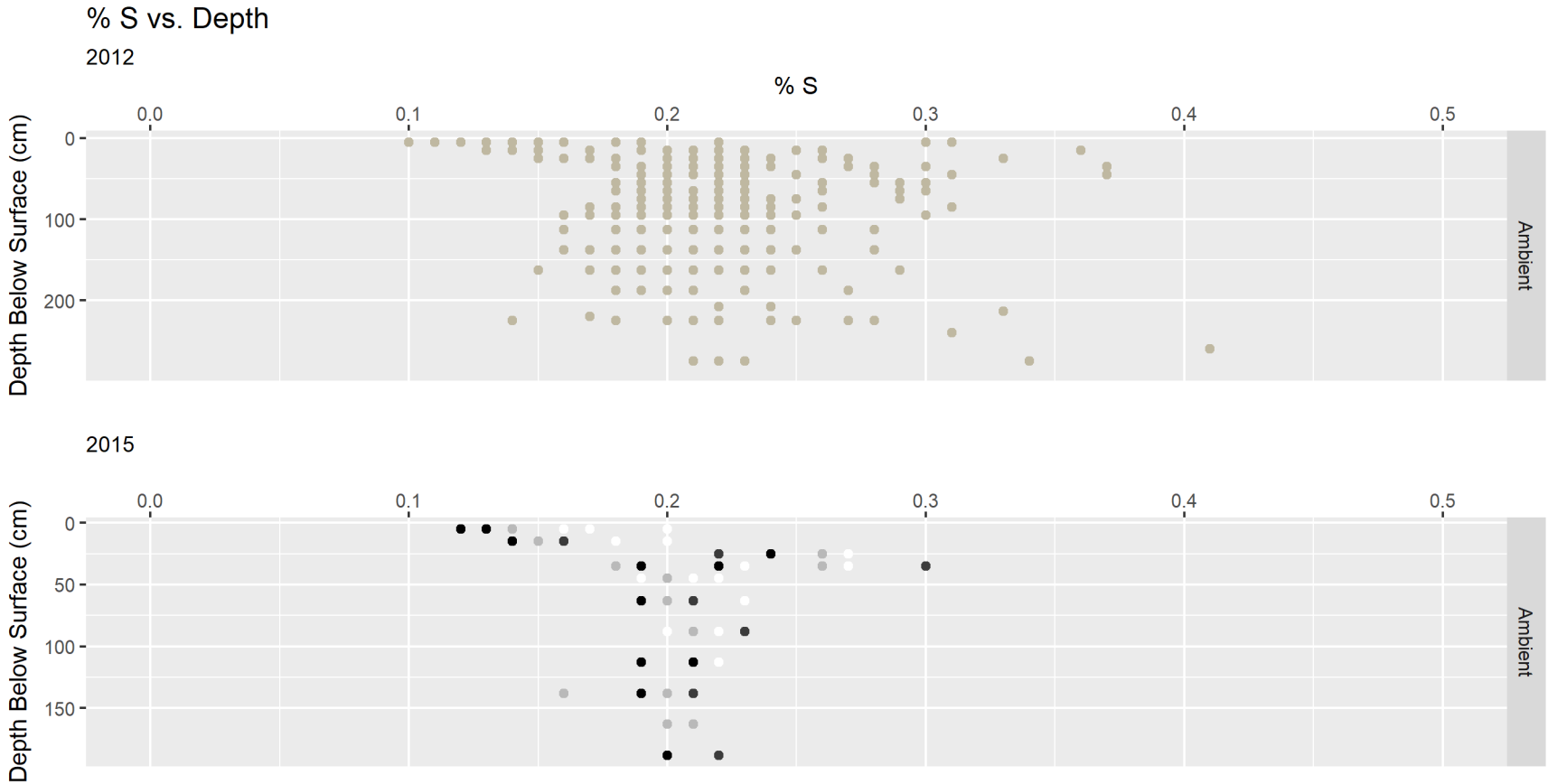

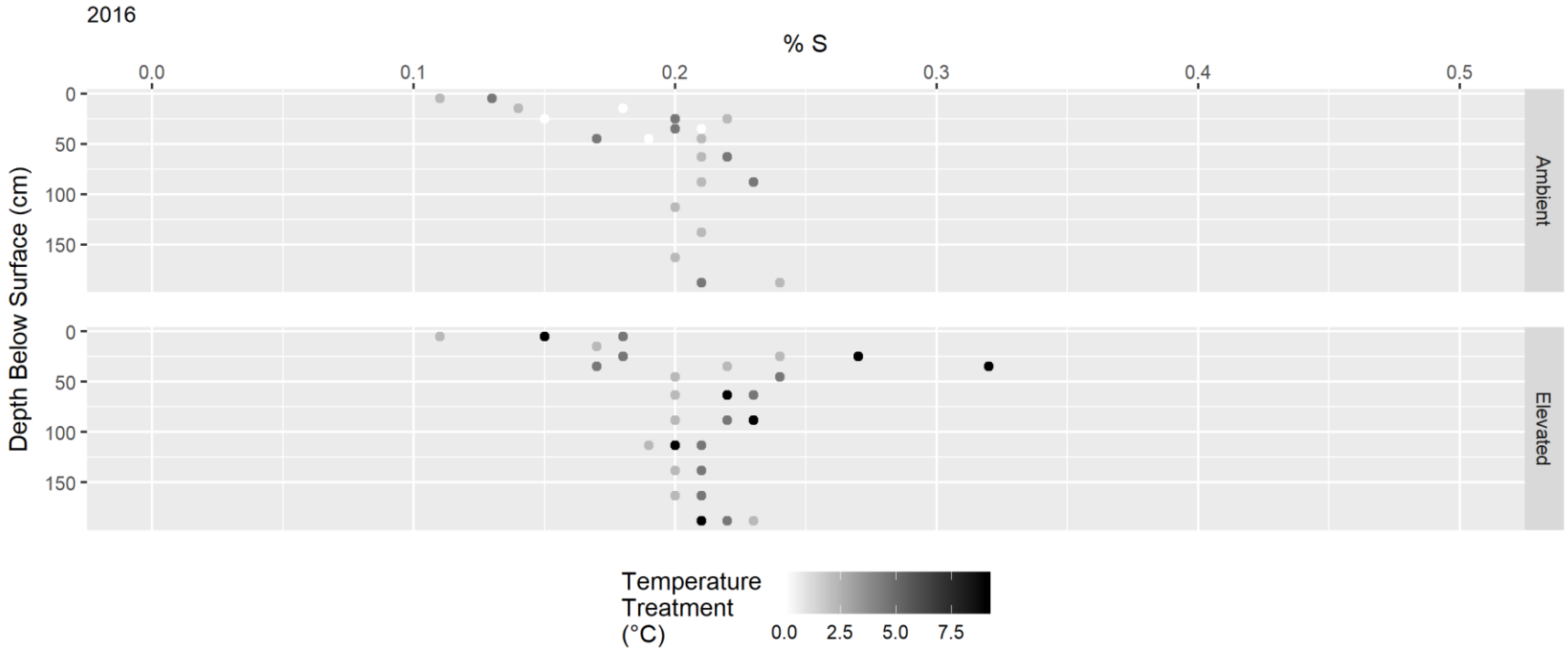
2016
% S
0.0
0.1
0.2
0.3
0.4
0.5
Depth Below Surface (cm)
0
50
100
150
Ambient
Elevated
Temperature Treatment (°C)
0.0
2.5
5.0
7.5

### 3.3 Maximum Total Mercury (THg) and Methylmercury (MeHg) Depth Profiles in 2016

In the present study, field sampling conducted in 2016 is the only sample set that experienced above ground heating, below ground heating, and elevated $CO_2$ concentrations. To investigate the depth profile characteristics of THg and MeHg with the full experimental treatment, $THg_{max}$ and $MeHg_{max}$ values were calculated for just the 2016 samples. Results of $THg_{max}$ analysis were plotted versus temperature and displayed in **Figure 11**. Following linear regression, the relationship between $THg_{max}$ and temperature was not found to be significant ($R^2$ = -0.0125). Results of $MeHg_{max}$ analysis were plotted versus temperature and displayed in **Figure 12**. Following linear regression, the relationship between $MeHg_{max}$ and temperature was not found to be significant ($R^2$ = -0.02388).

**Figure 11** Maximum Total Mercury ($THg_{max}$) Depth vs. Temperature Treatment

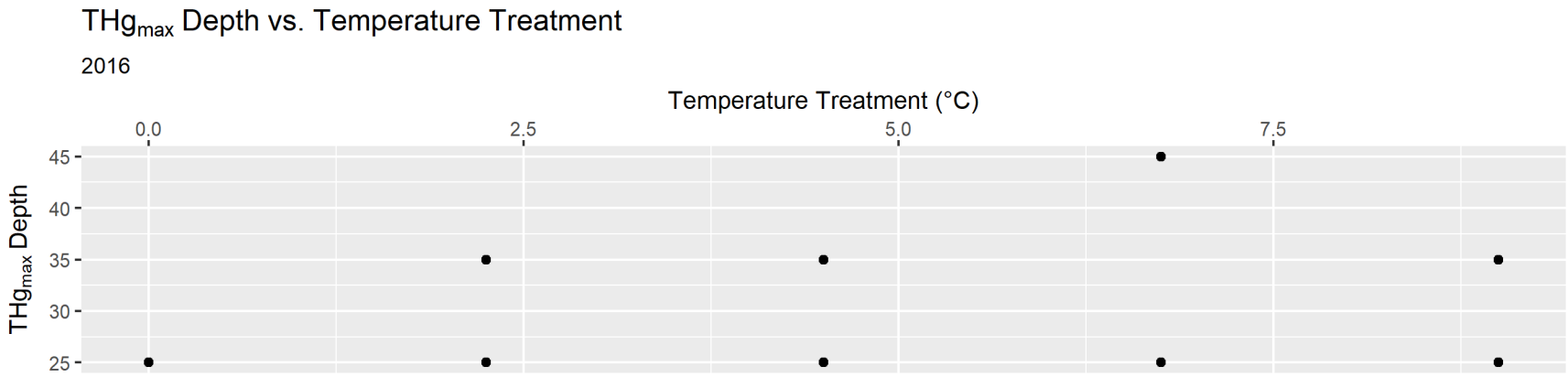


**Figure 12** Maximum Methylmercury ($MeHg_{max}$) Depth vs. Temperature Treatment

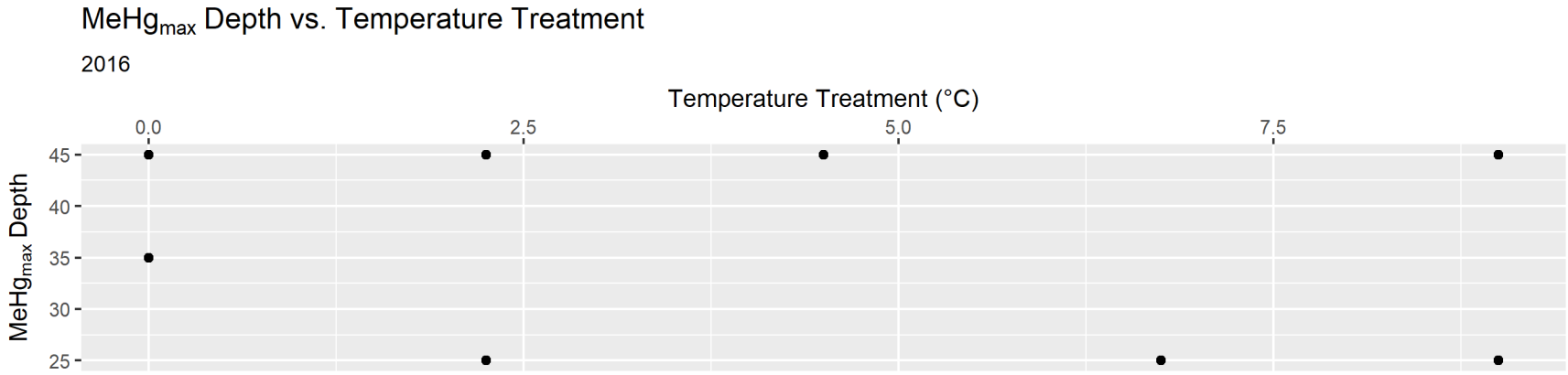

### 3.4 Multiple Linear Regression Analysis of Total Mercury (THg) Depth Profiles

A correlation matrix was generated including each of the relevant variables (temperature treatment, $CO_2$ elevation, depth, bulk density, log MeHg, log THg, log $S_{red}$, log %S, log %N, and log %C) in this study to determine the most significant relationships between variables. Correlation coefficient (R) values are displayed in a visual correlation matrix as shown in **Figure 13** and important relationships between variables are apparent. Paired variables with the largest positive R values were found between depth and log $S_{red}$ ($R = 0.72$), log MeHg and log THg ($R = 0.64$), log %N and log $S_{red}$ ($R = 0.62$), and depth and log %N ($R = 0.59$). The paired variables with the largest (absolute) negative R values were found between depth and log THg ($R = -0.66$), log %N and log THg ($R = -0.54$), and depth and log MeHg ($P = -0.53$). Final equations obtained from multiple linear regression for THg and MeHg are shown in **Equation 3** and **Equation 4**.

**Figure 13** Correlation Matrix for Multiple Linear Regression

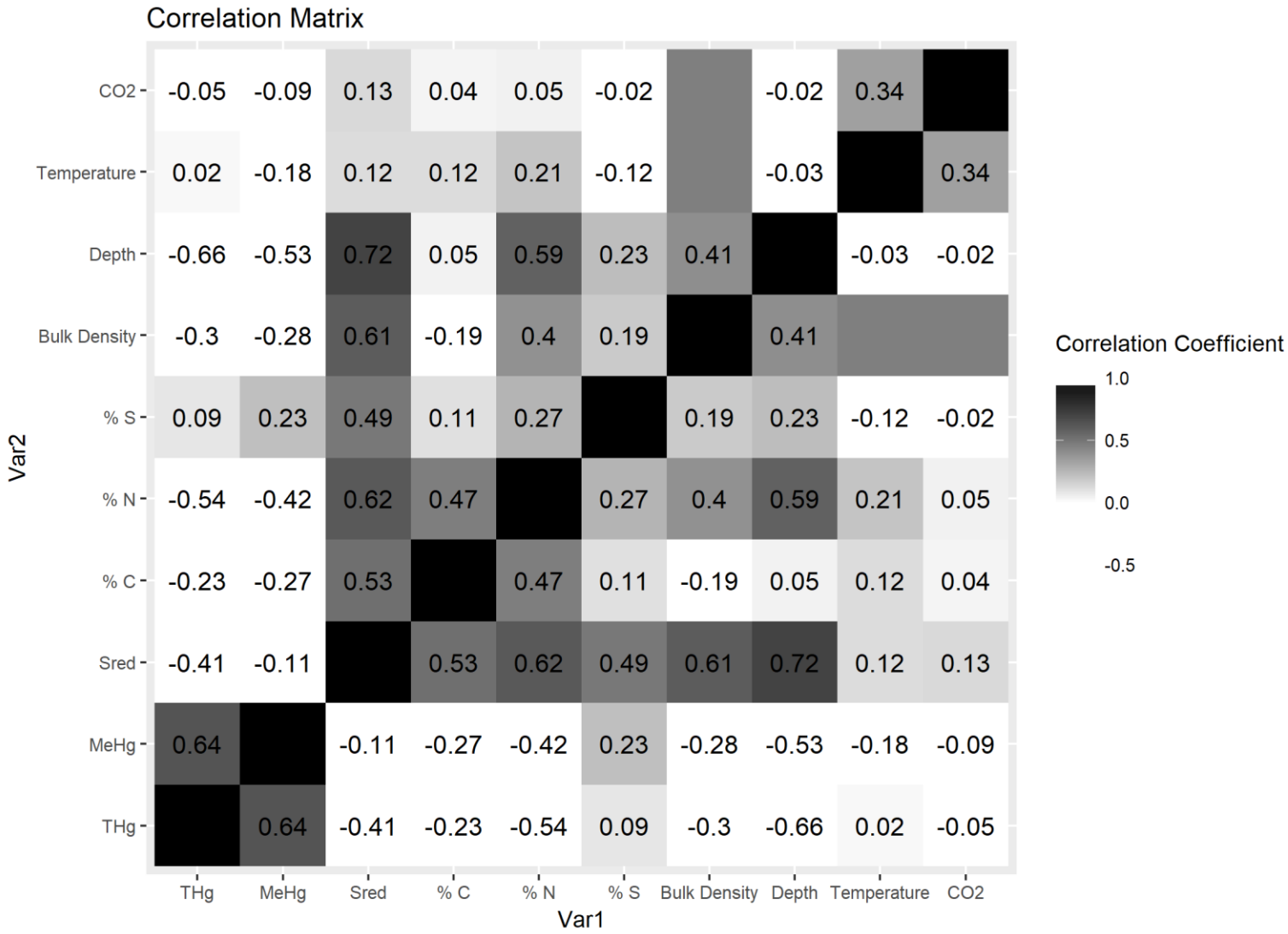

Multiple linear regression for the dependent variable log THg was conducted for the following independent variables: depth, temperature treatment, $CO_2$ treatment, bulk density, log %C, log %N, log %S, and log $S_{red}$. Total mercury values were log normalized based on qualitative analysis of histograms and residual plots, as shown in **Figures 14-19**. Histograms for THg (non-log) and log THg were generated and displayed in **Figure 14** and **Figure 15**, respectively. THg analysis revealed a bimodal histogram with non-normal distribution (**Figure 14**) and log transformation of THg gave a bimodal histogram with non-normal distribution (**Figure 15**). Log transformation was preferred for analysis of THg based on the significant improvement in $R^2$ values observed with log transformation.

The relationship between log THg and depth was found to be most significant ($R^2 = 0.4314$, $p < 0.05$). Linear regression was repeated between log THg + depth and remaining variables (temperature treatment, $CO_2$ treatment, bulk density, log %C, log %N, log %S, and log $S_{red}$). The relationship between log THg + depth and log %S was found to be most significant ($R^2 = 0.4476$, $p < 0.05$). Linear regression was repeated between log THg + depth + log %S and remaining variables (temperature treatment, $CO_2$ treatment, bulk density, log %C, log %N, and log $S_{red}$). The relationship between log THg + depth + log %S and log %N was found to be most significant ($R^2 = 0.4888$, $p < 0.05$). Linear regression was repeated between log THg + depth + log %S + log %N and remaining variables (temperature treatment, $CO_2$ treatment, bulk density, log %C, and log $S_{red}$). No additional significant relationship between log THg + depth + log %S + log %N and any of the remaining variables was found (**AA-91**).

Based on linear regression, therefore, results of THg linear regression, displayed

in **Table 8**, indicate a predictable relationship between log THg, depth, and log %S according to the following equation:

$$\log THg = -0.003*Depth + 0.79*\log \%S + 2.5 \quad (\textbf{Equation 3})$$

Calculation of AIC and BIC values revealed an improvement in AIC and BIC values with the incorporation of depth and log %S (**Table 9**), however, with the addition of log %N, AIC and BIC values did not improve, therefore, log %N was removed from the final linear regression equation (**AA-91**). Calculation of VIF values confirmed that independent variables included in the linear regression model were not co-variant (**Table 10**). Please refer to **Figure 34** of the appendix (**AA-91**) for original spreadsheets containing multiple linear regression calculations and values for log THg.

**Table 8** $Log_{10}$ Transformed Total Mercury (THg) Estimated Values, Standard Error, t Values and p Values

| | **Linear Regression Statistical Values for log THg** | | | |
|---|---|---|---|---|
| **Variable** | **Estimate** | **Standard Error** | **t Value** | **p Value** |
| (Intercept) | 2.548452924 | 0.086720515 | 29.38696708 | 5.67E-100 |
| Depth | -0.00290629 | 0.000165618 | -17.54815845 | 5.99E-51 |
| log % S | 0.790139093 | 0.11915803 | 6.631018445 | 1.14E-10 |

**Table 9** $Log_{10}$ Transformed Total Mercury (THg) $R^2$, Akaike Information Criterion (AIC), and Bayesian Information Criterion (BIC) Values

| **Linear Regression Statistical Values for log THg** | |
|---|---|
| **Adjusted $R^2$** | 0.4888 |
| **AIC** | -174.6588 |
| **BIC** | -154.8926 |

**Table 10** $Log_{10}$ Transformed Total Mercury (THg) Variance Inflation Factor (VIF) Values

| **Log THg Variance Inflation Factor (VIF)** | | |
|---|---|---|
| **Variable** | Depth | log % S |
| **VIF** | 1.066815 | 1.066815 |

Residual plots for the multiple linear regression of log THg as a function of depth and %S were generated and displayed in **Figure 16**. The black line displayed is a loess weighted regression. Visual inspection of the log THg residual plots where log THg is modeled as a function of depth and %S indicate that residual values are evenly dispersed around the horizontal axis (**Figure 16**). Residual normal quantile-quantile (Q-Q) plots for the linear regression of log THg as a function of depth and %S were generated and displayed in **Figure 17**. Visual inspection of the log THg residual normal Q-Q plot where log THg is modeled as a function of depth and %S indicates that the residuals are normally distributed between the theoretical quantile (TQ) range of -2 and 2, with some variability observed in the outermost regions (TQ < -2 or > 2) (**Figure 17**). Scale-location plots for the linear regression of log THg as a function of depth and %S were generated and displayed in **Figure 18**. Visual inspection of **Figure 18** indicates that residuals are spread equally along the range of fitted values, therefore, fulfilling the assumption of equal variance i.e. residuals are homoscedastic.

Residual vs. leverage plots for the linear regression of log THg as a function of depth and %S were generated and displayed in **Figure 19**. The black dotted line displayed the loess weighted regression and the black dashed line indicates a linear regression. Visual inspection of **Figure 19** indicates normal distribution about the horizontal axis. Added variable plots for the linear regression of log THg as a function of depth and log %S were generated separately and are displayed in **Figure 20** and **Figure 21**. Visual inspection of both **Figure 20** and **Figure 21** show a non-zero slope which indicates that the addition of both depth and log %S have significant effects on the linear regression model overall.

**Figure 14** Untransformed Total Mercury (THg) Histogram Plot

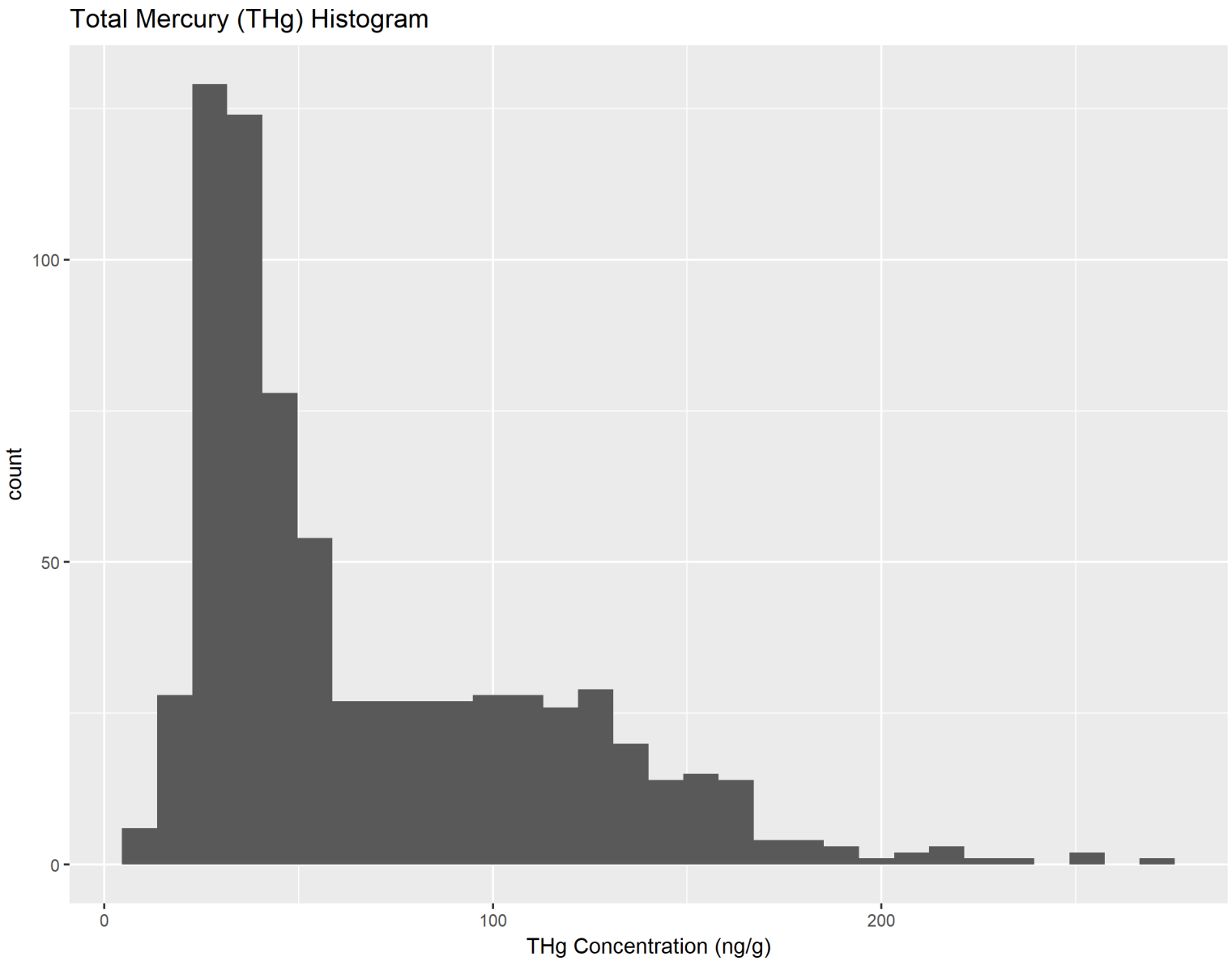

**Figure 15** $Log_{10}$ Transformed Total Mercury (THg) Histogram Plot

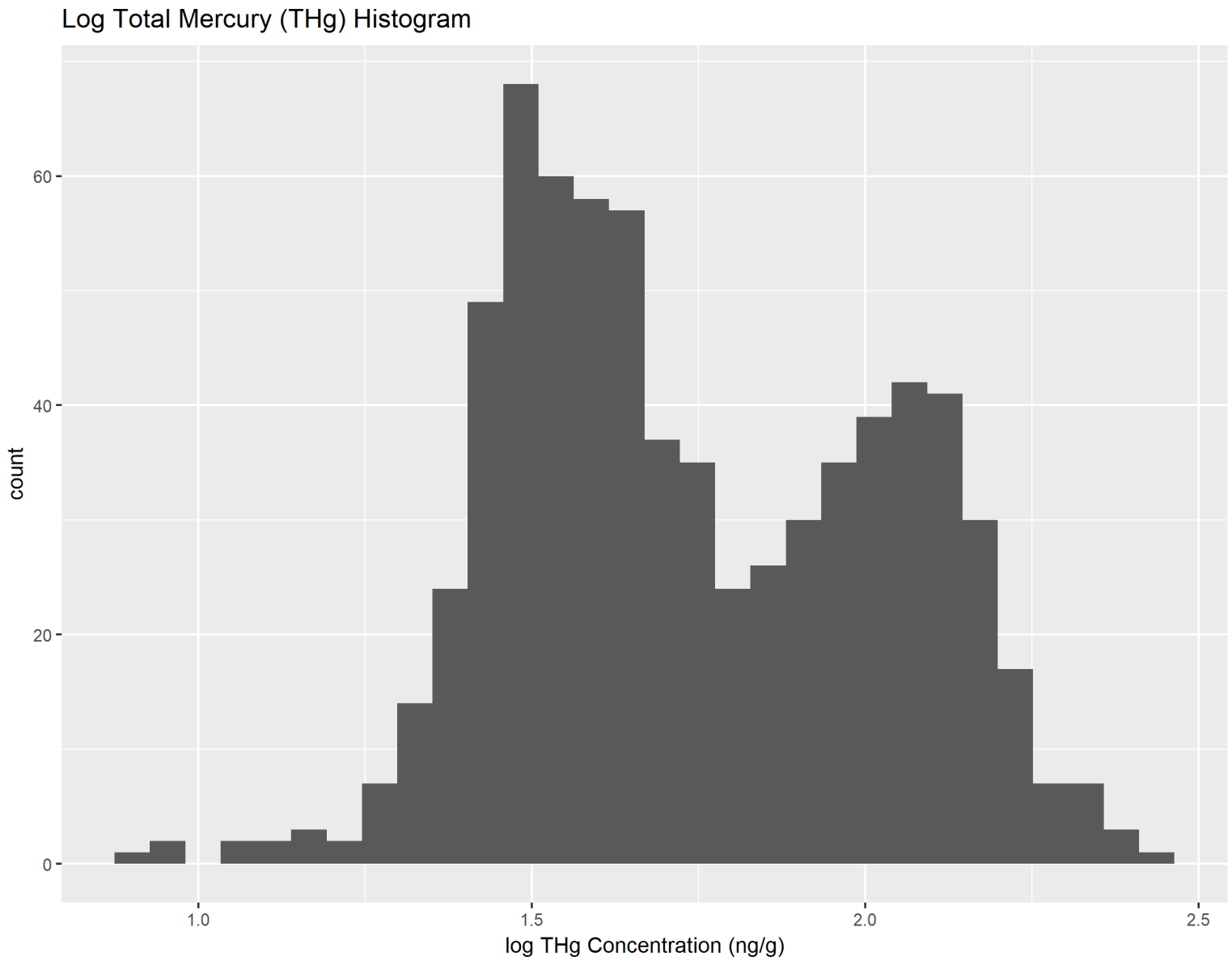

**Figure 16** $Log_{10}$ Transformed Total Mercury (THg) Residuals vs. Fitted Values Plot

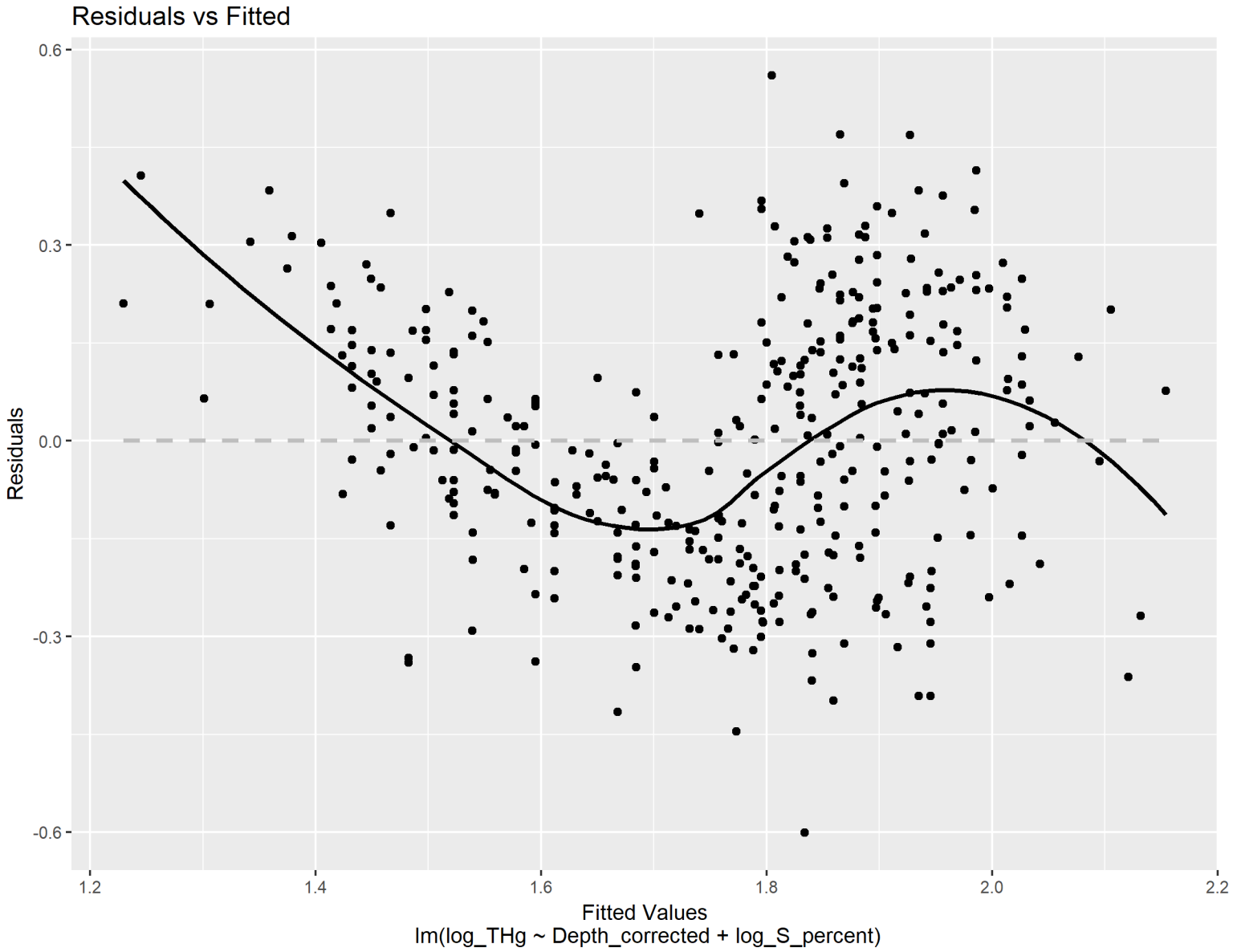

**Figure 17** $Log_{10}$ Transformed Total Mercury (THg) Q-Q Plot

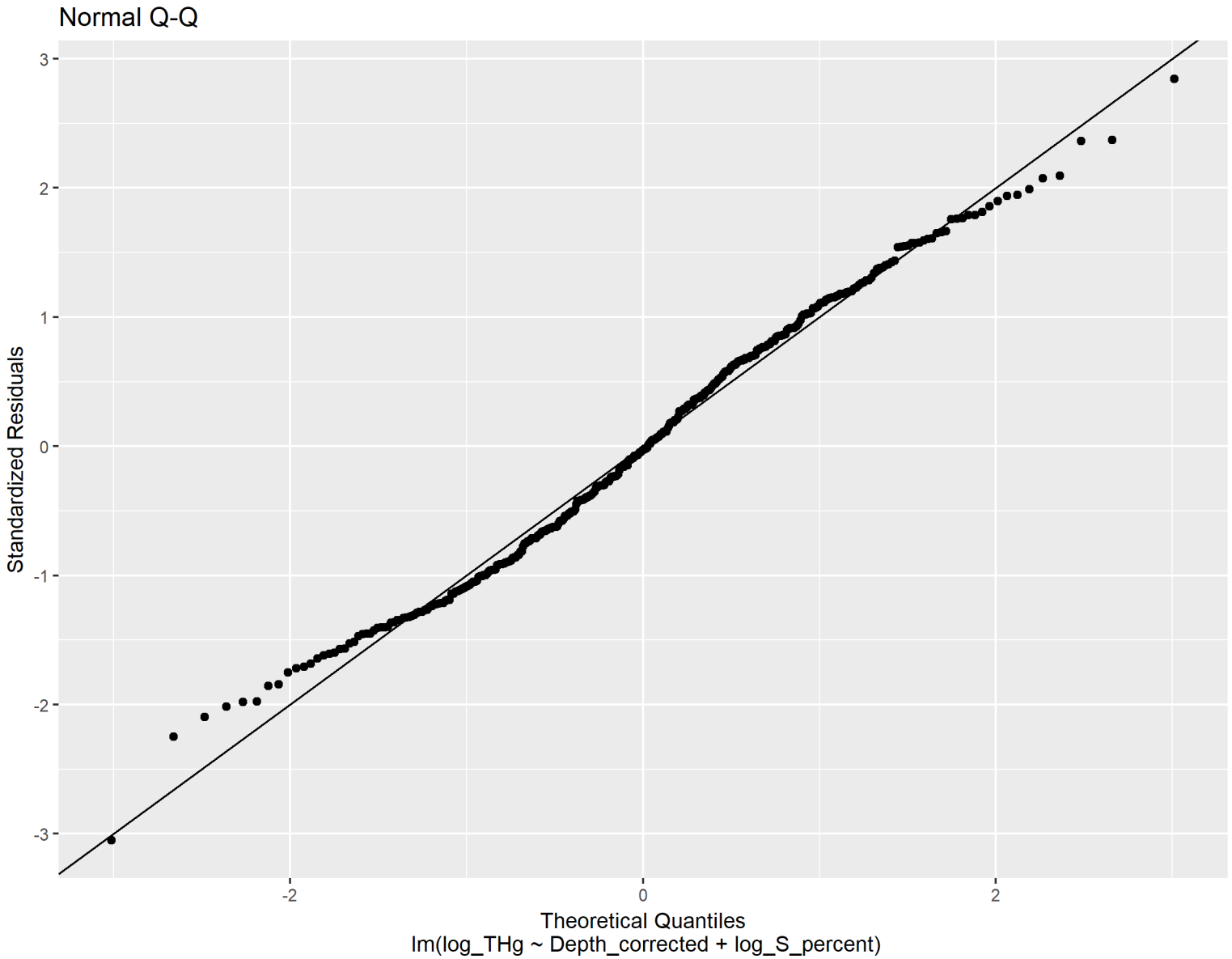

**Figure 18** $Log_{10}$ Transformed Total Mercury (THg) Scale-Location Plot

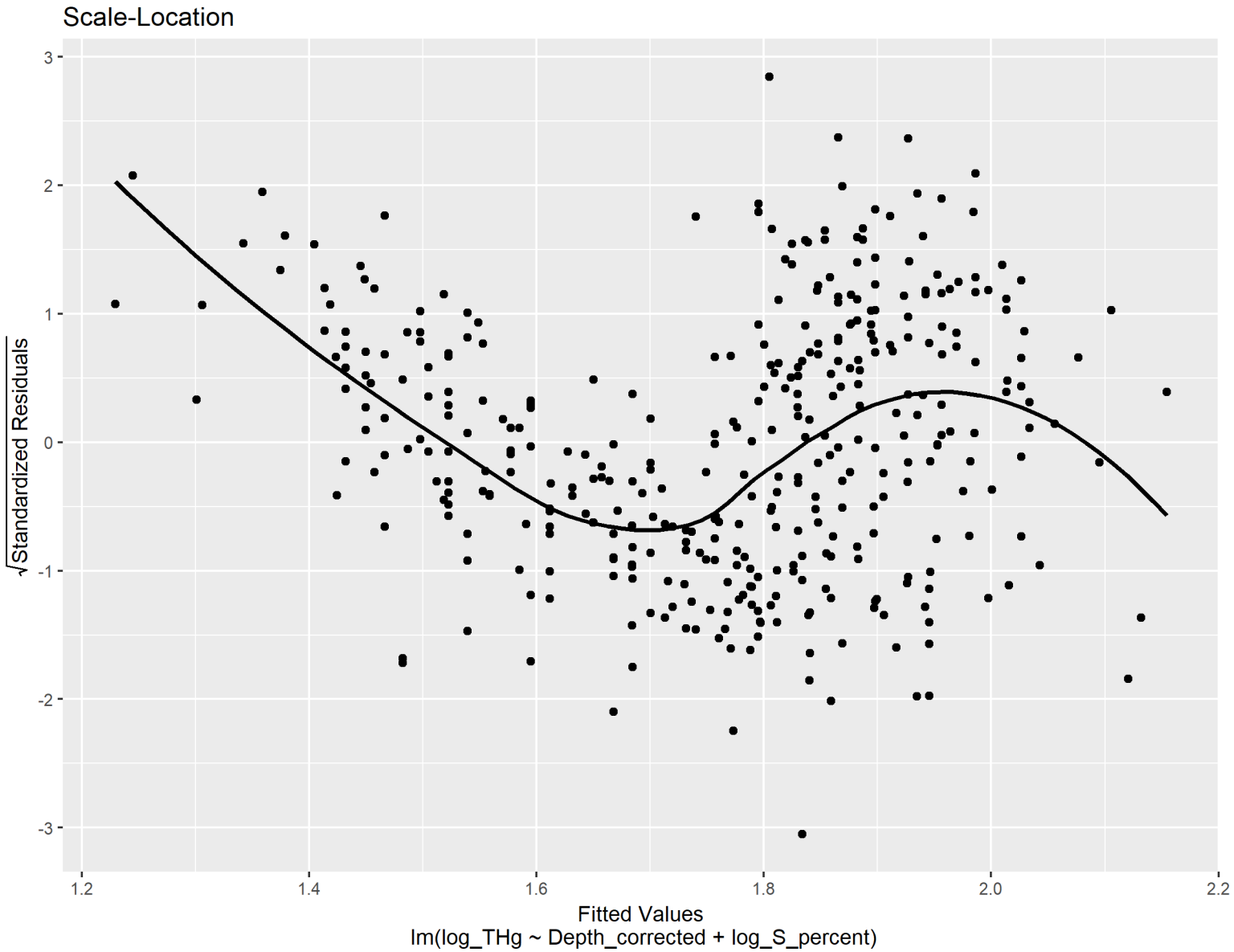

**Figure 19** $Log_{10}$ Transformed Total Mercury (THg) Residuals vs. Leverage Plot

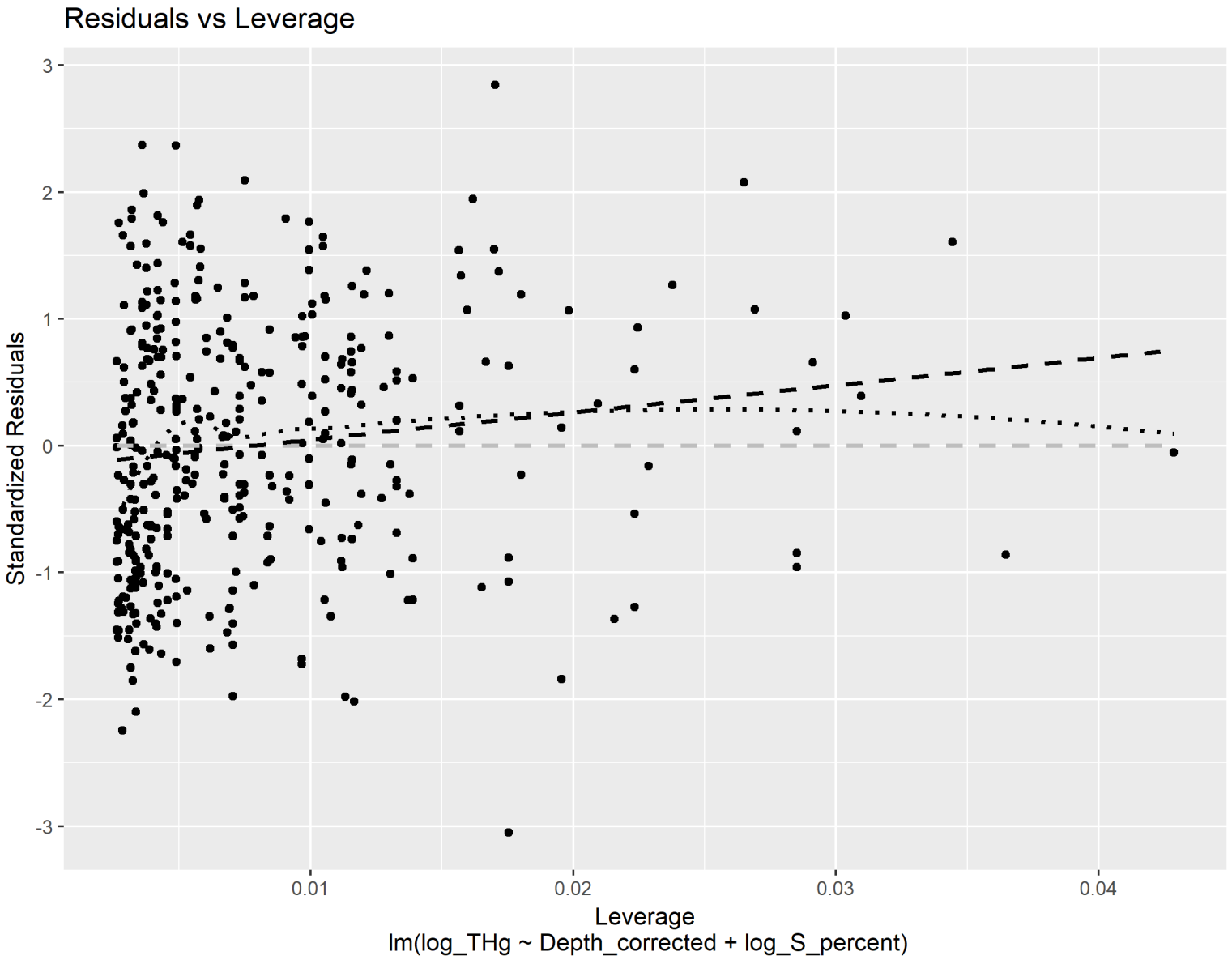

**Figure 20** $Log_{10}$ Transformed Total Mercury (THg) Added Variable Plot for Depth Below Surface

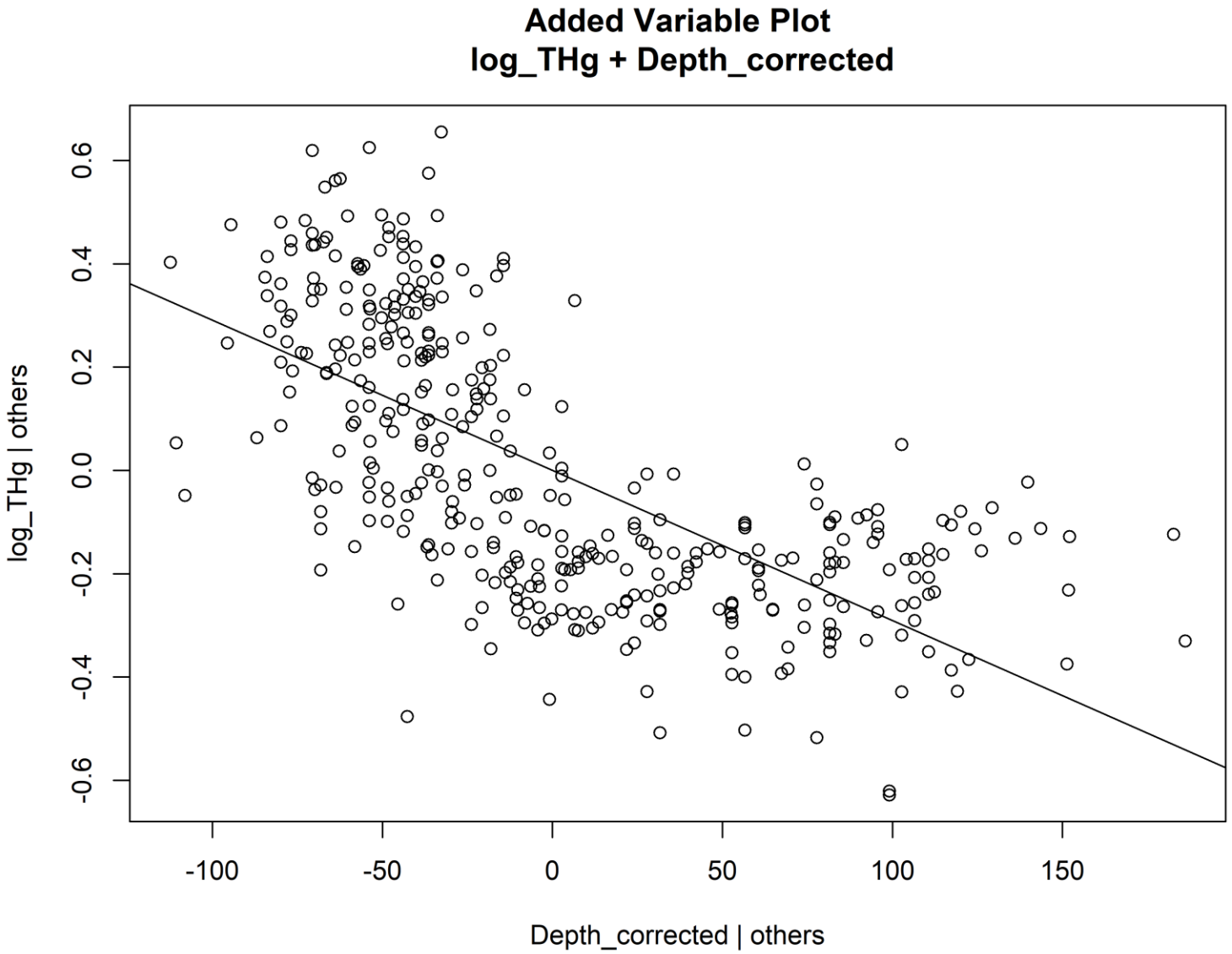

**Figure 21** $Log_{10}$ Transformed Total Mercury (THg) Added Variable Plot for Percent Sulfur (% S)

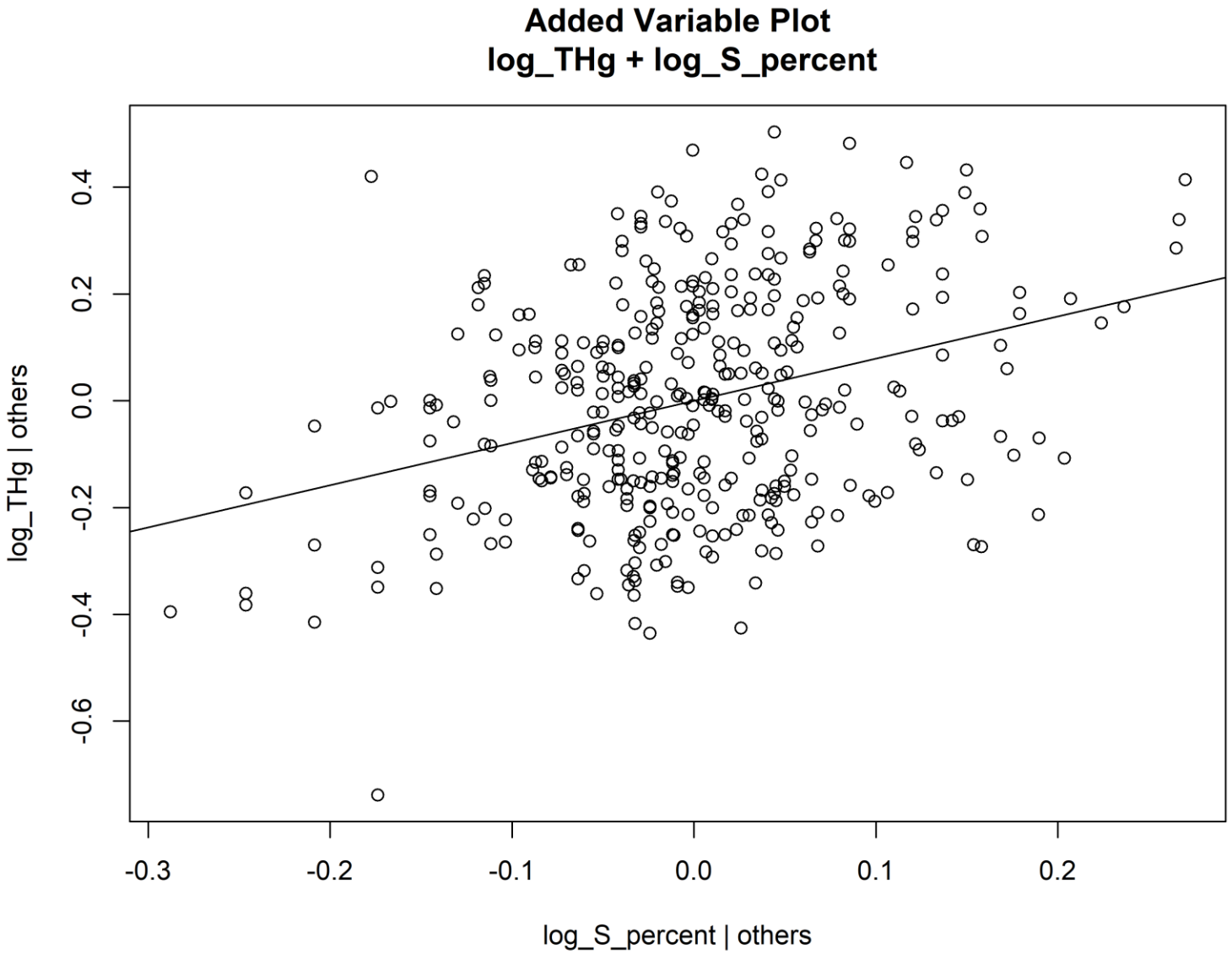

### 3.5 Multiple Linear Regression Analysis of Methylmercury (MeHg) Depth Profiles

Multiple linear regression analysis for the dependent variable log MeHg was conducted for the following independent variables: depth, temperature treatment, $CO_2$ treatment, bulk density, log THg, log %C, log %N, log %S, and log $S_{red}$. Initial choices made in the multiple linear regression for MeHg were based on the same correlation matrix shown in **Figure 13**. Methylmercury values were log normalized based on qualitative analysis of histograms and residual plots, as shown in **Figures 22-27**. Histograms for the MeHg (non-log) and log MeHg were generated and displayed in **Figure 22** and **Figure 23**, respectively. MeHg analysis revealed a normal distributed histogram (**Figure 22**) and log transformation of MeHg gave a normally distributed histogram (**Figure 23**). Log transformation was preferred for analysis of MeHg based on the significant improvement in $R^2$ values observed with log transformation.

The relationship between log MeHg and log THg was found to be most significant ($R^2 = 0.4111$, $p < 0.05$). Linear regression was repeated between log MeHg + log THg and remaining variables (depth, temperature treatment, $CO_2$ treatment, bulk density, log %C, log %N, log %S, and log $S_{red}$). The relationship between log MeHg + log THg and log $S_{red}$ was found to be most significant ($R^2 = 0.4784$, $p < 0.05$). Linear regression was repeated between log MeHg + log THg + log $S_{red}$ and remaining variables (depth, temperature treatment, $CO_2$ treatment, bulk density, log %C, log %N, and log %S). The relationship between log MeHg + log THg + log $S_{red}$ and depth was found to be most significant ($R^2 = 0.5405$, $p < 0.05$). Linear regression was repeated between log MeHg + log THg + log $S_{red}$ + depth and remaining variables (temperature treatment, $CO_2$ treatment, bulk density, log %C, log %N, and log %S). The relationship between log

MeHg + log THg + log $S_{red}$ + depth and log %N was found to be most significant ($R^2$ = 0.5611, $p < 0.05$). Linear regression was repeated between log MeHg + log THg + log $S_{red}$ + depth + log %N and remaining variables (temperature treatment, $CO_2$ treatment, bulk density, log %C, and log %S. No additional significant relationship between log MeHg + log THg + log $S_{red}$ + depth + log %N and any of the remaining variables was found (**AA-91**).

Based on linear regression, therefore, results of MeHg linear regression, displayed in **Table 11**, indicate a predictable relationship between log MeHg, log THg, log $S_{red}$, depth, and log %N according to the following equation:

log MeHg = 0.92*log THg + 3.5*log $S_{red}$ -0.0047*Depth -0.40*log %N (**Equation 4**)

Calculation of AIC and BIC values revealed an improvement in AIC and BIC values with the incorporation of log THg, log $S_{red}$, depth, and log %N, therefore, no variables were removed from the final linear regression equation (**Table 12**). Calculation of VIF values confirmed that independent variables included in the linear regression model were not co-variant (**Table 13**). Please refer to **Figure 35** of the appendix (**AA-91**) for original spreadsheets containing multiple linear regression calculations and values for log MeHg.

**Table 11** $Log_{10}$ Transformed Methylmercury (MeHg) Estimated Values, Standard Error, t Values, and p Values

| | **Linear Regression Summary Statistical Values for log MeHg** | | | |
|---|---|---|---|---|
| **Variable** | **Estimate** | **Standard Error** | **t Value** | **p Value** |
| (Intercept) | -7.8619 | 1.014951 | -7.74608 | 1.59E-12 |
| log THg | 0.915618 | 0.137025 | 6.68213 | 4.88E-10 |
| log $S_{red}$ | 3.54206 | 0.584409 | 6.060929 | 1.14E-08 |
| Depth | -0.00466 | 0.00095 | -4.90041 | 2.56E-06 |
| log % N | -0.3989 | 0.19752 | -2.01955 | 0.045298 |

**Table 12** $Log_{10}$ Transformed Methylmercury (MeHg) $R^2$, Akaike Information Criterion (AIC), and Bayesian Information Criterion (BIC) Values

| **Linear Regression Statistical Values for log MeHg** | |
|---|---|
| **Adjusted $R^2$** | 0.561088 |
| **AIC** | 121.107 |
| **BIC** | 139.0903 |

**Table 13** $Log_{10}$ Transformed Methylmercury (MeHg) Variance Inflation Factor (VIF) Values

| **Log MeHg Variance Inflation Factor (VIF)** | | | | |
|---|---|---|---|---|
| **Variable** | log THg | log $S_{red}$ | Depth | log % N |
| **VIF** | 1.6419 | 2.181876 | 3.178017 | 1.893217 |

Residual plots for the linear regression of log MeHg as a function of log THg, log $S_{red}$, depth, and log %N were generated and displayed in **Figure 24**. The black line displayed is a loess weighted regression. Visual inspection of the log MeHg residual plots where log MeHg is modeled as a function of log THg, log $S_{red}$, depth, and log %N indicate that residual values are evenly dispersed around the horizontal axis (**Figure 24**). Residual normal quantile-quantile (Q-Q) plots for the linear regression of log MeHg as a function of log THg, log $S_{red}$, depth, and log %N were generated and displayed in **Figure 25**. Visual inspection of the log MeHg residual normal Q-Q plot where log MeHg is modeled as a function of log THg, log $S_{red}$, depth, and log %N indicates that the residuals

are normally distributed between the theoretical quantile (TQ) range of -2 and 2, with some variability observed in the outermost regions (TQ < -2 or > 2) (**Figure 25**).

Scale-location plots for the linear regression of log MeHg as a function of log THg, log $S_{red}$, depth, and log %N were generated and displayed in **Figure 26**. Visual inspection of **Figure 26** indicates that residuals are spread equally along the range of fitted values, therefore, fulfilling the assumption of equal variance i.e. residuals are homoscedastic. Residual vs. leverage plots for the linear regression of log MeHg as a function of log THg, log $S_{red}$, depth, and log %N were generated and displayed in **Figure 27**. The black dotted line displayed the loess weighted regression and the black dashed line indicates a linear regression. Visual inspection of **Figure 27** indicates normal distribution about the horizontal axis. Added variable plots for the linear regression of log MeHg as a function of log THg, log $S_{red}$, depth, and log %N were generated separately and are displayed in **Figure 28**, **Figure 29**, **Figure 30**, and **Figure 31**. Visual inspection of **Figure 28-31** confirms a non-zero slope for all added variables, demonstrating that the addition of log THg, log $S_{red}$, depth, and log %N have significant effects on the linear regression model overall.

**Figure 22** Untransformed Methylmercury (MeHg) Histogram Plot

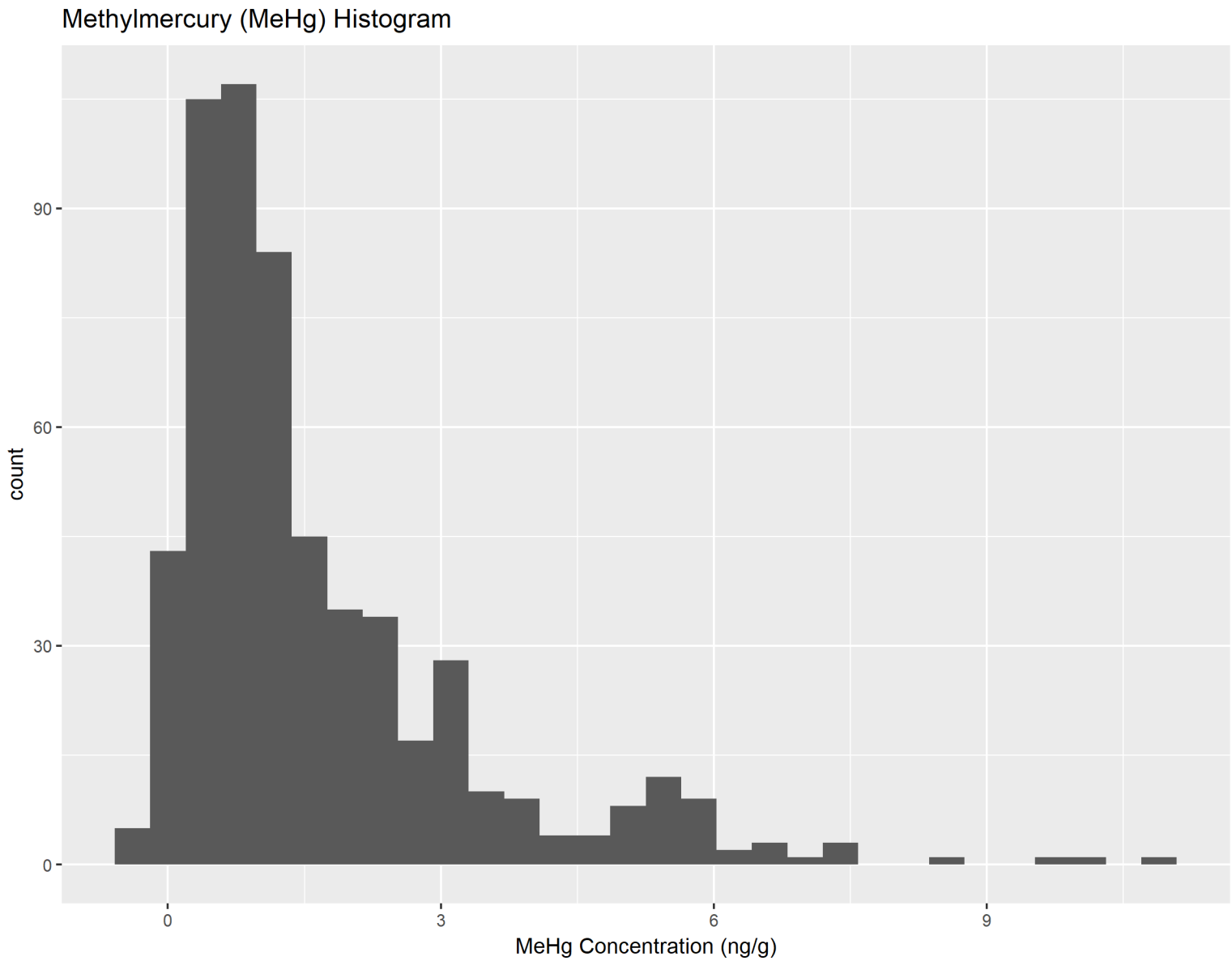

**Figure 23** $Log_{10}$ Transformed Methylmercury (MeHg) Histogram Plot

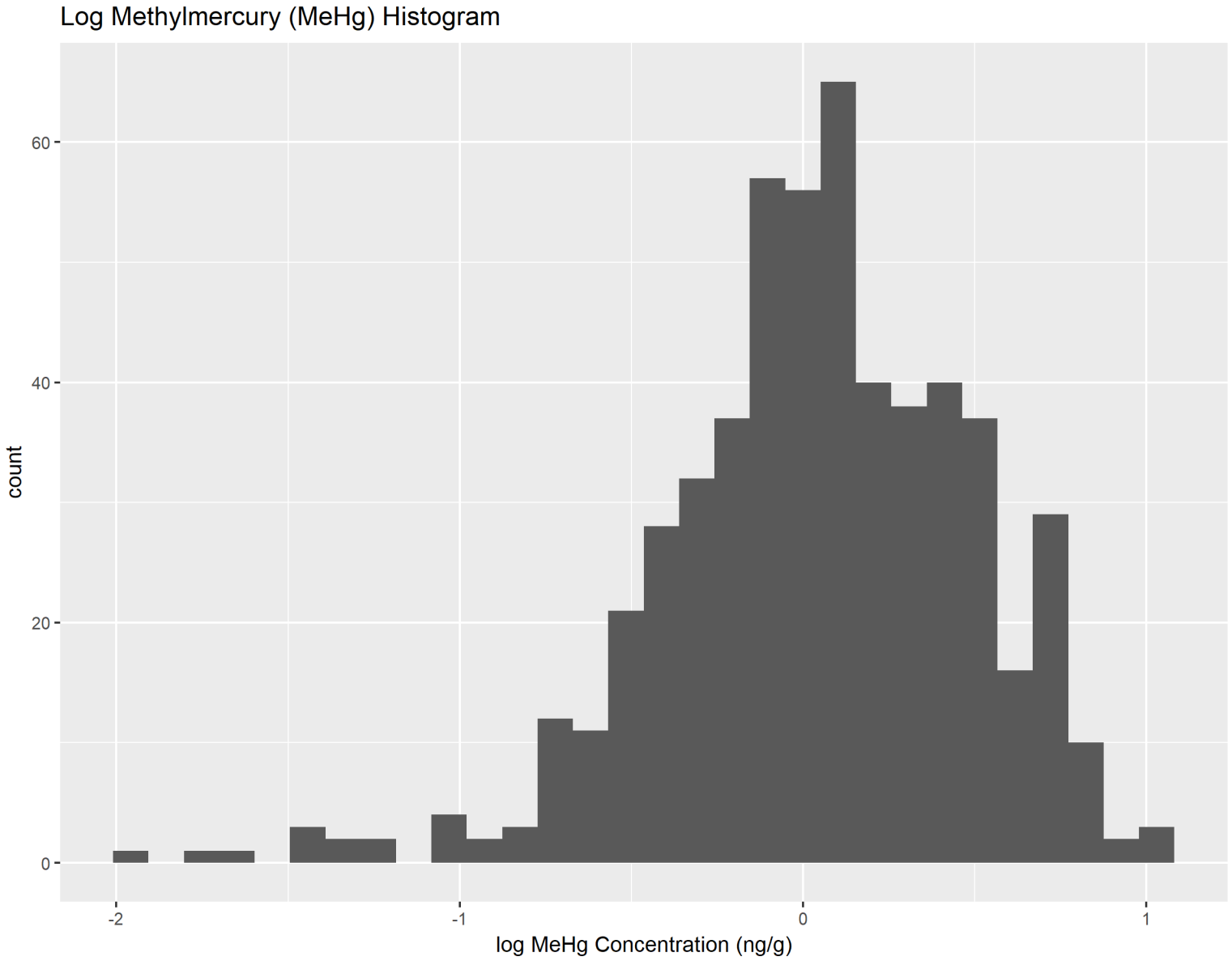

**Figure 24** $Log_{10}$ Transformed Methylmercury (MeHg) Residuals vs. Fitted Values Plot

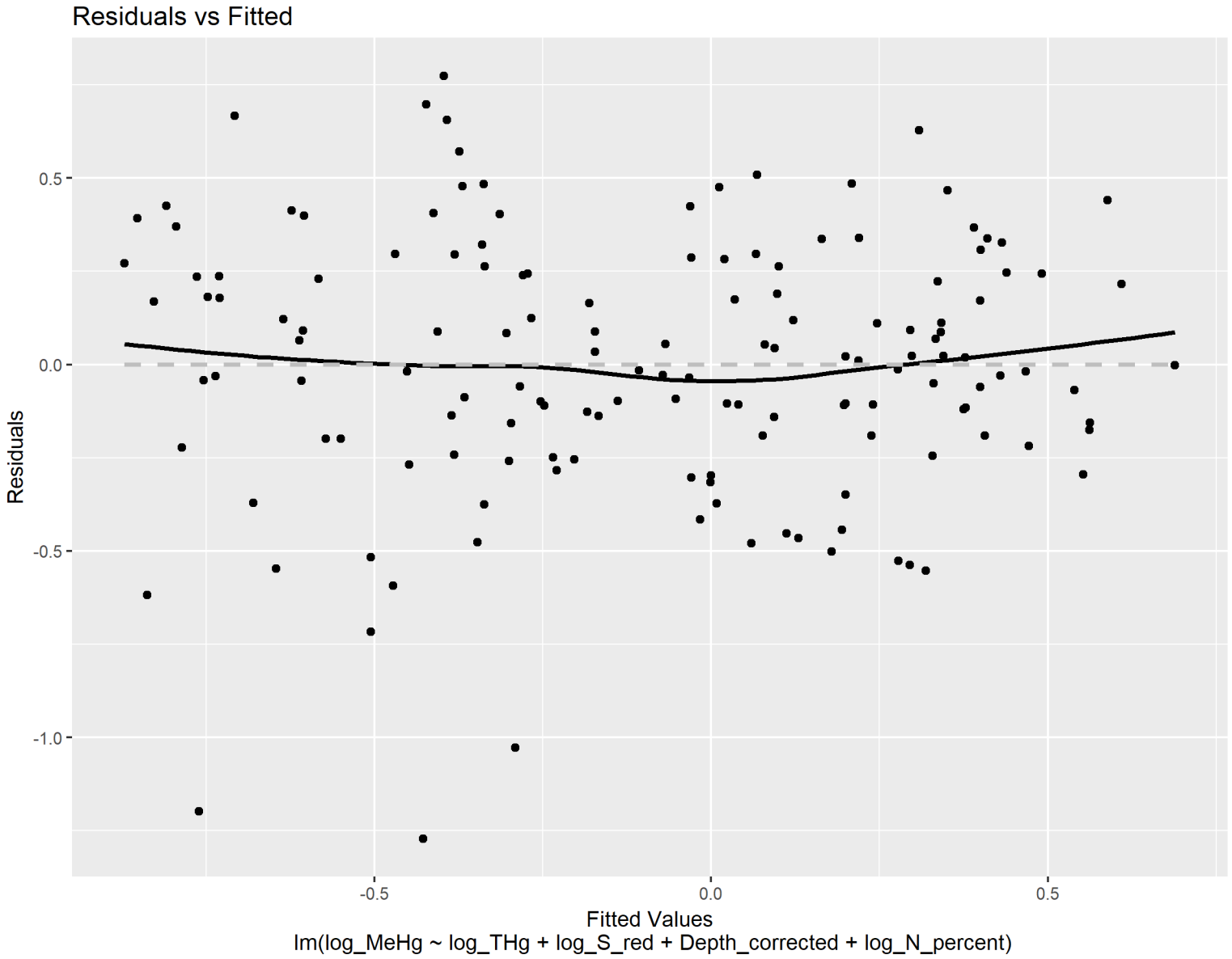

**Figure 25** $Log_{10}$ Transformed Methylmercury (MeHg) Q-Q Plot

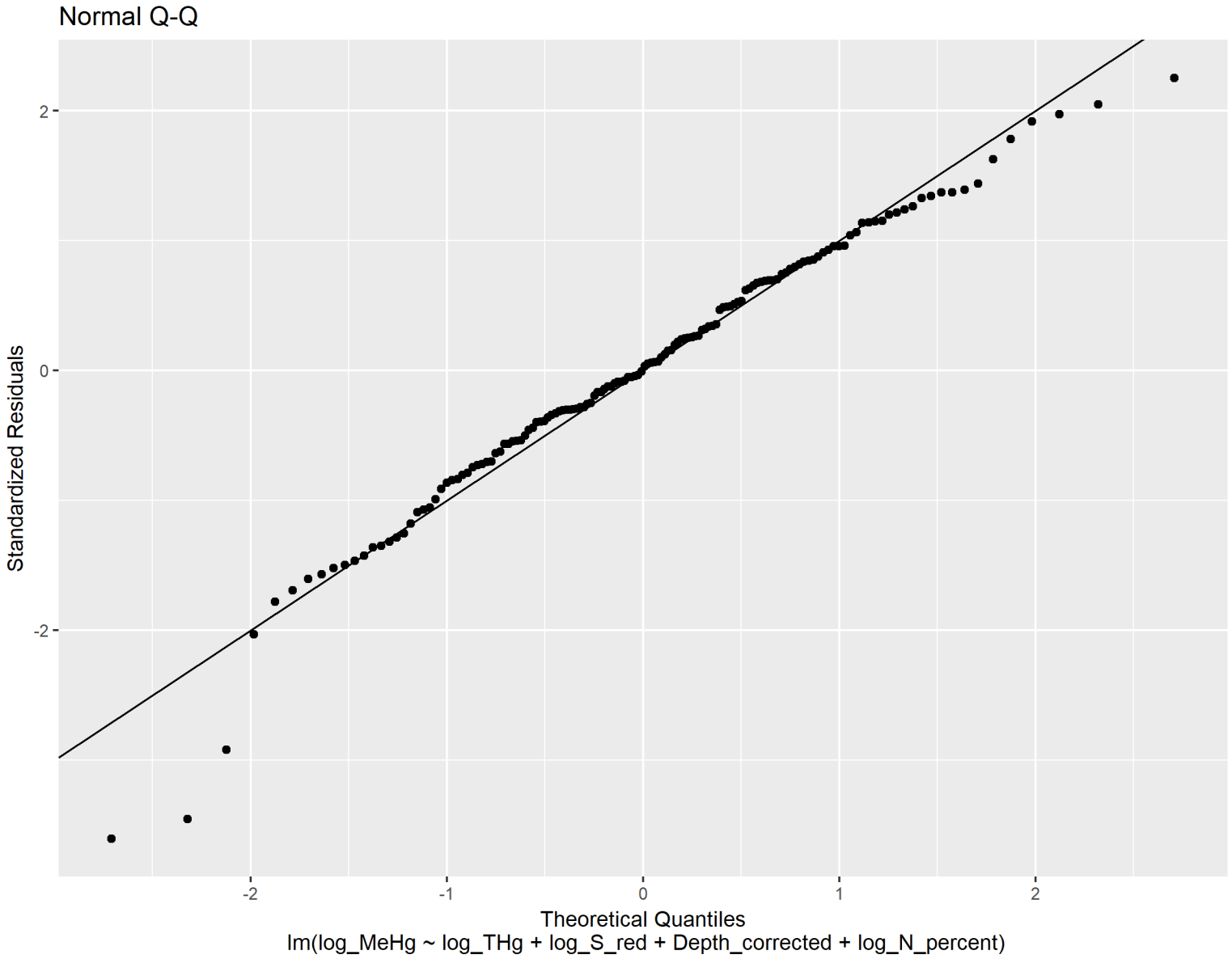

**Figure 26** $Log_{10}$ Transformed Methylmercury (MeHg) Scale-Location Plot

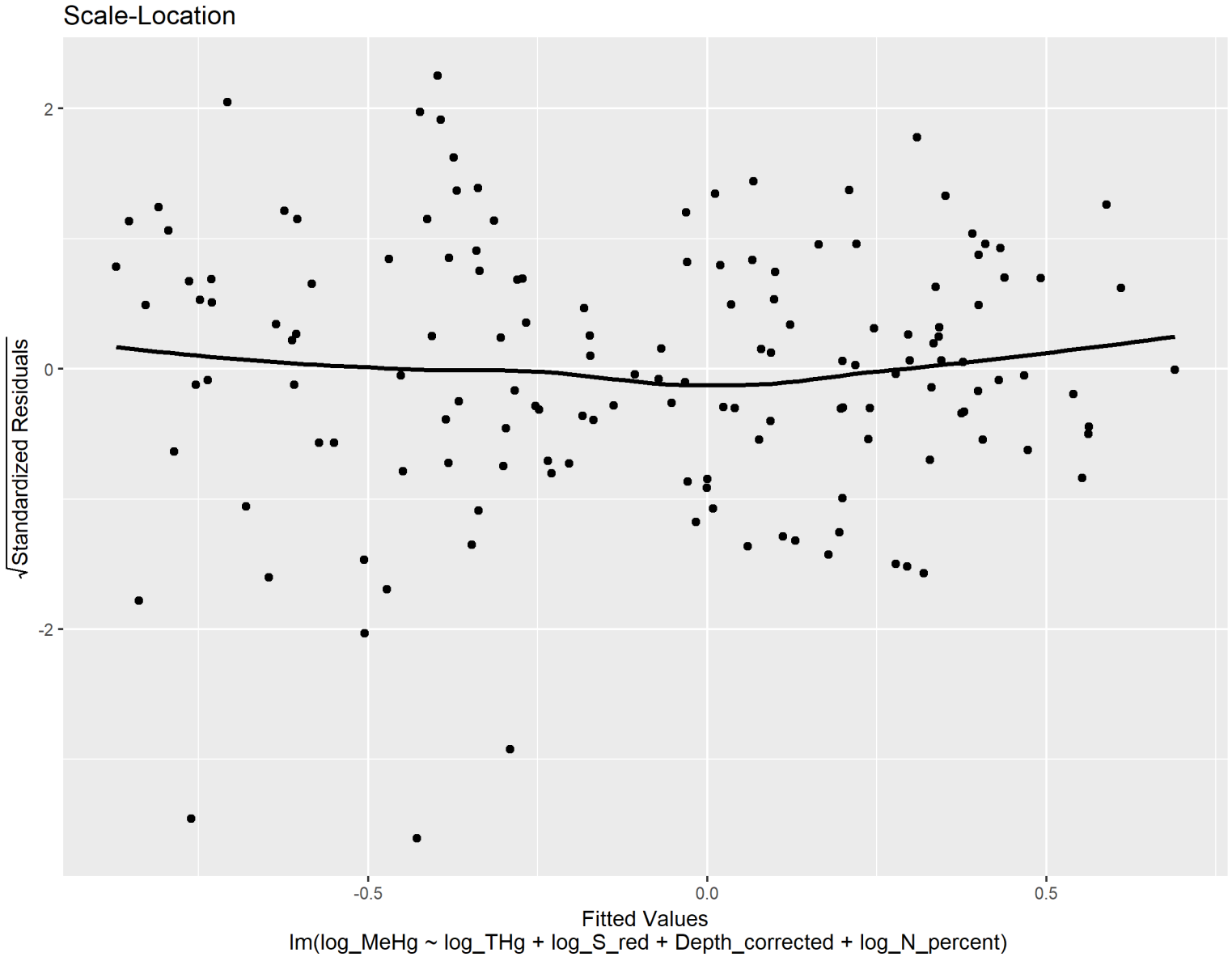

**Figure 27** $Log_{10}$ Transformed Methylmercury (MeHg) Residuals vs. Leverage Plot

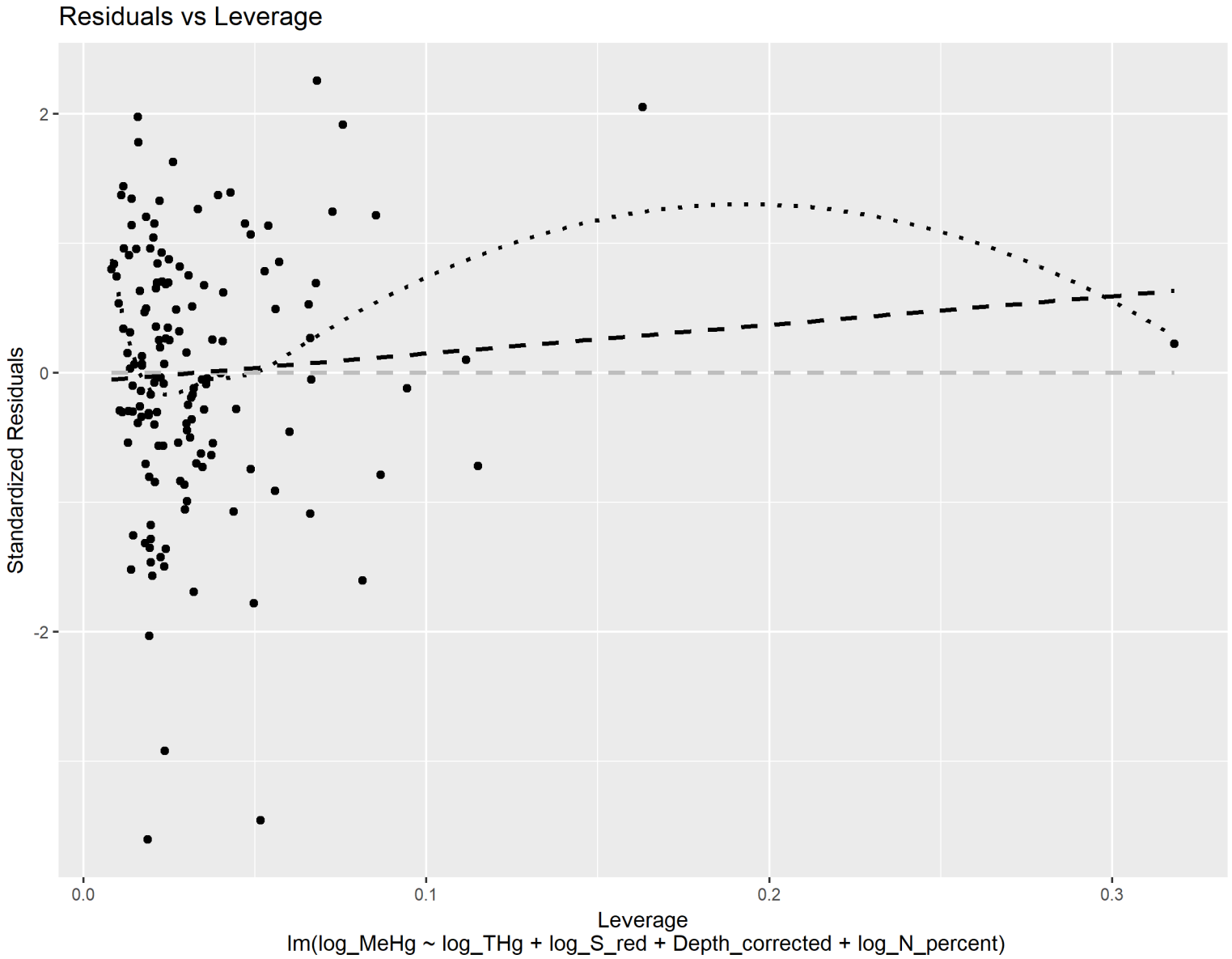

**Figure 28** $Log_{10}$ Transformed Methylmercury (MeHg) Added Variable Plot for $log_{10}$ Transformed Total Mercury (THg)

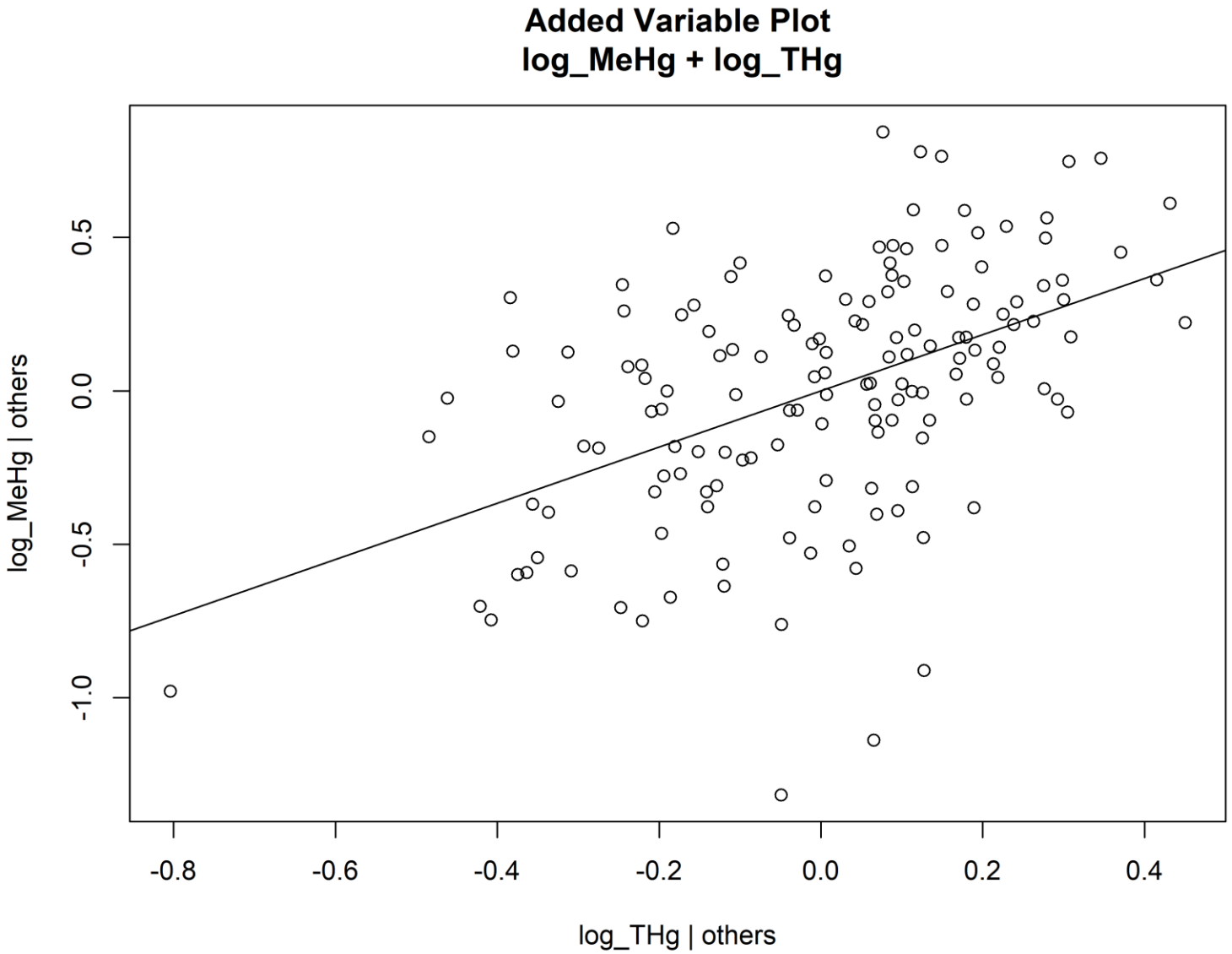

**Figure 29** $Log_{10}$ Transformed Methylmercury (MeHg) Added Variable Plot for $log_{10}$ Transformed Reduced Sulfur ($S_{red}$)

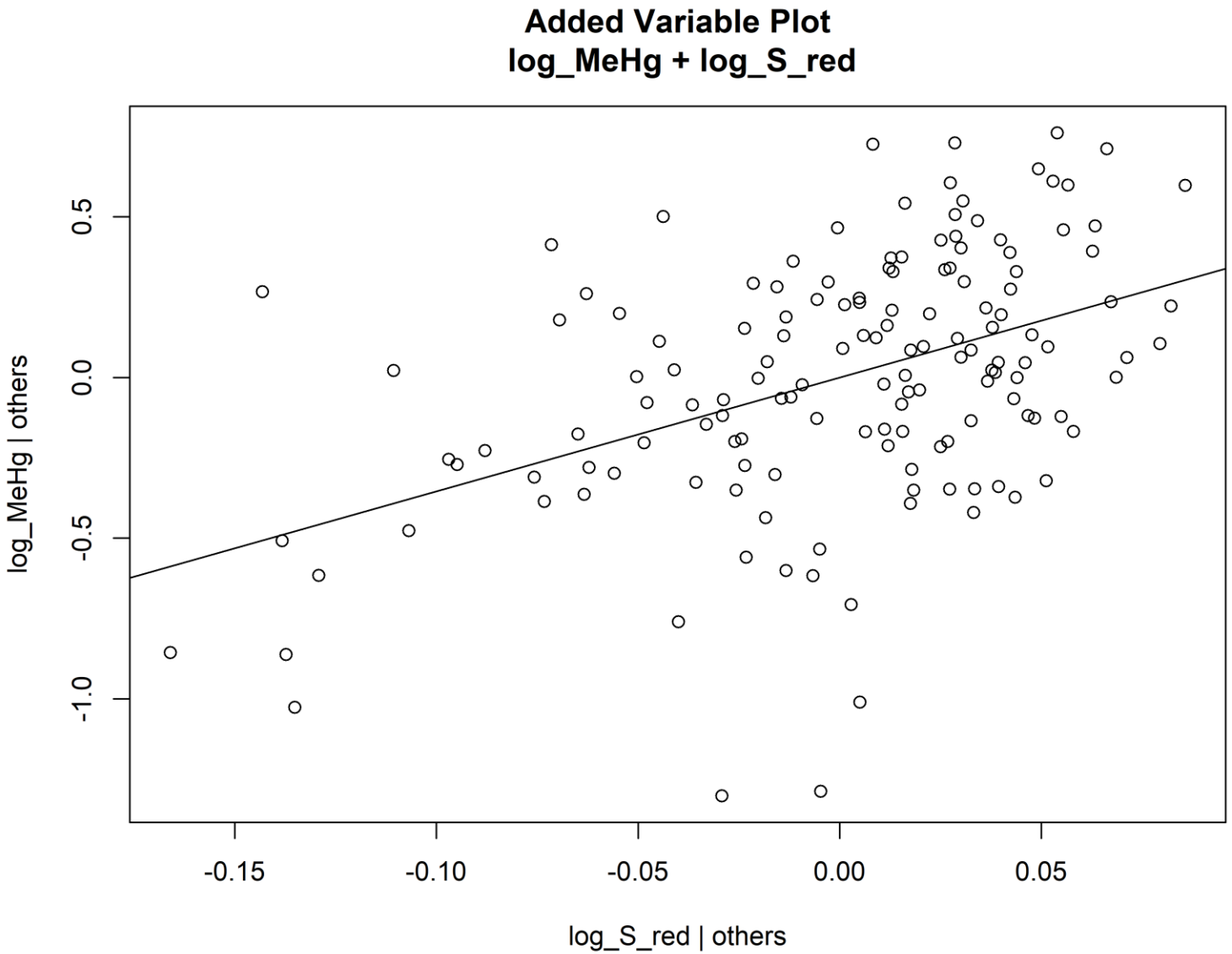

**Figure 30** $Log_{10}$ Transformed Methylmercury (MeHg) Added Variable Plot for Depth Below Peat Surface

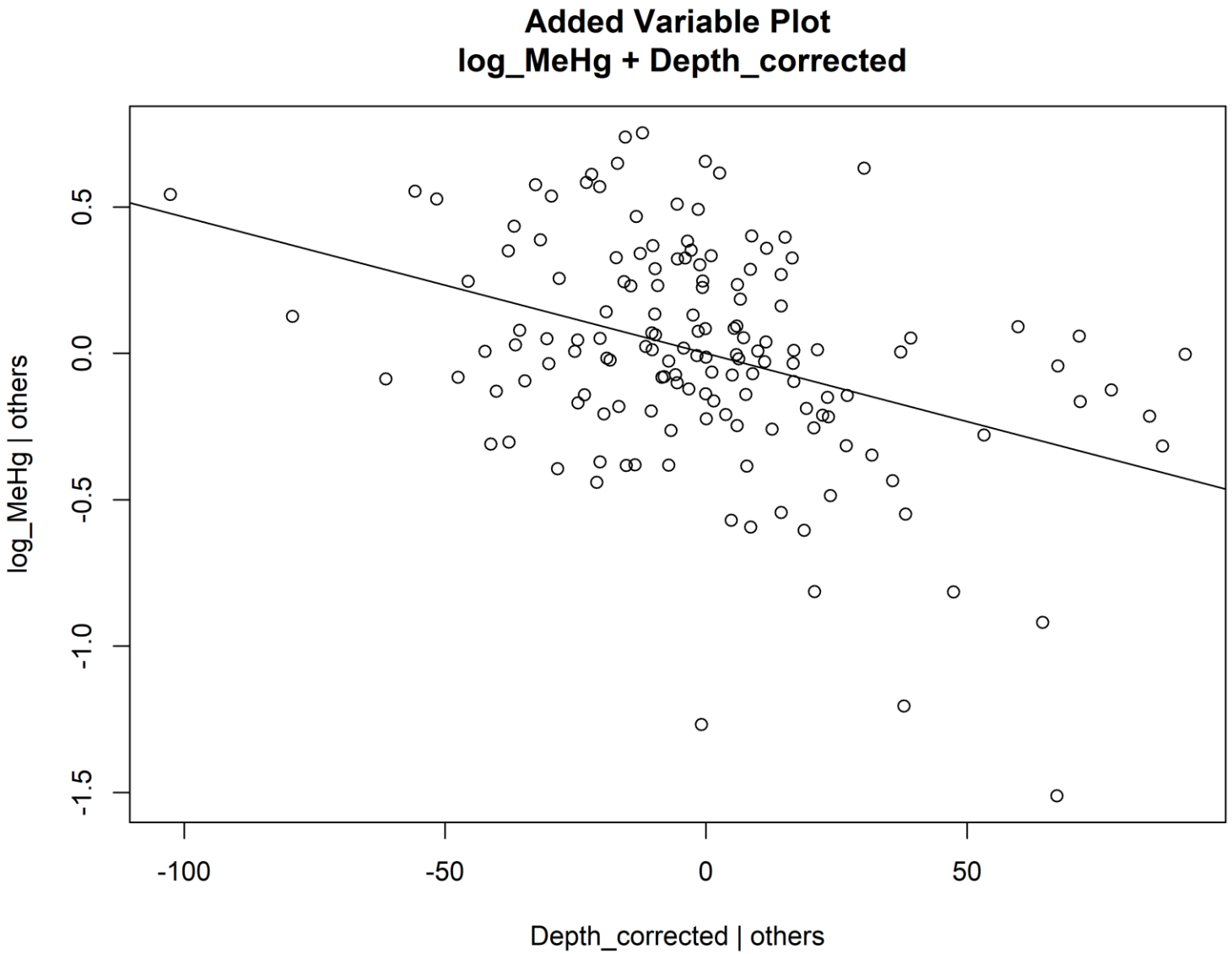

**Figure 31** $Log_{10}$ Transformed Methylmercury (MeHg) Added Variable Plot for Percent Nitrogen (% N)

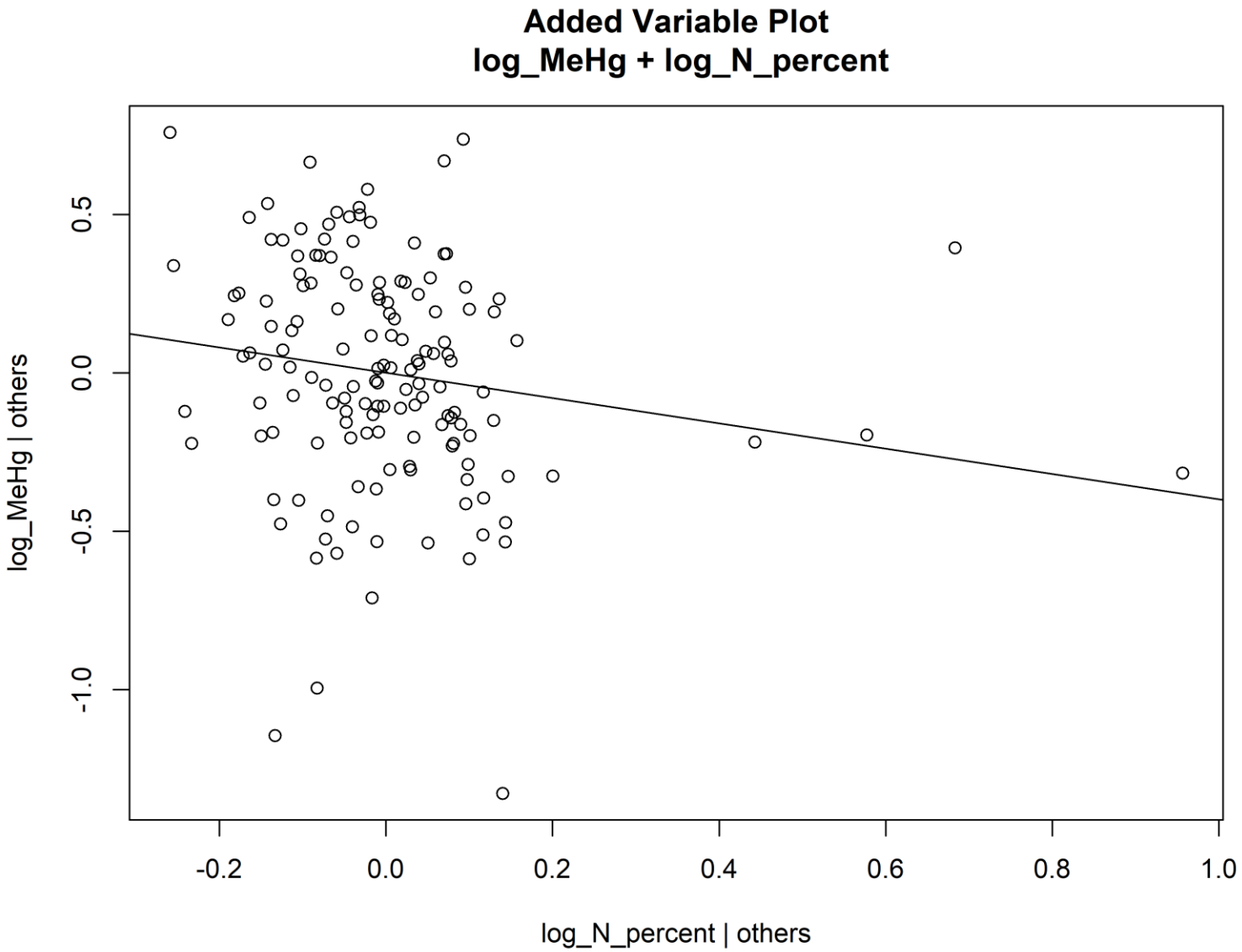

# CHAPTER 4

# Discussion

With future predicted increases in global temperature and atmospheric $CO_2$ concentrations[38], the impact on the cycling of Hg and S in the natural environment is uncertain. Current climate predictions estimate significant future increases in global average temperatures coupled with elevated levels of atmospheric $CO_2$[38]. Researchers have shown that increases in average temperature resulted in increased production of MeHg in the soil[22, 44, 45]. Previous studies have also indicated that increased levels of atmospheric $CO_2$ can also increase MeHg production[22,45, 47]. Moreover, elevated levels of $CO_2$ are predicted to cause increased rates of microbial decomposition in the soil[80], potentially increasing the net microbial demethylation of methylmercury. Overall, increased production of MeHg in peatlands could lead to increased amounts of MeHg released to streams[81], resulting in enhanced bioavailability to aquatic organisms and further bioaccumulation up the food chain.

## 4.1 Effects of Temperature and $CO_2$ Treatments on 2016 THg, MeHg, and $S_{red}$ Depth Profiles

The depth at which concentration maxima occur for THg, MeHg, and $S_{red}$ in peat solids, as well as the magnitude of those maxima is one potential way of comparing depth profiles to look at responses to the temperature and $CO_2$ treatments. In this study, no net response in the THg, MeHg, or $S_{red}$ depth concentration profiles was seen with heat treatment or $CO_2$ elevation. In this analysis of concentration depth profiles, only one full

year of experimental treatments were applied. Therefore, it is possible that these trends may change over the course of the ongoing 10-year experiment. Furthermore, it is possilbe that the chemistry of the peat solids will change more slowly than porewaters. While the chemistry of the porewaters is beyond the scope of this thesis, porewater concentrations of THg, MeHg, and $S_{red}$ are being measured for the SPRUCE experiment.

The relationship between temperature treatment and the depth at which $THg_{max}$ and $MeHg_{max}$, occur were investigated using linear regression and no statistically significant relationship was found for any of the variables analyzed. Therefore, at this point, it is unclear whether the temperature treatment will impact the depth at which $THg_{max}$ and $MeHg_{max}$ occur. Again, it is possible that the effect of temperature treatment will take longer than 1 year to become apparent, however, further research is needed to determine whether that effect would be significant. Although the releationship between $THg_{max}$, $MeHg_{max}$ and temperature treatment is not significant, based on visual inspection of depth profiles and calculation and comparison of max values, there is a trend towards maximum values occuring at lower depths which does seem apparent. Since this evaluation was qualitative, more detailed analysis would be necessary to determine if, in fact, any significant trends do exist.

While increased MeHg production has been reported for soils with elevated temperature treatments[22,44,45], no increase in MeHg production was observed with heat treatment in the SPRUCE experiment. One possible explanation is that increasing temperature and elevation of $CO_2$ may drive the water table further down in depth in the peat due to increased rates of evapotranspiration[82]. This could result in a deepening of the oxic layer, or, alternatively, a longer period of oxidation at depths which normally exist

in a reducing environment. As a result of this oxic layer occuring deeper in the peat, it's possible that the lowered water table would prevent increased MeHg production, thereby, mediating any possible increase. Increased MeHg production in soil has also been reported for sites with elevated atmospheric $CO_2$[22,45, 47]. However, in the present study, no increase in MeHg production was observed with $CO_2$ elevation.

### 4.2 Linear Regression Equations for Total Mercury (THg)

Statistical models were generated using a multiple linear regression approach to describe the behavior of THg and MeHg based on various biogeochemically related variables (depth, $S_{red}$, %C, %N, %S). Following linear regression, a significant relationship was established between THg and both the depth below the peat surface and $\log_{10}$ transformed %S in the peat solids according to **Equation 3**.

As a result of changing atmospheric deposition of Hg and S over time[83,84], THg is expected to be a function of both depth and %S. Although %S has no formal relationship with the appearance of THg, because both species are atmospherically deposited in ombrotrophic peat bogs[85,86] and because, furthermore, both are products of industrial combustion[78, 87], the two are likely to have a co-variant relationship. Furthermore, the relationship between THg and depth was negative, reflecting higher THg near the surface, again, potentially due to increases in atmospheric deposition since the industrial revolution, although, since the 1970's, atmospheric deposition of Hg has declined in the Upper Midwest region[79].

### 4.3 Linear Regression Equations for Methylmercury (MeHg)

Following multiple linear regression, a significant relationship was established between the $\log_{10}$ transformed MeHg concentration in peat solids and the $\log_{10}$ transformed concentrations of THg, $S_{red}$, and %N, as well as the depth below the peat surface according to **Equation 4**.

The relationship between THg and MeHg is easily explained by basic chemistry. According to **Equation 1**, MeHg is a function of THg, thus, the relationship between THg and MeHg is obvious, since THg is actually required in order for the chemical formation of MeHg to occur.

The general relationship between sulfur (S) and MeHg in soil is well established[19], with the reduction of sulfate ($SO_4^{2-}$) to sulfide ($S^{2-}$) by sulfate-reducing bacteria thought to be driving the production of MeHg. In this case, linear regression indicated a statistically significant positive relationship between the dependent variable, MeHg, and the independent variable, $S_{red}$. MeHg is highly related to $S_{red}$, since the reduction of $SO_4^{2-}$ and the methylation of Hg to MeHg both occur in the same redox zone existing around the water table. Additionally, this indicates that $S_{red}$ is a reasonable proxy for the local redox environment within peatland soils.

The relationship between MeHg and depth was negative and the same relationship was found between THg and depth, which is in agreement with the known relationship between depth and redox. The observed decrease in net MeHg with depth is related to the lack of active MeHg reduction in the catotelm and continuing demethylation.

In addition, MeHg was found to be negatively correlated with %N. With high nitrogen (N) concentrations in the form of ammonium ($NH_3^+$), very little reduction of N occurs, thus, it's possible that the redox potential does not decrease enough to reduce $SO_4^-$, thereby limiting formation of MeHg. In this context, %N would be a limiting factor for the production of MeHg. It's also possible that the relationship between MeHg and %N is inverse co-variance with depth or potentially spurious. At this point, the cause for this relationship remains unclear.

# CHAPTER 5

## Conclusions

The biogeochemical cycling of Hg and S are complex environmental processes found occurring in peatland soils. In this experiment, simulated warming and $CO_2$ - elevation were utilized to determine the potential impacts, if any, of rising global temperatures and atmospheric $CO_2$ concentrations on the chemical speciation of selected species (THg, MeHg, and $S_{red}$). In this study, no significant trends in THg, MeHg or $S_{red}$ were observed with temperature or $CO_2$ treatment. Continuation of this research in the future may show significant relationships between THg, MeHg, and $S_{red}$ with increased temperature and elevated atmospheric $CO_2$. This study contains the largest existing dataset of XANES values in peatlands. In addition, the determination of $S_{red}$ in peatland soils is unique to this study. Finally, the relationship between $S_{red}$ and MeHg demonstrated here illustrates the value of $S_{red}$ as a predictor for MeHg and a proxy for the redox environment.

BIBLIOGRAPHY


1. Tchounwou, P. B., Yedjou, C. G., Patlolla, A. K. & Sutton, D. J. Heavy Metals Toxicity and the Environment. *NIH Public Access* 365–396 (2014). doi:10.1007/978-3-7643-8338-1

2. Järup, L. Hazards of heavy metal contamination. *Br. Med. Bull.* **68,** 167–182 (2003).

3. Kabir, E. *et al.* Current status of trace metal pollution in soils affected by industrial activities. *ScientificWorldJournal.* **2012,** 916705 (2012).

4. Chen, C. *et al.* Methylmercury in marine ecosystems: Spatial patterns and processes of production, bioaccumulation, and biomagnification. *Ecohealth* **5,** 399–408 (2008).

5. Hong, Y., Kim, Y. & Lee, K. Methylmercury Exposure and Health Effects. 353–363 (2012).

6. Center for Food Safety and Applied Nutrition. Metals - Fish: What Pregnant Women and Parents Should Know. *Directly accessed from FDA website* 20852 (2014).

7. Minnesota Department of Health. Information for Healthcare Professionals about Prenatal Mercury Exposure Guidelines for pregnant women , women planning pregnancy and children under age 15. (2011).

8. Bindler, R., Yu, R., Hansson, S., Claßen, N. & Karlsson, J. Mining, metallurgy and the historical origin of mercury pollution in lakes and watercourses in Central Sweden. *Environ. Sci. Technol.* **46,** 7984–7991 (2012).

9. Nriagu, J. O. A History of Global Metal Pollution. *Science (80-. ).* **272,** 223–224 (2017).

10. Martínez Cortizas, A., López-Merino, L., Bindler, R., Mighall, T. & Kylander, M. E. Early atmospheric metal pollution provides evidence for Chalcolithic/Bronze Age mining and metallurgy in Southwestern Europe. *Sci. Total Environ.* **545–546,**

398–406 (2016).

11. Boutton, C. F. Post-Industrial Revolution changes in large-scale atmospheric pollution of the northern hemisphere by heavy metals in a pioneering paper twenty five years ago evidenced for the furst time that the Arctic atmosphere was [ Murozumi Using revolutionary ultra. **100,** (1995).

12. Selin, N. E. Global Biogeochemical Cycling of Mercury: A Review. *Annu. Rev. Environ. Resour.* **34,** 43–63 (2009).

13. Pacyna, E. G., Pacyna, J. M., Steenhuisen, F. & Wilson, S. Global anthropogenic mercury emission inventory for 2000. *Atmos. Environ.* **40,** 4048–4063 (2006).

14. Futsaeter, G. & Wilson, S. The UNEP Global Mercury Assessment: Sources , Emissions and Transport. *E3S Web Conf.* **36001,** 2–3 (2013).

15. Boening, D. W. Ecological effects, transport, and fate of mercury: A general review. *Chemosphere* **40,** 1335–1351 (2000).

16. Higueras, P. *et al.* Industrial and natural sources of gaseous elemental mercury in the Almadén district (Spain): An updated report on this issue after the ceasing of mining and metallurgical activities in 2003 and major land reclamation works. *Environ. Res.* **125,** 197–208 (2013).

17. Grigal, D. F. Inputs and outputs of mercury from terrestrial watersheds: a review. *Environ. Rev.* **10,** 1–39 (2002).

18. Åkerblom, S. *et al.* Significant interaction effects from sulfate deposition and climate on sulfur concentrations constitute major controls on methylmercury production in peatlands. *Geochim. Cosmochim. Acta* **102,** 1–11 (2013).

19. Coleman Wasik, J. K. *et al.* Methylmercury declines in a boreal peatland when experimental sulfate deposition decreases. *Environ. Sci. Technol.* **46,** 6663–6671 (2012).

20. Enrico, M. *et al.* Atmospheric Mercury Transfer to Peat Bogs Dominated by Gaseous Elemental Mercury Dry Deposition. *Environ. Sci. Technol.* **50,** 2405–

2412 (2016).

21. Kolka, R. K., Nater, E. A, Grigal, D. F, Verry, E. S. Atmospheric Inputs of Mercury and Organic Carbon into a Forested Upland/Bog Watershed. *Water, Air Soil Pollut.* 273–294 (1999).

22. Yang, Z. *et al.* Warming increases methylmercury production in an Arctic soil. *Environ. Pollut.* **214,** 504–509 (2016).

23. Echols, K. R., Meadows, J. C. & Orazio, C. E. Pollution of Aquatic Ecosystems II: Hydrocarbons, Synthetic Organics, Radionuclides, Heavy Metals, Acids, and Thermal Pollution. *Encycl. Inl. Waters* 120–128 (2009). doi:10.1016/B978-012370626-3.00223-4

24. Shao, D., Kang, Y., Wu, S. & Wong, M. H. Effects of sulfate reducing bacteria and sulfate concentrations on mercury methylation in freshwater sediments. *Sci. Total Environ.* **424,** 331–336 (2012).

25. Yu, R. Q. *et al.* Contribution of coexisting sulfate and iron reducing bacteria to methylmercury production in freshwater river sediments. *Environ. Sci. Technol.* **46,** 2684–2691 (2012).

26. Gilmour, C. C. *et al.* Mercury methylation by novel microorganisms from new environments. *Environ. Sci. Technol.* **47,** 11810–11820 (2013).

27. Compeau, G. C. & Bartha, R. Sulfate-Reducing Bacteria: Principle Methylators of Mercury in Anoxic Estuarine Sediment. *Appl. Environ. Microbiol.* **50,** 498–502 (1985).

28. Revis, N. W., Osborne, T. R., Holdsworth, G. & Hadden, C. Distribution of Mercury Species in Soil from a Mercury-Contaminated Site. *Water, Air Soil Pollut.* **45,** 105–113 (1989).

29. Manceau, A. *et al.* Formation of Mercury Sulfide from Hg(II) − Thiolate Complexes in Natural Organic Matter. *Environ. Sci. Technol.* (2015). doi:10.1021/acs.est.5b02522

30. Dwayne, E. (Oak R. N. L. *Personal Communication*.

31. Rui, J. *et al.* Responses of bacterial communities to simulated climate changes in alpine meadow soil of the Qinghai-Tibet plateau. *Appl. Environ. Microbiol.* **81,** 6070–6077 (2015).

32. Zhang, H. & Lindberg, S. E. Processes influencing the emission of mercury from soils: A conceptual model. *J. Geophys. Res.* **104,** 21889 (1999).

33. Xia, K. *et al.* X-ray absorption spectroscopic evidence for the complexation of HG(II) by reduced sulfur in soil humic substances. *Environ. Sci. Technol.* **33,** 257–261 (1999).

34. Manceau, A. & Nagy, K. L. Relationships between Hg(II)-S bond distance and Hg(II) coordination in thiolates. *Dalt. Trans. (Cambridge, England)* **11,** 1421–1425 (2008).

35. Skyllberg, U., Bloom, P. R., Qian, J., Lin, C. M. & Bleam, W. F. Complexation of mercury(II) in soil organic matter: EXAFS evidence for linear two-coordination with reduced sulfur groups. *Environ. Sci. Technol.* **40,** 4174–4180 (2006).

36. Miller, C. L. *et al.* Characterization of soils from an industrial complex contaminated with elemental mercury. *Environmental Research* **125,** 20–29 (2013).

37. Graham, A. M., Aiken, G. R. & Gilmour, C. C. Dissolved organic matter enhances microbial mercury methylation under sulfidic conditions. *Environ. Sci. Technol.* **46,** 2715–2723 (2012).

38. IPCC. Climate Change 2014 Synthesis Report. *Contrib. Work. Groups I, II III to Fifth Assess. Rep. Intergov. Panel Clim. Chang.* 1–112 (2014).

39. Assessment, N. C. Midwest Regional Climate Estimates. (2017). Available at: https://nca2014.globalchange.gov/report/regions/midwest.

40. Carrie, J. *et al.* Increasing contaminant burdens in an arctic fish, burbot (Lota lota), in a warming climate. *Environ. Sci. Technol.* **44,** 316–322 (2010).

41. Dijkstra, J. A. *et al.* Experimental and Natural Warming Elevates Mercury Concentrations in Estuarine Fish. *PLoS One* **8,** 1–9 (2013).

42. Drigo, B. *et al.* Shifting carbon flow from roots into associated microbial communities in response to elevated atmospheric CO 2. *Pnas* **107,** 10938–10942 (2010).

43. Fang, H., Cheng, S. & Lin, E. Elevated atmospheric carbon dioxide concentration stimulates soil microbial activity and impacts water-extractable organic carbon in an agricultural soil. 253–267 (2015). doi:10.1007/s10533-014-0039-2

44. Rydberg, J., Klaminder, J., Rosén, P. & Bindler, R. Climate driven release of carbon and mercury from permafrost mires increases mercury loading to sub-arctic lakes. *Sci. Total Environ.* **408,** 4778–4783 (2010).

45. St. Pierre, K. a, Chételat, J., Yumvihoze, E. & Poulain, A. J. Temperature and the sulphur cycle control monomethylmercury cycling in high Arctic coastal marine sediments from Allen Bay, Nunavut, Canada. *Environ. Sci. Technol.* **48,** 2680–2687 (2014).

46. Jastrow, J. D. *et al.* Elevated atmospheric carbon dioxide increases soil carbon. *Glob. Chang. Biol.* **11,** 2057–2064 (2005).

47. Natali, S. M. *et al.* Increased mercury in forest soils under elevated carbon dioxide. *Oecologia* **158,** 343–354 (2008).

48. Oh, N. H. & Richter, D. D. Soil acidification induced by elevated atmospheric CO2. *Glob. Chang. Biol.* **10,** 1936–1946 (2004).

49. Matilainen, T., Verta, M., Korhonen, H., Uusi-Rauva, A. & Niemi, M. Behavior of mercury in soil profiles: Impact of increased precipitation, acidity, and fertilization on mercury methylation. *Water. Air. Soil Pollut.* **125,** 105–119 (2001).

50. Lodenius, M. & Autio, S. Effects of Acidification on the Mobilization of Cadmium and Mercury from Soils. **267,** 261–267 (1989).

51. Furman, O. S. *et al.* Co-cycling of sulfur and mercury within the zone of water-

table fluctuations in organic soils.

52. Sebestyen, S. D. *et al.* Long-Term Monitoring Sites and Trends at the Marcell Experimental Forest. in *Peatland Biogeochemistry and Watershed Hydrology at the Marcell Experimental Forest* 15–71 (2011).

53. Hanson, P. J. *et al.* Attaining whole-ecosystem warming using air and deep-soil heating methods with an elevated CO2 atmosphere. *Biogeosciences* **14,** 861–883 (2017).

54. Oak Ridge National Laboratory. SPRUCE Spruce and Peatland Responses Under Changing Environments. Available at: https://mnspruce.ornl.gov/.

55. US-EPA. Method 1631: Mercury in water by oxidation, purge and trap, and cold vapor atomic fluorescence spectrometry. *EPA 821-R-96-012. US EPA, Off. Water, Washington, DC* 1–46 (2002).

56. U.S. Environmental Protection Agency. Method 1630, Methyl Mercury in Water by Distillation, Aqueous Ethylation, Purge and Trap, and Cold-Vapor Atomic Fluorescence Spectrometry; EPA-821-R-01-020; Office of Water and Office of Science and Technology: Washington, D.C. (2001).

57. Zeng, T., Arnold, W. A. & Toner, B. M. Microscale characterization of sulfur speciation in lake sediments. *Environ. Sci. Technol.* **47,** 1287–1296 (2013).

58. Cron, B. *Personal Communication*.

59. Marcus, M. A., Westphal, A. J. & Fakra, S. C. Classification of Fe-bearing species from K-edge XANES data using two-parameter correlation plots. *J. Synchrotron Radiat.* **15,** 463–468 (2008).

60. Nicholas, S. L. *et al.* Solid-phase arsenic speciation in aquifer sediments: A micro-X-ray absorption spectroscopy approach for quantifying trace-level speciation. *Geochim. Cosmochim. Acta* **211,** 228–255 (2017).

61. Jones, E., Oliphant, E. & Peterson, P. SciPy: Open Source Scientific Tools for Python. (2001). Available at: http://www.scipy.org/.

62. Oliphant, T. E. Python for scientific computing. *J. Comput. Sci. Eng.* **9,** 10–20 (2007).

63. R Core Team. R: A language and environment for statistical computing. (2017).

64. Wickham, H. ggplot2: Elegant Graphics for Data Analysis. (2009).

65. Ihaka, R., Murrell, P., Hornik, K., Fisher, J. C. & Zeileis, A. colorspace: Color Space Manipulation. (2016).

66. Wickham, H. scales: Scale Functions for Visualization. (2017).

67. Wickham, H. tidyverse: Easily Install and Load the 'Tidyverse'. (2017).

68. Schloerke, B. *et al.* GGally: Extension to 'ggplot2'. (2017).

69. Wilke, C. O. cowplot: Streamlined Plot Theme and Plot Annotations for 'ggplot2'. (2017).

70. Auguie, B. gridExtra: Miscellaneous Functions for 'Grid' Graphics. (2017).

71. Kassambara, A. ggpubr: 'ggplot2' Based Publication Ready Plots. (2017).

72. Wickham, H. & Chang, W. devtools: Tools to Make Developing R Packages Easier. (2017).

73. Tang, Y., Horikoshi, M. & Li, W. ggfortify: Unified Interface to Visualize Statistical Result of Popular R Packages. *R J.* 478–489 (2016).

74. Horikoshi, M. & Tang, Y. ggfortify: Data Visualization Tools for Statistical Analysis Results. (2016).

75. Hope, R. M. Rmisc: Ryan Miscellaneous. (2013).

76. Archontoulis, S. V & Miguez, F. E. Supplemental Material for Nonlinear Regression in Agricultural Research List of Figures. *Agron. J.* **107,** 1–13 (2013).

77. Archontoulis, S. V. & Miguez, F. E. Nonlinear regression models and applications in agricultural research. *Agron. J.* **107,** 786–798 (2015).

78. Swain, E. B., Engstrom, D. R., Brigham, M. E., Henning, T. A. & Brezonik, P. L.

Increasing Rates of Atmospheric Mercury Deposition in Midcontinental North America Published by : American Association for the Advancement of Science Stable URL : http://www.jstor.org/stable/2877670. **257,** 784–787 (2010).

79. Engstrom, D. R. & Swain, E. B. Recent declines in atmospheric mercury deposition in the upper Midwest. *Environ. Sci. Technol.* **31,** 960–967 (1997).

80. van Groenigen, K. J., Qi, X., Osenberg, C. W., Luo, Y. & Hungate, B. A. Faster Decomposition Under Increased Atmospheric CO2 Limits Soil Carbon Storage. *Science (80-. ).* **344,** 508–509 (2014).

81. Grigal, D. F. Mercury sequestration in forests and peatlands: a review. *J. Environ. Qual.* **32,** 393–405 (2003).

82. Sebestyen, S. D. *Personal Communication*.

83. Pheiffer-Madsen, P. Peat bog records of atmospheric mercury deposition. *Nature* **293,** 127–130 (1981).

84. Baumgardner, R. E., Lavery, T. F., Rogers, C. M. & Isil, S. S. Estimates of the atmospheric deposition of sulfur and nitrogen species: Clean Air Status and Trends Network, 1990-2000. *Environ. Sci. Technol.* **36,** 2614–2629 (2002).

85. Haynes, K. M. *et al.* Gaseous mercury fluxes in peatlands and the potential influence of climate change. *Atmos. Environ.* **154,** 247–259 (2017).

86. Vile, M. A., Bridgham, S. D., Wieder, R. K. & Novák, M. Atmospheric sulfur deposition alters pathways of gaseous carbon production in peatlands. *Global Biogeochem. Cycles* **17,** n/a-n/a (2003).

87. Liu, G., Peng, Z., Yang, P. & Wang, G. Sulfur in coal and its environmental impact from Yanzhou mining district, China. *Chinese J. Geochemistry* **20,** 273–281 (2001).

# APPENDIX

**Figure 32** Multiple Linear Regression for Total Mercury (THg) in 2016

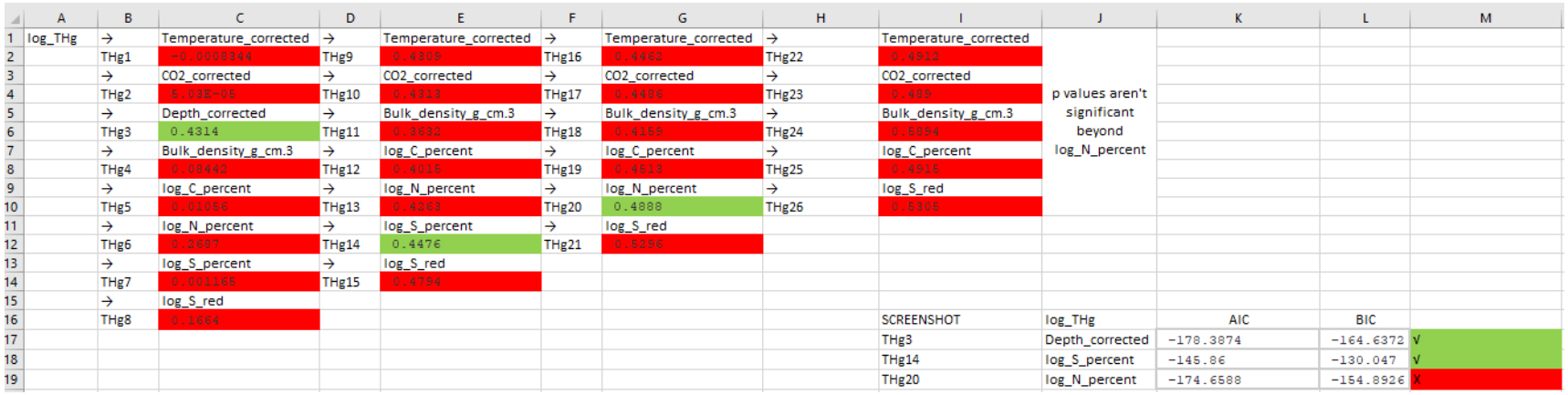

| | A | B | C | D | E | F | G | H | I | J | K | L | M |
|---|---|---|---|---|---|---|---|---|---|---|---|---|---|
| 1 | log_THg | → | Temperature_corrected | → | Temperature_corrected | → | Temperature_corrected | → | Temperature_corrected | | | | |
| 2 | | THg1 | -0.0008344 | THg9 | 0.4309 | THg16 | 0.4462 | THg22 | 0.4912 | | | | |
| 3 | | → | CO2_corrected | → | CO2_corrected | → | CO2_corrected | → | CO2_corrected | | | | |
| 4 | | THg2 | 5.03E-05 | THg10 | 0.4313 | THg17 | 0.4486 | THg23 | 0.495 | p values aren't | | | |
| 5 | | → | Depth_corrected | → | Bulk_density_g_cm.3 | → | Bulk_density_g_cm.3 | → | Bulk_density_g_cm.3 | significant | | | |
| 6 | | THg3 | 0.4314 | THg11 | 0.3632 | THg18 | 0.4155 | THg24 | 0.5894 | beyond | | | |
| 7 | | → | Bulk_density_g_cm.3 | → | log_C_percent | → | log_C_percent | → | log_C_percent | log_N_percent | | | |
| 8 | | THg4 | 0.08442 | THg12 | 0.4015 | THg19 | 0.4613 | THg25 | 0.4915 | | | | |
| 9 | | → | log_C_percent | → | log_N_percent | → | log_N_percent | → | log_S_red | | | | |
| 10 | | THg5 | 0.01056 | THg13 | 0.4263 | THg20 | 0.4888 | THg26 | 0.5305 | | | | |
| 11 | | → | log_N_percent | → | log_S_percent | → | log_S_red | | | | | | |
| 12 | | THg6 | 0.2687 | THg14 | 0.4476 | THg21 | 0.5296 | | | | | | |
| 13 | | → | log_S_percent | → | log_S_red | | | | | | | | |
| 14 | | THg7 | 0.001165 | THg15 | 0.4794 | | | | | | | | |
| 15 | | → | log_S_red | | | | | | | | | | |
| 16 | | THg8 | 0.1664 | | | | | | SCREENSHOT | log_THg | AIC | BIC | |
| 17 | | | | | | | | | THg3 | Depth_corrected | -178.3874 | -164.6372 | √ |
| 18 | | | | | | | | | THg14 | log_S_percent | -145.86 | -130.047 | √ |
| 19 | | | | | | | | | THg20 | log_N_percent | -174.6588 | -154.8926 | X |

**Figure 33** Multiple Linear Regression for Methylmercury (MeHg) in 2016

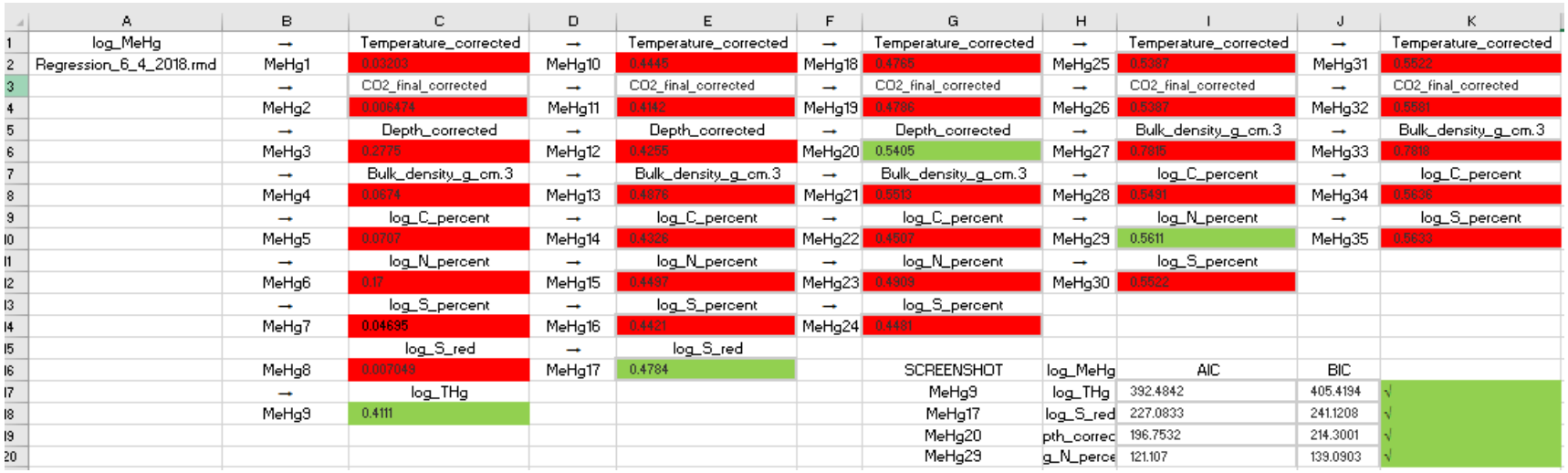

| | A | B | C | D | E | F | G | H | I | J | K |
|---|---|---|---|---|---|---|---|---|---|---|---|
| 1 | log_MeHg | → | Temperature_corrected | → | Temperature_corrected | → | Temperature_corrected | → | Temperature_corrected | → | Temperature_corrected |
| 2 | Regression_6_4_2018.rmd | MeHg1 | 0.03203 | MeHg10 | 0.4445 | MeHg18 | 0.4765 | MeHg25 | 0.5387 | MeHg31 | 0.5522 |
| 3 | | → | CO2_final_corrected | → | CO2_final_corrected | → | CO2_final_corrected | → | CO2_final_corrected | → | CO2_final_corrected |
| 4 | | MeHg2 | 0.006474 | MeHg11 | 0.4142 | MeHg19 | 0.4786 | MeHg26 | 0.5387 | MeHg32 | 0.5591 |
| 5 | | → | Depth_corrected | → | Depth_corrected | → | Depth_corrected | → | Bulk_density_g_cm.3 | → | Bulk_density_g_cm.3 |
| 6 | | MeHg3 | 0.2775 | MeHg12 | 0.4255 | MeHg20 | 0.5405 | MeHg27 | 0.7815 | MeHg33 | 0.7818 |
| 7 | | → | Bulk_density_g_cm.3 | → | Bulk_density_g_cm.3 | → | Bulk_density_g_cm.3 | → | log_C_percent | → | log_C_percent |
| 8 | | MeHg4 | 0.0674 | MeHg13 | 0.4876 | MeHg21 | 0.5513 | MeHg28 | 0.5491 | MeHg34 | 0.5636 |
| 9 | | → | log_C_percent | → | log_C_percent | → | log_C_percent | → | log_N_percent | → | log_S_percent |
| 10 | | MeHg5 | 0.0707 | MeHg14 | 0.4326 | MeHg22 | 0.4507 | MeHg29 | 0.5611 | MeHg35 | 0.5633 |
| 11 | | → | log_N_percent | → | log_N_percent | → | log_N_percent | → | log_S_percent | | |
| 12 | | MeHg6 | 0.17 | MeHg15 | 0.4487 | MeHg23 | 0.4909 | MeHg30 | 0.5522 | | |
| 13 | | → | log_S_percent | → | log_S_percent | → | log_S_percent | | | | |
| 14 | | MeHg7 | 0.04695 | MeHg16 | 0.4421 | MeHg24 | 0.4481 | | | | |
| 15 | | | log_S_red | → | log_S_red | | | | | | |
| 16 | | MeHg8 | 0.007049 | MeHg17 | 0.4784 | | SCREENSHOT | log_MeHg | AIC | BIC | |
| 17 | | → | log_THg | | | | MeHg9 | log_THg | 392.4842 | 405.4194 | √ |
| 18 | | MeHg9 | 0.4111 | | | | MeHg17 | log_S_red | 227.0833 | 241.1208 | √ |
| 19 | | | | | | | MeHg20 | pth_correc | 196.7532 | 214.3001 | √ |
| 20 | | | | | | | MeHg29 | g_N_perce | 121.107 | 139.0903 | √ |

**Figure 34** $Log_{10}$ Transformed Total Mercury (THg) Residuals vs. Leverage Plot